The Dissertation Committee for Benjamin James Spivey
certifies that this is the approved version of the following dissertation:

Dynamic Modeling, Model-Based Control, and Optimization of Solid Oxide Fuel Cells

Committee:

Thomas F. Edgar, Supervisor

Roger Bonnecaze

Dongmei Chen

Jeremy Meyers

Gary Rochelle

Dynamic Modeling, Model-Based Control, and Optimization of Solid Oxide Fuel Cells

by

Benjamin James Spivey, B.S.M.E., M.S.E.

DISSERTATION

Presented to the Faculty of the Graduate School of
The University of Texas at Austin
in Partial Fulfillment
of the Requirements
for the Degree of

DOCTOR OF PHILOSOPHY

THE UNIVERSITY OF TEXAS AT AUSTIN
August 2011

Dedicated to my parents.

Acknowledgments

I would like to thank my advisor, Professor Thomas Edgar, for his accessibility, responsiveness, and direction throughout the doctoral process. His trust and support enabled me to pursue my research ideas, and I am grateful for the opportunities he has provided to advance my engineering experience. I have enjoyed working with him the past several years. I also thank my dissertation committee members: Prof. Meyers; Prof. Chen; Prof. Rochelle; and Prof. Bonnecaze. I appreciate their availability and feedback on my research.

I would like to recognize the contributions made by several alumni of Dr. Edgar's group. Dr. John Hedengren has provided generous advice and continuous support with modeling software and optimization methods. Dr. Ricardo Dunia has been a valuable resource both as a professor and colleague in process controls. Dr. Tyler Soderstrom has provided guidance during the doctoral process. I would like to thank John Hedengren, Gib Siard, and Steve Toney who served as mentors during my internships with ExxonMobil along with the many additional engineers at ExxonMobil who contributed to my understanding of current issues in process control.

I am grateful for the support provided by the National Science Foundation as part of the IGERT program and The University of Texas at Austin for the Engineering Doctoral Fellowship. I would like to acknowledge my fellow students in the Edgar lab for their valued encouragement and engaging discussions: Ivan Castillo, Bhalinder Singh Gill, Doug French, Blake Parkinson,

Kody Ford, Anh Nguyen, Ramiro Palma, Jong Kim, Ninad Patwardhan, Ela Joag, Xiaojing Jiang, Kriti Kapoor, Vinay Bhardwaj, Wesley Cole, Akshay Sripasad, Yang Zhang, Amogh Prabhu, Dan Weber, Hyung Lee, and Sidharth Abrol. I appreciate the work Zack Doran performed as an undgraduate research assistant in modeling the indirect internal reformer. I would like to credit Sarah De Berry-Caperton and Chris Bailor for their reliable support to our lab.

Finally, I thank mostly my parents for their positive words and readiness to listen throughout this work. Their consistent dedication has enabled me to pursue my educational dreams and achieve the completion of my doctoral degree. I credit them for encouraging me to have a passion for education and lifelong learning.

Dynamic Modeling, Model-Based Control, and Optimization of Solid Oxide Fuel Cells

Publication No. __________________

Benjamin James Spivey, Ph.D.
The University of Texas at Austin, 2011

Supervisor: Thomas F. Edgar

Solid oxide fuel cells are a promising option for distributed stationary power generation that offers efficiencies ranging from 50% in stand-alone applications to greater than 80% in cogeneration. To advance SOFC technology for widespread market penetration, the SOFC should demonstrate improved cell lifetime and load-following capability. This work seeks to improve lifetime through dynamic analysis of critical lifetime variables and advanced control algorithms that permit load-following while remaining in a safe operating zone based on stress analysis. Control algorithms typically have addressed SOFC lifetime operability objectives using unconstrained, single-input-single-output control algorithms that minimize thermal transients. Existing SOFC controls research has not considered maximum radial thermal gradients or limits on absolute temperatures in the SOFC. In particular, as stress analysis demonstrates, the minimum cell temperature is the primary thermal stress driver in tubular SOFCs.

This dissertation presents a dynamic, quasi-two-dimensional model for a high-temperature tubular SOFC combined with ejector and prereformer models. The model captures dynamics of critical thermal stress drivers and is used as the physical plant for closed-loop control simulations. A constrained, MIMO model predictive control algorithm is developed and applied to control the SOFC. Closed-loop control simulation results demonstrate effective load-following, constraint satisfaction for critical lifetime variables, and disturbance rejection. Nonlinear programming is applied to find the optimal SOFC size and steady-state operating conditions to minimize total system costs.

Table of Contents

List of Tables

List of Figures

Nomenclature

ARX	autoregressive with exogeneous input
CFD	computational fluid dynamics
CHP	combined heat and power
CTQ	critical to quality variable (with reference to Six Sigma)
CV	controlled variable
DER	distributed energy resource
DIR	direct-internal-reforming
EEA	electrode electrolyte assembly
GT	gas turbine
IAE	integrated absolute error
IEA	International Energy Agency
IIR	indirect-internal-reforming
$ITAE$	integrated time-weighted absolute error
kWe	kilowatt electricity
LHV	lower heating value
LQR	linear quadratic regulator
LTI	linear time invariant
$MIMO$	multi-input multi-output

$MISO$	multi-input single-output
MPC	model predictive control
MV	manipulated variable
$NARMAX$	nonlinear autoregressive moving average with exogeneous input
NLP	nonlinear programming
PDF	probability density function
PID	proportional-integral-derivative
QP	quadratic programming
QSS	quasi-steady-state
$RBFNN$	radial basis function neural network
RGA	relative gain array
RMS	root mean square
SCR	steam-to-carbon ratio
$SISO$	single-input single-output
$SOFC$	solid oxide fuel cell
UA	air utilization
UF	fuel utilization

Chapter 1

Introduction

1.1 Motivation for Distributed Energy

Combined heat and power (CHP) systems have been identified by the Department of Energy as an ideal integrated distributed energy resource (DER) for high efficiency energy generation for residential, commercial, and industrial building complexes. Fuel-based sources commonly used for CHP will complement expanding implementation of intermittent renewable energy sources to improve DER micro-grid robustness.

Increasing CHP production has been an ongoing trend with current production increasing from 46 to 85 GW since the DOE CHP Roadmap was created in 1998. The DOE is accelerating the CHP Program to target CHP power production reaching 20% of U.S. electricity capacity by 2030 which will provide fuel savings estimated at 5.3 quadrillion BTUs, approximately half of current U.S. household consumption, and emissions reductions equivalent to 154 million cars, half of all current passenger vehicles, removed off the road [27]. Electrical power and heat are utilized in cogeneration systems to meet electrical, thermal, and cooling loads on the customer's micro-grid while excess power potentially may be sold to the utility grid. In addition, renewable technologies, such as photovoltaic cells or waste heat recovery engines, may also be integrated into a CHP energy system to minimize grid power usage.

By its nature cogeneration is often applied as a distributed energy resource in which the power source is located in proximity to the customer. A DOE study demonstrated that CHP systems increased energy savings by 10% over stand-alone distributed power generation for a representative New York large office building [26]. The study results were consistent for both advanced engine and microturbine generation with a maximum efficiency of less than 45% for the advanced engine; however, with less efficient generation, a greater percentage of waste heat should be used to boost prime mover recuperation than downstream waste recovery. The primary conclusion of the aforementioned study is that high efficiency power generation is critical for viable CHP implementation.

1.2 Role of Fuel Cells in Stationary Power Generation

Solid oxide fuel cell (SOFC) systems are ideal candidates for the prime mover of DER and CHP systems due to demonstrated high efficiencies, low environmental and noise emissions, fuel flexibility, and potential for various balance of plant (BOP) configurations. Stand-alone SOFC systems have demonstrated efficiencies ranging from 40-50%, and efficiencies from 60-70% have been reported for pressurized hybrid gas turbine-solid oxide fuel cell (GT-SOFC) systems. SOFC systems release a high temperature effluent gas ranging from 600-1000°C thereby permitting internal reformation of fuels such as natural gas and syngas. The high operating temperatures also open the potential for a variety of CHP applications and bottoming combined-cycles. Combining the SOFC-based prime mover with downstream users of thermal energy, including steam, hot water, air conditioning, into a CHP system increases overall efficiency to approximately 80% [34]. SOFC are particularly ideal for application in the immediate future since the existing natural gas infrastructure can be utilized.

Siemens Power Generation, Inc., developed a cathode-supported tubular SOFC for a field unit demonstration program including a 100-kWe combined heat and power system and a 220-kWe pressurized GT-SOFC power system [31]. The former demonstration was the world's largest operating SOFC system through August 1999 as it produced 105-110 kWe net AC and 65 kWt to the hot water district heating system; the electrical efficiency was demonstrated to be 46% net AC LHV. The 220 kWe system was the first demonstration of a pressurized GT-SOFC system with startup in Fall 1999. The 100 kWe SOFC has accumulated over 38,000 hours of operation at multiple sites [38].

Siemens remains an active participant in the Solid State Energy Conversion Alliance (SECA). Recent reports from Siemens demonstrate a continued effort to optimize cell geometry using various tubular structures, circular, triangular (Delta), and flattened tubular (high-power density, HPD) as shown in Figure 1.1. The circular tubular geometry has been placed in active duty in the field unit demonstrations previously described. The HPD series has been developed to reduce cathode ohmic resistance by introducing multiple parallel current paths; the HPD has an active area similar to the tubular geometry. The HPD10 was the optimal configuration in this geometry. The Delta series was later developed to increase the active area and thereby power of each cell. The Delta 8 is the current preferred geometry for manufacturing and mod-

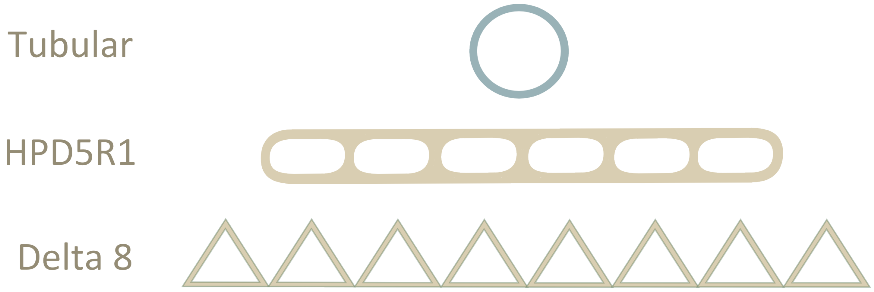

Figure 1.1: Cross-sections of several Siemens Power Generation, Inc. SOFC designs (not to scale)

ularity considerations. In a numerical comparison of Delta 8 and HPD5R1 geometries for 100 kWe AC systems, the Delta 8 produced a net electrical efficiency of 48.6% versus 46.8% for the HPD5R1; note that these figures do not reflect efficiency increases from CHP or combined-cycle applications. The total number of cells required for the Delta 8 is less than half at 254 versus 578. The exhaust temperatures indicate potential for downstream heat recuperation at 867 and 901°C for the Delta 8 and HPD5R1, respectively.

Additional industrial partners affiliated with SECA are Acumentrics Corporation, Cummins Power Generation, Delphi Automotive Systems LLC, Fuel Cell Energy, and GE Global Research. A 5 kWe/3 kWt SOFC system installed by Acumentrics, CP-SOFC-5000 Fuel Cell Generator, at Edison R&D Centre in Italy in 2007 has reported 1500 h operation time over four startup cycles; they report a degradation of less than 5% over the first 1000 h [19]. Long lifetimes, load-following, cost reduction, and high efficiency are primary goals of SECA efforts.

In addition, the NEDO consortium in Japan has led a continued effort in the past decade for developing SOFCs since 2004 while Europe has produced several SOFC collaborations among industry and academia. In October 2010, a presentation by NGK Spark Plug in collaboration with TOHO Gas Co., Ltd. reported field demonstration of a micro CHP SOFC producing electrical power between 200-1300 W and 75°C hot water at electrical efficiency of 50% and total efficiency of about 83% [56]. TOHO also reports a 3 kW planar SOFC system that produced a record high 59% efficiency DC LHV with a total operating time of 750 h [44]. Collaboration between Danish firm Topsoe Fuel Cell A/S and Riso University has reported satisfaction of SECA Phase 1 minimum requirements with 5 kWe SOFC installed in Epsoo, Finland, that produced 4 kWe over 3,000 h since Q1 2007, an availability over 80% and a degradation of 1%/1000 h which is less than the SECA target of 2%/500 h [48, 49]. Maximum efficiency was 57% with total load cycle efficiency of 37% due to part load operation. The Danish alliance has produced 1,100 solid oxide fuel cells by 2009. A Swiss company, Hexis, Ltd., reported cost-competitive manufacturing of 1 kWe planar SOFC via a screen printing technique since 2001 [74].

Comparison of SOFC efficiencies to fuel-based alternatives illustrates the advantage offered by SOFC power generation. Average power plant efficiency in the U.S. is 33.2% with coal power plants operating at 20-38% and combined cycle natural gas plants operating at 30-50% efficiency, as summarized by Colson and Nehrir [19]. Trends of fossil power generation in the European Union reported that average efficiencies of natural gas-powered generation has increased from 34% to 50% from 1990 to 2005 with a predicted increase to 54% in 2015; note that the efficiency of gas turbines increases with capacity with the highest efficiencies being over one-hundred MW affecting this average [32]. Average efficiencies of coal-powered generation have increased from 34 to 38% with a predicted increase to 40% by 2015. These efficiency calculations incorporate LHV energy efficiency improvements through CHP and combined-cycle by summing power production with heat production multiplied by a correction factor and dividing the total by total fuel input.

In particular, several studies have compared the SOFC versus other power plants for combined heat and power systems. In 2008 Karellas, et. al., investigated a CHP system using either a microturbine or SOFC coupled with the Biomass Heatpipe Reformer, which produces a hydrogen-rich effluent fuel [41]. Heat from the prime mover is consumed by the reformer. The microturbine is a Capstone C30 with an electrical efficiency of 26% and power output of 30 kW; the total system efficiency and electrical efficiency reach a peak near 70% and 19% respectively. The SOFC CHP system offers peak total and electrical efficiency over 80% and 40% respectively. In 2010 Shaneb, et. al., discussed the application of internal combustion engines, stirling engines, and fuel cells for single dwelling μCHP [67]. Their review concluded that fuel cells offer the lowest noise and pollution emissions, lowest maintenance requirements, and highest electrical efficiencies at partial load. The primary challenges with using fuel cell in this application are limited market availability, short lifetimes, and relatively high costs.

1.3 Research Motivation

Solid oxide fuel cells are a promising emerging energy technology that offers many advantages over power generation alternatives. However, SOFC have not become a mainstream power generation technology due primarily to challenges of manufacturing cost, cell reliability, and operational flexibility. The motivation of this research is to address reliability and operational flexibility challenges by characterizing the dynamic behavior of SOFC critical-to-quality (CTQ) variables and by investigating and providing an advanced control solution to improve SOFC lifetime and operational flexibility with respect to fuel quality variation. In addition, as the U.S. electrical grid is enhanced to proposed smart grid capabilities, a real need exists to provide advanced control and optimization that is real-time, predictive, capable of autonomous action, and able to diagnose faults and provide solutions [25].

The SOFC offers higher efficiency, lower emissions, and lower noise than turbomachinery at power generation capacities appropriate for distributed energy generation at power capacities from 1 kW to 100 MW. The SOFC may operate on a variety of fuels and provide high temperature waste heat with operating temperatures between 600-1000°C as shown in Figure 1.2. While the SOFC electrode-electrolyte assembly (EEA) is composed of ceramic layers, other fuel cell technologies such as direct methanol fuel cells (DMFC), proton exchange membranes (PEM), phosphoric acid fuel cells (PAFC), and molten carbonate fuel cells (MCFC) require expensive metals, corrosive acids, or molten material to participate in redox reactions. Companies report manufacturing SOFCs at a competitive cost for distributed energy applications;

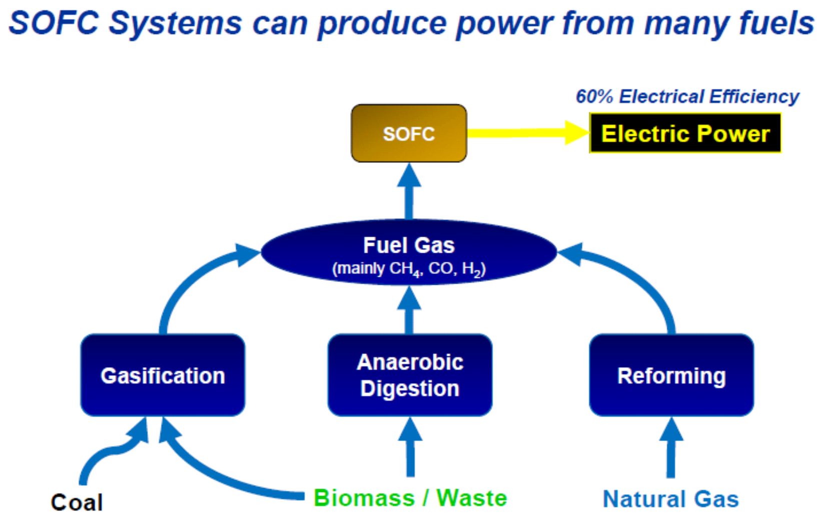

Figure 1.2: SOFC systems may operate directly on methane via internal reformation [75]

these SOFC operate on pipeline-delivered natural gas at businesses and homes. The American company Bloom Energy provides SOFC-powered electricity service via Bloom Electrons to customers in CA at rate 5 to 20% below the grid rate while reducing CO_2 emissions and nearly eliminating NO_x and SO_x emissions. As of January 2011, state incentives and long-term natural gas contracts are necessary to achieve this competitive rate.

Despite the benefits of SOFCs and decades of university and industry research, solid oxide fuel cells have yet to become a mainstream power generation platform for several reasons. Manufacturing cost of the SOFC has been one limiting factor. SOFC stack manufacturing cost is reported by the Solid-state Energy Conversion Alliance (SECA) as greater than \$1500/kW at the outset of the SECA collaboration in 2000 with the goal of reducing stack cost to \$175/kW to provide an overall power generation cost of \$700/kW by 2012

(2007 dollar basis) [75]. Reported SOFC lifetimes have not yet reached SECA design life goals of greater than 40,000 h. As of Q1 2009 Siemens reported a successful completion of a 5,000 h stack test on the Delta8 R0 SOFC and plans to complete a 25,000 h stack test on a Delta 8 MWe-class module by Q3 2015 [60]. SOFCs are susceptible to many modes of failure and degradation ranging from microcracking, delamination, corrosion, redox material degradation, and catalyst poisoning; thermomechanical stress is primary driver of SOFC failure and degradation. In order to meet the SECA requirements, the fuel cell community recognizes the importance of a fundamental understanding of fuel cell dynamics and controlling the reliability CTQ variables - steam-carbon ratio, thermal gradients, local temperatures, and fuel/air utilizations [13].

Some reports have predicted a market for advanced control and networking for DERs reaching between \$3.75 to \$7.5 billion within the U.S. and \$15 to \$30 billion globally with the assumption that these controls can provide 5-10% energy savings, not considering renewable energy savings [50]. State of the art controls research on SOFC systems commonly seeks to address reliability issues indirectly via minimizing variation of either a constant lumped stack temperature, the outlet gas temperature, or voltage using a regulatory controller; these approaches are discussed in more detail in Chapter 2. However, it remains to be demonstrated whether controlling the lumped or outlet temperatures or voltage is a satisfactory approach for controlling the fundamental reliability CTQ variables, minimum cell temperature and maximum radial thermal gradient for the tubular SOFC. Reported SOFC controls solutions are commonly single input-single output (SISO) or multiple input-single output (MISO) and therefore do not incorporate multivariable interactions throughout the SOFC into a centralized control scheme. Finally, the real control objective for most controlled variables is to prevent exceeding limits, such as maximum utilization limits, yet regulatory controllers are typically used to control these CVs, thereby tying up valuable manipulated variables. Justification for use of model predictive control (MPC) for nonlinear systems is readily seen as even the first generation of MPC had an enormous impact to improve process control within the chemical industry over the past few decades [62].

Advanced dynamics and controls research opportunities for solid oxide fuel cell applications include the following components: (1) investigating dynamics of SOFC reliability CTQ variables; (2) identifying appropriate multivariable SOFC control structures; (3) determining benefits of constrained multivariable MPC with regards to load-following, disturbance rejection, and reliability constraint satisfaction; and (4) developing an economically optimal system. Advanced control holds much promise to expand the range of operability, lifetime, and efficiency of future SOFC builds.

1.4 Project Description

The proposed SOFC control research seeks to answer open questions regarding the extent to which MPC may improve SOFC operating constraint satisfaction, load-following capability, robustness to unmeasured disturbances, and economically optimal operation. Answering these questions is expected to alter the paradigm for SOFC systems by improving the predicted efficiency and expanding the operating range with regards to fuel flexibility and electrical and thermal load following. These objectives may be simultaneously achieved by consistently maintaining tight constraint satisfaction while expanding the operating envelope for load-following and fuel flexibility.

The specific SOFC system chosen for this research initiative is a cathode-supported tubular SOFC modeled after the tubular Siemens-Westinghouse design. The cathode-supported tubular design has a large amount of publicly available steady-state operating and modeling results in comparison to other SOFC designs. The availability of these results is necessary for model validation in absence of an experimental fuel cell apparatus.

This dissertation addresses the aforementioned SOFC research goals through three primary steps:

- Dynamic modeling: The SOFC is modeled dynamically via a set of nonlinear, highly-coupled differential and algebraic equations (DAE). The distributed parameter model improves model accuracy over lumped models and provides local states that may be used to calculate worst-case temperatures and gradients for reliability assurance. The dynamic SOFC system is modeled as a DAE within APMonitor, and all thermo-electrochemical equations are solved simultaneously in open-loop with APMonitor/APOPT as a square nonlinear program.
- Model-Predictive Control: The MPC problem formulation used to control the SOFC incorporates a nonlinear objective function based on the predicted dynamic state response, hard constraints on manipulated variable (MV) upper and lower limits and changes in the MV (i.e., move suppression), and soft constraints on controlled variable (CV) limits using

slack variables. Multi-input single-output (MISO) transfer-function process models are converted directly to a linear-time-invariant multi-input multi-output (MIMO) state-space formulation for use as the controller model. The MPC is applied to track loads in the presence of fuel quality disturbances. CVs are chosen as the performance variable, power, and operability variables (i.e., fuel utilization, thermal gradient, etc.).

- Optimization: Determining the optimal number of cells and operational inputs to the system will provide the necessary information for sizing the SOFC system and balance of plant equipment. The economic-based objective function is composed of capital and operating costs, and the optimization problem is constrained by operational limits equivalent to those used in model-predictive control.

1.5 Dissertation Structure

In this introductory chapter, advanced dynamic modeling and control of a tubular solid oxide fuel cell system is proposed as an energy systems research area requiring further controls research to answer questions regarding performance and lifetime goals. Advanced control of the SOFC is discussed in the context of U.S. national priorities identified by smart grid programs within the National Energy Technology Laboratory. These programs specifically identify growing demand for both distributed energy resources and improved grid control and monitoring. The primary components of this research are identified as detailed dynamic modeling of an SOFC, advanced control system development, and economic optimization.

Chapter 2 provides a literature review of planar and tubular solid oxide fuel cell system modeling and controls research progress during the past two decades. The review provides justification for the modeling and controls approach chosen for this research as it highlights alternative modeling and controls approaches. Following a literature review introduction, this chapter is organized in three sections: plant modeling and simulations, SOFC control strategies, and reliability. The common controls objectives for all SOFC research is presented first; the controls review continues with a summary of classical control approaches, comprised of PI and PID controllers, and model-based control solutions, including H-infinity, optimal control, and predictive control. The reliability section provides justification for the operability controlled variables chosen in this research.

Chapter 3 provides a detailed overview of SOFC system modeling in this work, comprising the fuel cell, ejector, and prereformer sub-models integrated within MATLAB/Simulink. The time-discrete dynamic fuel cell DAE model is modeled within APMonitor and solved with the APOPT nonlinear programming (NLP) solver. System modeling decisions are discussed regarding thermodynamic assumptions, electrochemical and thermal modeling, chemical species, transport delays, and spatial and temporal discretization.

Chapter 4 presents a summary of open-loop steady-state and dynamic simulation results. Steady-state validation is performed using publicly available plant data as common in validation of tubular SOFC models and by comparing temperature and concentration profiles to distributed parameter model results by Campanari [17]. Steady-state analysis is further used to investigate multivariable interactions, radial versus axial temperature gradients, and the accuracy of a reduced-order distributed parameter model. The dynamic model is verified by comparing the settling time to other works, examining the effects of time discretization and transport delays, and the dynamic MV-CV interactions. Results from the dynamic staircase test provide insight for designing the control structure. The open-loop dynamic response to disturbances demonstrates the need for closed-loop control.

Chapter 5 presents the closed-loop dynamic results using model predictive multi-input multi-output (MIMO) control. A description of the control structure is provided first followed by the closed-loop results. Results from controller tuning for the controller time-step and prediction horizon justify control tuning parameters. Load-following results demonstrate the tradeoffs between tracking objectives and constraints. A reliability control study justifies the need for controlling the true reliability CVs, the minimum cell temperature and maximum radial thermal gradient for the tubular SOFC by Siemens Power Generation, Inc., rather than measurements that indirectly represent reliability concerns such as a lumped cell temperature or outlet gas temperature. Finally, the controller is shown to maintain the load within 3% of nominal when subjected to fuel quality disturbances of ± 10%.

Chapter 6 discusses steady-state optimization of the SOFC with regards to sizing and operational setpoints. The detailed model used to represent the physical plant in dynamic simulations is used by the optimization routine as a set of nonlinear algebraic constraints. The use of such a detailed model permits inclusion of MV and CV operability constraints thereby ensuring that the optimal solution is feasible and does not induce excessive thermal stresses. The optimization is successful in finding optimal SOFC sizing and operational setpoints that reduce operational costs by 5% and satisfy all operational constraints.

Chapter 7 summarizes the contributions within this work and presents recommendations for future work.

Chapter 2

Background

2.1 Introduction

During the past decade, researchers have been successful in advancing the state of the art in solid oxide fuel cell (SOFC) modeling and controls. Fuel cell dynamic simulation models have advanced to include balance of plant equipment with reformers, ejectors, heat exchangers, various piping and valves, pumps and blowers, and electrical management systems. Various configurations of hybrid gas turbine-solid oxide fuel cell systems have been investigated. Spatially distributed models have recently been applied to control applications.

This literature review seeks to provide a sufficient background in recent solid oxide fuel cell modeling and control research in order to achieve several goals: (1) demonstrate why the SOFC is modeled with the specific assumptions and structure used in this dissertation, and (2) illustrate how the research in this dissertation expands the field of SOFC control and operation. To these ends this chapter begins with a review of plant modeling research relevant to the present model; the model section comprises steady-state planar, steady-state tubular, dynamic planar, and dynamic tubular SOFC models as well as prereformer and ejector models. Schematics of the tubular and planar geometries are shown in Figure 2.1. A review of SOFC control literature follows the plant modeling discussion and provides an overview of classical

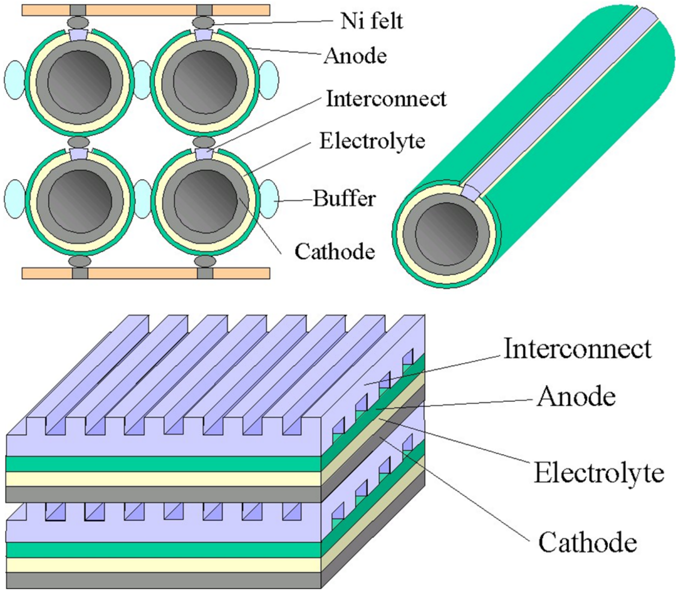

Figure 2.1: Renderings of the tubular (above) and planar (below) geometries [43]

and model-based control for planar and tubular SOFC systems. The controls section concludes by discussing motivation for further SOFC controls research. Finally, mechanical reliability research discusses justification for choosing the operability controlled variables to extend fuel cell lifetime.

2.2 Plant Modeling and Simulation

2.2.1 Solid Oxide Fuel Cell

Solid oxide fuel cell models have been created for many purposes; material design and selection, feature design, system design, operational strategies, and component selection are the primary applications. Models considered in this literature review are intended to provide insight into overall fuel cell system design and operational and control strategies along with insight into internal phenomena. The most common geometries, planar and tubular, are reviewed to give insight into modeling differences and provide a suitable background for the high-temperature, direct-internal-reforming (DIR) steady-state and dynamic tubular SOFC modeling approach used in this work. Cells considered herein may also vary in configurations such as medium or high temperature cells, anode-, electrolyte-, or cathode-supported and indirect- (IIR) or direct-internal reforming cells. The models are based upon first-principles characterization of fuel cell phenomena using energy, material, and momentum balances and thermodynamic and electrical expressions. This review is limited to models on a similar level of detail as the tubular model presented herein; models designed solely for detailed analysis of material properties or localized phenomena within the cell, as with material studies and atomic-scale modeling, are not included here. Models vary in many aspects for the intended use but most current models for system evaluation share the common features of modeling a single cell to represent stack behavior, lumped layer properties for 1D and 2D models or fully lumped models, and simplification of system-environment heat exchange at boundaries. Additional common assumptions are equipotential, ideal gas, H_2 as the sole redox fuel, and the water-gas shift reaction at equilibrium.

The models considered also range from lumped models to two-dimensional models and include both steady-state and dynamic models. Compared to the field of steady-state fuel cell models, the types of dynamic fuel cell models are much more limited in number; however, a thorough understanding of fuel cell dynamics is critical for designing systems and controllers to maximize cell lifetime [13]. Data available for validation of tubular models is particularly scarce.

This review of SOFC models categorizes the models as planar or tubular and steady-state or dynamic. Each model is analyzed for the transport balances considered, spatial discretization, electrochemical simplifications, chemical reaction models, thermal interactions and boundaries, and other key assumptions and simplifications. In addition, some authors' models provide good examples of key model design choices, such as iterative vs. simultaneous solution techniques, and these unique features are discussed. A summary of models reviewed in this chapter is shown in Table 2.1.

Table 2.1: Review of solid oxide fuel cell modeling literature

Design	Time	Discretization	Balance of Plant	Radiation	Reformation Reaction	Year published	Authors
Geometry independent	Steady-state	3D	n/a	Not considered	Lee [46]	1999	Ferguson, Fiard, Herbin [29]
Circular planar	Steady-state	2D	Afterburner, preheater	End effect	n/a	1998	Costamagna and Honneger [20]
Planar	Steady-state	3D CFD	n/a	Not considered	n/a	2003	Yuan, Rokni, Sunden [80]
Planar, Tubular	Steady-state	2D	hybrid GT-SOFC system	Planar - end effect, tubular - internal and end effect	Rechnenauer, Achenbach [63]	2005	Stiller, Bolland, et al. [71]
Planar	Steady-state and dynamic	1D	n/a	Internal	Achenbach, Riensche [2]	2004	[3, 4]
Planar	Dynamic	3D	Fuel processor	Within a global heat transfer coefficient	Not provided	2003	Petruzzi, Cocchi, and Fineschi [59]
Planar	Dynamic	2D	n/a	Not considered	Achenbach, Riensche [2]	2008	Xi, Sun [76]
Tubular	Steady-state	1D	Ejector, prereformer	Not considered	n/a	2001	Campanari, Iora [16]
Tubular	Steady-state	2D	n/a	Not considered	Ahmed, Foger [6]	2004	Campanari, Iora [17]
Tubular	Steady-state	2D	n/a	Internal	Only chemical equilibrium	2003	Li, Chyu [47]
Tubular	Steady-state	2D	n/a	Internal	Xu, Froment [77]	2010	Dokmaingam, Laosiripojana, et al. [24]
Tubular	Dynamic	2D	n/a	Internal	n/a	1999	Hall, Colclaser [33]
Tubular	Dynamic	2D	Afterburner, ejector, prereformer	End effects and internal	Achenbach, Riensche [2]	2004	Thorud, Stiller, et al. [73]
Tubular	Dynamic	2D	n/a	End effect	n/a	2005	Xue, Du, et al. [78]
Tubular	Dynamic	2D	n/a	Not considered	n/a	2009	Barzi, Hamedi, et al. [8]

[a] Uses a root mean square objective function

2.2.1.1 Steady-State Planar SOFC Models

In one of the earlier reports of SOFC modeling in 1996, Ferguson, Herbin, et al., [29] present a three-dimensional, steady-state model that is geometry independent although the majority of results apply to the planar cell. The model provides local temperature, voltage, and concentration potential using finite-volume discretization over a single-cell; their discretized model uses multiple nodes over three dimensions for each cell layer. The authors apply the model to optimize planar cell design parameters, rib width and anode thickness. As is common in many SOFC models, the electrochemical reactions occur at the electrode electrolyte assembly(EEA) layer interfaces on either side of the electrolyte and the shift and reformation reactions occur in the porous cathode and cathode gas channel. Molar flux within the porous electrodes is modeled by Fick's law; this is particularly important for planar cells due to the low aspect ratios. Two gas-phase reactions occur within the anode chamber as shown in Equation 2.1.

$$\begin{aligned} CH_4 + H_2O &\xleftrightarrow{r_{CH_4}} CO + 3\,H_2 \\ CO + H_2O &\xleftrightarrow{r_{shift}} CO_2 + H_2 \end{aligned} \tag{2.1}$$

The reformation reaction rate is based upon a model by Lee which has the rate as a function of methane and steam partial pressure [46]; the water-gas shift reaction is modeled at equilibrium, a common assumption. The electrochemical reaction occurring within the SOFC involves oxygen diffusing through the porous cathode, undergoing reduction at the cathode/electrolyte interface, oxygen anions traveling across the electrolyte towards the cathode, and hydrogen oxidation at the cathode/electrolyte interface as shown in Figure 2.2. Carbon monoxide can also undergo electrochemical oxidation at the cathode but is not considered in Ferguson's model or the present model in this dissertation. The redox reactions consist of two half-reactions, each one occurring at the anode and cathode respectively as shown in Equation 2.2.

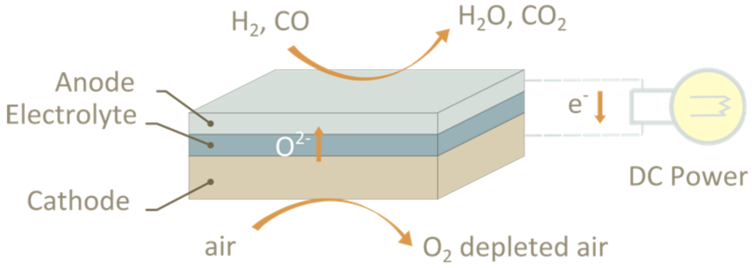

Figure 2.2: Redox reactions occurring within the solid oxide fuel cell

$$\begin{aligned} H_2 + O^{-2} &\xrightarrow{r_{anode}} H_2O + 2\,e^- \\ O_2 + 4e^- &\xrightarrow{r_{cathode}} 2\,O^{-2} \\ 2\,H_2 + O_2 &\xrightarrow{r_{redox}} 2\,H_2O \end{aligned} \tag{2.2}$$

Heat transfer within the channels involves convection in the flow direction and conduction to the solid parts through a thermal boundary layer; conductive heat transport within the solid layers is modeled with Fourier's law. Radiation is neglected in this work although they recognize a need to include radiation; the authors mention that the fourth-order nonlinearities will require a special numerical approach using their method. Faraday's law relates the mass flux to the current flow. Electrical potential is constant throughout their model except at the electrode-electrolyte interfaces where they provide a boundary condition based on Nernst's law. An advanced aspect of their model when published was the use of temperature-dependent electrical resistance. They consider six species, H_2, H_2O, CH_4, O_2, CO, and CO_2. Their model accepts use of pure hydrogen or methane as an inlet fuel, and results are presented for atmospheric conditions. Validation data, though currently limited for geometries other than planar, was much more limited in 1996, and the only validation is presented for the planar model based upon IEA Workshop, 1989, simulation data. The maximum efficiency reached during anode thickness and rib width parameter tests is 49.6%.

A circular, planar solid oxide fuel cell with integrated preheater model is presented by Costamagna, et.al., [20] for small to medium range power co-generation; the circular cell shape was novel when presented by Costamagna in 1998. Their stated modeling purpose is to plan a safe experimental operating strategy for a SOFC with preheater. The authors validate their data with two experimental SOFC stacks with radial flow and having five to six cells each. The model is two-dimensional in the radial and axial directions; angular state dependence is found to be negligible through the authors' experiments. Ohmic, activation, and concentration polarization are considered as overpotential losses to compute the realized voltage. Mass and energy balances are written in plug flow form. No internal reformation is mentioned in the model description although operating temperatures are sufficiently high to induce reformation. Key boundary assumptions are constant temperature and potential and feed gas concentration along the axial direction of the cell structure, adiabatic surfaces on the ends, convective and radiative heat transfer along the length to the shell, and afterburning of the reactants. Radiation is assumed to be negligible between adjacent rib surfaces based upon the more dominant effect of interconnect conduction for this cell structure. Costamagna reports a maximum power density of 1860 W/m^2 which results in 18.6 W for the experimental cell.

Yuan, et.al., developed a three-dimensional steady-state CFD model to analyze heat transfer and pressure drops within a medium-temperature (700-850°C) planar SOFC with thick porous anodes [80]. The authors note that concentration polarization is a critical overpotential loss due to the anode thickness. This model is used to assess the effects of cell design parameters, geometry, material permeation, and entrance pressure gradient, on the transfer phenomena. Since the source fuel is hydrogen, internal reformation is not considered in the material or energy balances. Radiation is also not considered although it is noted that it may be a factor, especially along the anode reaction surfaces. Both of these two factors, radiation and reformation, are more prominent as the cell operating temperature increases.

Stiller, Bolland, et.al., presented a detailed description of their steady-state two-dimensional SOFC model and results for both planar and tubular geometries fueled by methane [70]. The authors implement their model within a hybrid GT-SOFC cycle to investigate primary system performance criteria of power, efficiency, and reliability indicators. The 20 W planar cell is the focus of this section as shown in Figure 2.3.

The planar geometry is a cross-flow, electrolyte-supported cell based upon an in-house experimental stack. The model is discretized with one node each for the solid, air, and fuel layers with a single cell used as representative of all cells. Thermal conduction is considered in two directions within the plane of flow. The stacking direction is not considered, and all boundaries

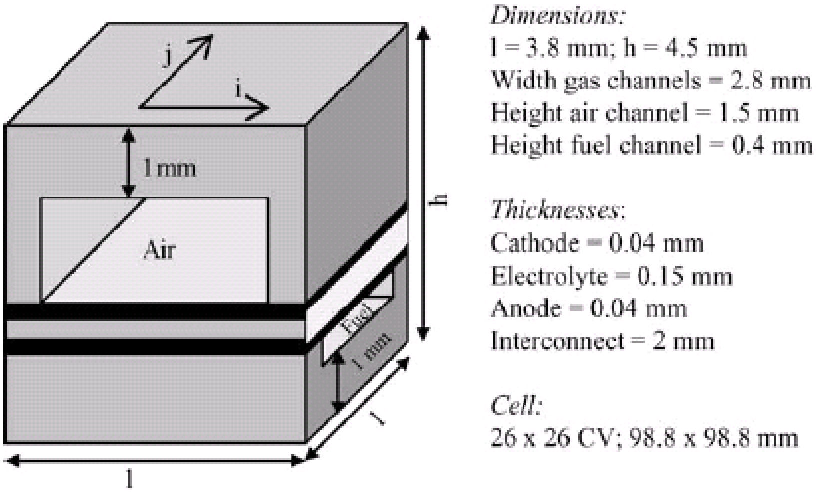

Figure 2.3: A schematic of the unit-cell for a cross-flow planar SOFC modeled by Stiller [70]

are adiabatic besides radiation from cell edges to the pre-reformer; the pre-reformer is modeled separately and linked to the SOFC model with a total heat flow term. Radiation to the prereformer is calculated as grey-body radiation with an emissivity of 0.8. Radiation is not considered within the planar cell; authors' note that other literature cite a need for radiation in planar models to model the temperature profile more accurately [79], but the assumption is made expecting that system properties of utilization, efficiency and power will remain accurate. Heat and material generation terms occur from the internal reformation and gas shift reactions. The reformation reaction is based upon a rate expression developed by Rechnenauer and Achenbach, which is a linear function of the methane partial pressure and a rate constant characterized by the Arrhenius equation as is common [63]. The water-gas shift reaction is considered to be at equilibrium because of the quick reaction rate at the high operating temperatures. Overpotential is a function of ohmic and activation losses; concentration losses, also known as diffusion losses, are not considered. The cell voltage is a model input used for calculating local current values. The fuel utilization, or current, can be used as a model input instead of voltage, but an iterative approach is required to modify the voltage until utilization convergence is reached. Current is an implicit state as a function of fuel utilization, fuel flow, and inlet fuel concentration. The authors evaluate the possibility of carbon deposition by checking whether the Gibbs free energy of the coking reactions is less than zero; the two coking reactions involve CO and CH_4 as precursors.

Validation of Stiller's planar model is performed by comparing results to models by Rechnenauer [63] and Selimovic [66] using inputs from an IEA Benchmark test [1]. A key difference between planar and tubular inputs is the higher excess air ratio for the planar case due to a higher reliability risk from thermal gradients. Simulation results indicate that the planar model fit well to published data with a voltage deviation of 2 percent. The models were solved using a Newton-Raphson iterative procedure using partial derivatives.

Aguiar, et al., presents results for one-dimensional models of co-flow and counter-flow medium-temperature anode-supported planar SOFC cells with direct internal reforming of methane [3]. The authors use this model to investigate the change in fuel utilization, current density, inlet temperature, and flow configuration on steady-state and dynamic performance. Dynamic results are presented in a subsequent publication and are described in the control section [4]. The model represents a single cell located within the center of a stack, and end effects are neglected. The EEA composite is considered as a single layer within the energy balance. Pressure drops along the channels are ignored. Five species are considered within the fuel channel: H_2O, CO_2, CO, CH_4, and H_2; O_2 and N_2 are considered for the air channel. Only hydrogen oxidation is considered in the electrochemical reactions. The three common reaction mechanisms are considered: steam reformation, water-gas shift, and hydrogen oxidation on the anode-side. The authors provide a summary of methane reformation reactions for various DIR catalysts. The first-order methane reaction rate proposed by Achenbach and Riensche [2] is used in their model as shown in Equation 2.3:

$$r_{CH_4} = \ A \exp\left(-\frac{E_a}{RT}\right) p_{CH_4} \quad [mol\, m^{-1}\, s^{-1}] \tag{2.3}$$

with a rate constant of $A = 4274\, mol\, s^{-1}\, m^{-2}\, bar^{-1}$ and activation energy of $EA = 82\, kJ\, mol^{-1}$. The water gas shift reaction is also presented in their work. Heat flow within solid parts is modeled with conductive transport, and heat flow between solid and gas layers is modeled as convective transport. A constant Nusselt number is used given the laminar flow assumption. Radiation is considered between the interconnect and EEA assembly, and the radiation geometry is modeled as two infinite parallel planes. A prominent assumption in this work is constant gas densities and heat capacities. These latter parameters have a non-trivial effect on the temperature gradient.

The model power densities are shown to be in a similar range as previously published results. Past literature has shown that peak power with hydrogen ranges between $1.08\, W\, cm^{-2}$ and $1.58 W\, cm^{-2}$ at cell temperatures ranging between 973 and 1073 K; with humidified hydrogen peak power is at $0.49\,W\,cm^{-2}$, and with methane peak power is at $0.4\,W\,cm^{-2}$.

2.2.1.2 Dynamic Planar SOFC Models

Petruzzi, et.al., developed a three-dimensional transient model for medium-temperature, cross-flow 3.5 kW planar solid oxide fuel cells with the motivation of optimizing cell design and operating strategies for application as an auxiliary power unit within automotive vehicles; the research was performed in Munich at BMW AG [59]. The transient model is applied during heat-up and start-up operating phases as well as transients during normal operation. The model provides plots of combined temporal and spatial variation in temperatures, concentrations, electrical, and thermodynamic properties. The stack average temperature and power delivered are primary controlled variables, with fuel and oxidant flows as the primary manipulated variables. The source fuel is 24% hydrogen mixed with a carrier gas consisting of H_2O, CO_2, CO, and N_2, in order of increasing concentration; methane can also be included in the model. Key system design tradeoffs is having enough cells to increase voltage and reduce polarization losses as desired and few enough large cells to decrease the surface-to-volume ratio and reduce required thermal insulation.

Within Petruzzi's thermo-electrial SOFC model, the oxidation of hydrogen and carbon monoxide is considered, unlike the steady-state planar models reviewed in the previous section. While the presence of CO_2 increases the activity barrier for oxidation of CO, the presence of H_2O makes the favored reaction path generation of hydrogen by the shift reaction. Internal reforming and gas-shift reactions are also considered in the material and heat generation terms. The reformation model is not discussed, but the shift reaction equilibrium constant is calculated as a function of temperature [64]. Overpolarization losses are simplified as a linear function of current, and only ohmic and activation polarization are considered with concentration losses neglected. One important assumption is that ohmic resistance is considered constant; while this assumption significantly reduces computational issues, recent research has found that temperature-dependent ohmic resistance leads to steady-state multiplicity [10]. The equipotential assumption is applied across the length of the cell and for all cells and is a common assumption. Efficiency is calculated as the ratio of electrical power produced to the lower heating value (LHV) of the inlet fuel of CO, H_2, and CH_4. Pressure drops are neglected along the fuel and oxidant channel, and gas flow is assumed to be at steady-state conditions since the time constant is much lower than for solid components. The gas is assumed to be well mixed normal to the flow direction, and gas temperature variation is only considered along the flow direction. A global heat transfer coefficient is utilized to simplify several thermal transport processes, radiation, conduction between the interconnect and EEA, and convection between the interconnect and gas flow. In addition, heat transfer between the stack and insulation shell is modeled as convection. Petruzzi uses MATLAB stiff ODE solvers to solve the SOFC system model. The model results provided the following design guidelines: insulation and start-up times need to be improved for air processing unit application, a heat-exchanger is necessary to reduce start-up times, and air mass flow is a key manipulated variable for controlling the average stack temperature.

Xi presents a co-flow planar DIR SOFC dynamic model that demonstrates computational challenges associated with dynamic modeling of discretized SOFC systems and proposes an iterative solution scheme [76]. Voltage is selected as the iterative variable adjusted to move the solution towards convergence. The authors apply a quasi-steady state (QSS) assumption to the fuel and air energy and mass balances - these states are assumed to move instantaneously to changes in the slower solid temperature dynamics. This assumption contributed to reducing the model order from approximately 160 to 16 states; however, the QSS assumption introduces a set of coupled non-linear algebraic equations that may negate computational gains by order reduction - an efficient algebraic solver is important. The model permits the six common chemical species found in fuel, same as Petruzzi's model. Additional assumptions are ideal gas flows, an equipotential assumption across the cell length, adiabatic cell boundaries, a constant Nusselt number, hydrogen is the only species undergoing electrochemical oxidation, and reformation and water-gas shift reactions are the only other reactions occurring in the fuel channel. The authors simplify the energy balance by combining all solid cell layers into one EEA layer and neglecting the fuel air chamber as a temperature layer; the air chamber is considered as the only other temperature layer. Neglecting the fuel chamber is a prominent assumption since it is well known that having variable properties, such as specific heat capacity, in the fuel chamber is critical to producing an accurate temperature profile throughout the cell.

The Xi model is used to demonstrate the open-loop dynamic response of the co-flow planar SOFC. The current is stepped up from 4000 to 8000 A/m^2 followed by a later step decrease back to 4000 A/m^2. The voltage decreases with increasing power and shows the jump discontinuity followed by a first-order response characteristic of numerator dynamics. The maximum cell temperature and gradient increase with increasing power and decrease with decreasing power with a second-order response having minimal overshoot.

2.2.1.3 Steady-State Tubular SOFC Models

Campanari presented a steady-state model for a tubular high-temperature DIR solid oxide fuel cell in 2001 and 2004 based upon the Siemens Westinghouse design; note that the cell design and many parameters from the Campanari model in both articles [16, 17] are used as a foundation for the tubular SOFC model presented throughout this dissertation, and differences are highlighted in this review. In the first paper (2001), Campanari details a thermodynamic analysis of the full tubular SOFC system, with the fuel cell, ejector, and prereformer as shown in Figure 2.4. This system is calibrated for a 100 kW plant with 48% LHV efficiency, which includes the energy consumed by the blower and fuel compressor; this efficiency matches well with the Campanari model predicted efficiency of 48.5%. The authors note that the primary way to modulate cell power production is by controlling the current density, air utilization, and fuel mass flow; voltage and fuel inlet pressure can substitute for current density and fuel mass flow although voltage does not move linearly with air utilization as with current. Campanari performed a parametric analysis of different operating strategies. As compared with constant fuel utilization operation, using a constant air flow produced higher fuel cell exhaust temperatures and higher power generation per air flow, specific generation, which is beneficial for lowering plant capital costs although at a less than one-percent decrease in electrical efficiency. Operating at higher fuel

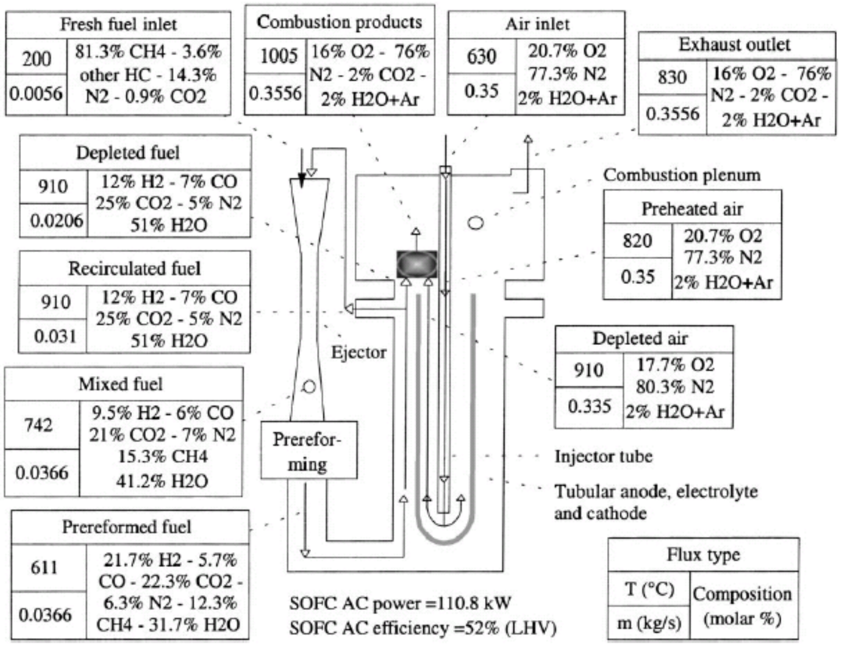

Figure 2.4: Schematic of the full SOFC system with an ejector and prereformer [16]

utilizations leads to lower specific power generation. The authors also find that it is ideal to operate with the lowest allowable steam-carbon ratio to reduce the fresh fuel pressure needed.

In addition to the thermodynamic model, Campanari presents a finite-volume model for the tubular solid oxide fuel cell [17]. In this work Campanari provides an exhaustive table of SOFC parameters and equations necessary for first-principles modeling of the SOFC. He uses an iterative approach to converge two models, electrochemical and thermal, consecutively to produce steady-state results. The model represents a single cell, as shown in Figure 2.5, located within the center of a stack without boundary heat loss.

As shown in Figure 2.5, the fuel flow travels upward in the space be-

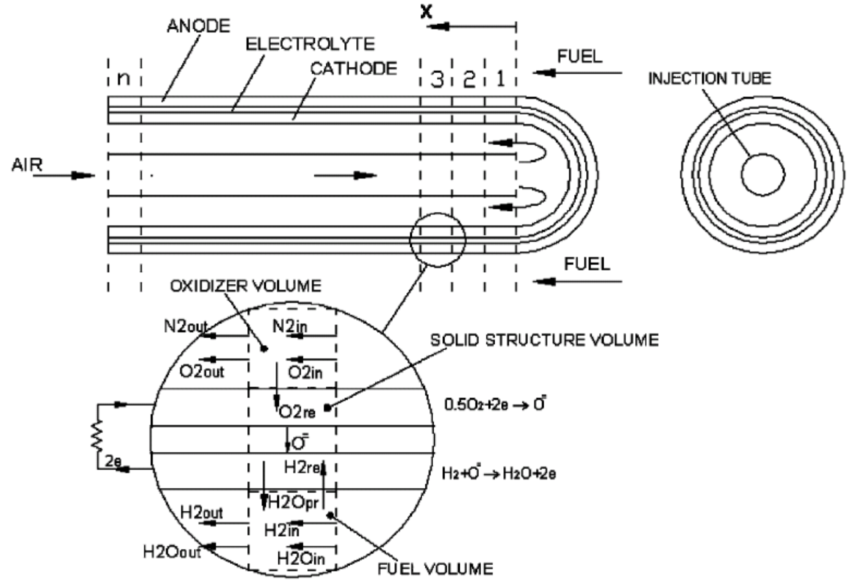

Figure 2.5: A cell cross-section for the Campanari model with finite-volume discretization rotated 90° [17]

tween cells along the anode; air flow enters an injection tube at the tube top, travels downward within the injection tube, and turns 180° to travel upward along the cathode as the electrochemical reaction begins. The electrochemical model makes the equipotential assumption. The Nernst equation differs somewhat from that used by other authors, and the current dissertation model uses a common Nernst equation form as used by Stiller [69]. Ohmic, activation, and diffusion polarization losses are considered.

Within the thermal model, the EEA is modeled with a single finite volume in the radial direction though the different material properties are considered. The reformation reaction is a function of both methane and steam partial pressure; the shift reaction is assumed to be at equilibrium. The cell ohmic resistance temperature-dependency is included in this model. Specific heats are taken as a linear function of temperature, as shown in Equation 2.4, with coefficients calculated by interpolation:

$$h_i = a + bT \tag{2.4}$$

Gas and thermal conductivities are likewise calculated as a function of flow conditions. Nusselt numbers are derived using a computational fluid dynamics (CFD) analysis, and constant Nusselt numbers are applied to the anode side, 4.2, cathode side, 5.5, and injection tube, 11. The CFD analysis showed laminar flow on the anode side and conditions within the transition region on the cathode side and injector tube. An important assumption in the thermal model is the absence of radiation between the injector tube and cathode; the assumption is based upon the expected magnitude of convective heat exchange versus radiative heat exchange. The current dissertation has deviated from the Campanari model by including radiation since radiation is seen to have a significant effect on gas and solid temperature profiles.

The Campanari model is validated using published performance data for two SOFC plants each taken at the operating conditions: (1) a 100 kW atmospheric prototype plant, and (2) a 300 kW pressurized hybrid turbine-fuel cell plant. Power, current density, air utilization, and fuel utilization are chosen as validation criteria, and the model results indicate that the Campanari model matches with three-percent error or less for all criteria. Plots of temperature, species concentration, and electrical states are shown in Figure 2.6.

Campanari's results produce several conclusions, which are consistent with other published results:

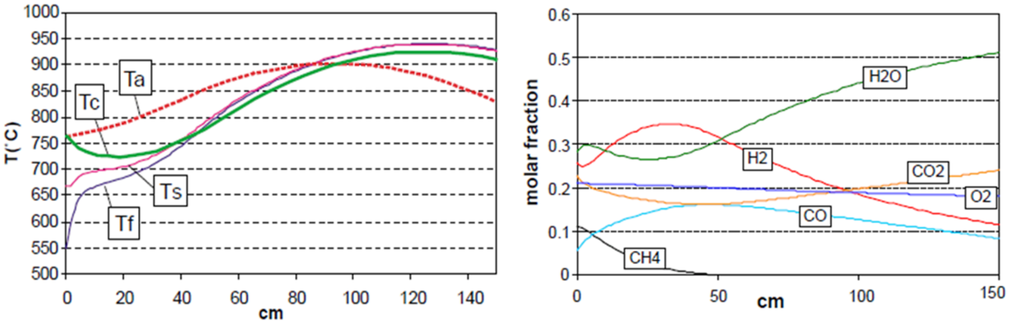

Figure 2.6: Campanari steady-state analysis along the fuel cell axial direction [17]

- The EEA temperature curve exhibits a sinusoidal-like shape with a decrease near the fuel inlet due to endothermic steam reformation reactions occurring at the anode, an increase due to electrochemical and ohmic heat generation, and a final slight decrease as the EEA approaches the cooler air inlet.

- The methane is fully reformed near the fuel entrance within one-third of the cell length, thereby contributing to the change in EEA temperature from decreasing to increasing in the first third of the length. Hydrogen production likewise peaks at this location.

- A peak in the cell current occurs near the first third in length also. The ohmic polarization likewise peaks near the same location, and all polarization losses continue to decrease as the EEA temperature increases.

Li presents a tubular SOFC model with two-dimensional axial-symmetric analysis of a single cell unit and validated against data for three different SOFC plants [47]. The Li model does not assume constant heat and mass transfer conditions along the EEA surface but rather uses local balances with a discretization of 602 volumes in the axial direction to represent the transport phenomena. A two-step iterative algorithm is used with temperature, pressure, and mass-fractions fed to the electrical model to calculate potentials and current, and these are then used within the governing equations to calculate temperatures and mass-fractions. The three common reactions, steam reformation, water gas-shift, and electrochemical, are considered; only hydrogen oxidation is considered in the electrochemical reaction. Equations for the equilibrium constants are provided. The electrical potential is calculated with a three-dimensional grid using Kirchoff's law. Radiation is modeled per existing literature [11].

The EEA axial temperature profile from Li's model using prereformed methane fuel matches well with a measured temperature profile by Hirano, illustrating a peak temperature that is shifted closer to the axial center of the cell and a more significant decrease in temperature towards the anode chamber exit. The difference with Campanari's temperature profile is likely due to the inclusion of radiation, and a comparison with and without radiation for the current dissertation model is shown in the simulation steady-state validation section. With the hydrogen fuel cases, the cell temperature profile becomes more evenly distributed as the current density increases. This effect occurs as the air flow rate increases thereby increasing cooling of the closed-end of the fuel cell. A difference with Li's model is that the hydrogen concentration decreases monotically even with a 27.7% methane mole fraction in the feed; this may be caused by the chosen form of the reformation reaction, which is implied to be at equilibrium for Li's model.

Stiller proposes a two-dimensional tubular SOFC model to investigate the effect of pressure ratio, air inlet temperature, air flow rate, and anode gas recycling on steady-state performance [71]. The SOFC is combined with a gas turbine in a bottoming cycle. The tubular cell is based on the Siemens Westinghouse design, consistent with Campanari, having a 1.5 m length and 22 mm outer diameter. The fuel cell model represents a single cell with adiabatic boundaries besides a lumped radiative heat flow with the prereformer. Unique finite volumes are used for anode, cathode, and injection tube gas layers, an injection tube solid layer, and a combined EEA solid layer. The potential model includes activation and ohmic losses while neglecting diffusion losses which are lower in magnitude. All EEA layers are modeled with temperature-dependent ohmic resistance unlike in Stiller's planar model; this approach is used due to different production techniques for tubular cells. Thermal conductivities of EEA layers are taken as constant; Nusselt numbers are considered constant assuming laminar flow. Axial heat conduction is modeled using the temperature at the thermal center, the radius where thermal resistance is equal inside and outside the radius. Radiation is considered between the injection tube and cathode in a similar manner as used in the current dissertation. The steam reformation model is based on Achenbach's mechanism which is a linear function of methane partial pressure, same as is used in the current dissertation.

Dokmaingam, et al., developed a mathematical model of an indirect-internal-reforming (IIR) tubular SOFC with counter-flow configuration and investigated the effect of different fuels, methane, biogas, methanol, and ethanol, on thermal states and power generation performance [24]. The tubular cell in this model is distinguished from the Siemens-Westinghouse plant in that an internal fuel reformer is the center tube within the cell assembly. This geometry is based upon the design by Aguiar, 2002 [5]. The fuel flow undergoes a 180° turn to reach the anode surface as it flows in the same direction as the air flow exterior to the cathode outer diameter. Key assumptions from this model are constant axial cell potential, diffusion and pressure drops are ignored, ideal gas behavior, and a final fuel utilization of 80%. Material properties are taken from the work of Zhu [81]. The authors justify only considering H_2 oxidation, not CO oxidation, by stating how the rate of CO oxidation is three times lower. Radiation between the inner tube, reformer, and EEA is considered, in addition to conduction and convection.

The steady-state comparison of an IIR SOFC operating with different fuels indicated that the highest efficiencies are obtained respectively with methanol, methane, biogas, and finally ethanol with the lowest efficiency. However, methanol requires the highest volumetric flow rate whereas methane requires the third-lowest. This report also indicated that methanol produced the lowest axial temperature gradients and lowest temperature difference between fuel and air chambers; the final observation would likely lead to the lowest radial thermal gradients though this is not indicated in the article. The study is performed using a constant load voltage of 0.7V, fuel utilization of 80%, and steam-to-carbon ratio of 2.0; however, the authors do not indicate whether each case produces the same power. The authors also performed a study of operating pressure, steam-to-carbon ratio, flow direction, and carbon dioxide content in biogas. A higher electrical efficiency results from higher pressures. An increasing steam-to-carbon ratio ameliorates the entrance EEA cool spot with a side-effect of decreasing electrical efficiency. The co-flow configuration exhibits reduced temperature gradients and higher electrical efficiencies than the counter-flow configuration due to improved thermal matching between heat required for endothermic reformation reactions and heat produced by exothermic oxidation reactions. Varying CO_2 concentrations in the biogas produces lower efficiencies at higher CO_2 concentrations; in addition the axial temperature profile changes significantly, and thermal cycling may occur.

2.2.1.4 Dynamic Tubular SOFC Models

Hall developed an early dynamic tubular cathode-supported SOFC model for high-temperature operation and the same configuration as the Siemens SOFC [33]. The model is a distributed parameter model with volumes in the axial direction, and the cell temperatures are chosen as the dynamic states with all other states at quasi-steady-state. The electrochemical model incorporates ohmic, activation, and diffusion losses and is validated using published data from Singhal [68]. The energy model includes heat transfer by conduction, convection and radiation. Axial conduction is ignored by the authors. Radiation is modeled as transfer between the inner air tube and EEA and between adjacent cells; the author concludes that radiation is a significant thermal transport effect. Euler-based time difference equations are used to reduce the differential equations to algebraic equations. The transient model alternates between electrochemical and thermal calculations. Hall performs dynamic simulations by introducing a current density step-change, representative of a load change, and reports the dynamic response of voltage, maximum cell temperature, and minimum cell temperature. As shown in Figure 2.7, the results indicate a settling time approaching 5000 seconds for thermal properties and 3600 seconds for electrical properties. The dynamic response shown

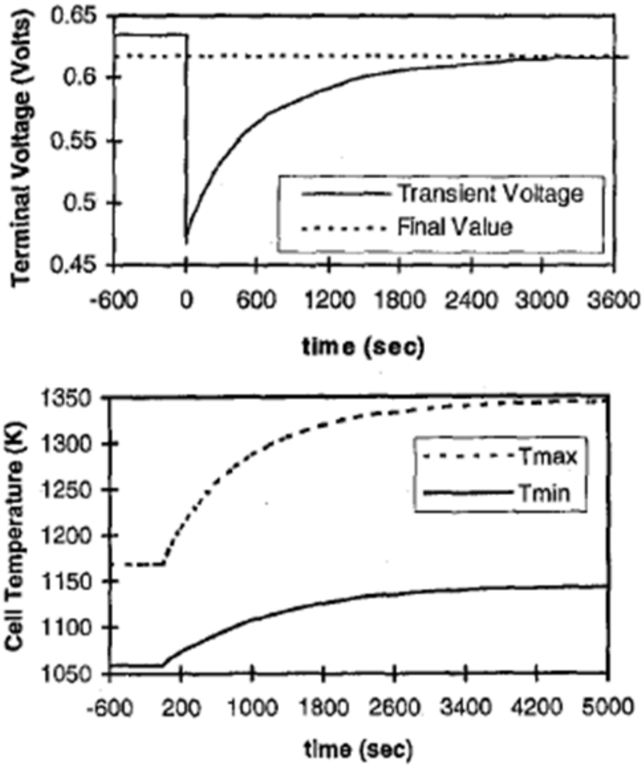

Figure 2.7: Dynamic response of voltage and cell temperatures in Hall's SOFC model [33]

by Hall is one of the earliest reports of dynamic tubular SOFC performance. Though in this case, the minimum and maximum cell temperature move in the same direction for a power increase, these temperatures do not always move in tandem for power increases. For instance, the case of increasing fuel flow to increase power will cause the minimum cell temperature to decrease when the fuel flow is at a much lower temperature than the EEA temperature. The temperatures likely move in tandem because Hall does not model internal reformation, which causes a cool spot due to endothermic reactions. Hall's model mentions the SOFC being powered by reformed hydrocarbon fuels consisting of hydrogen and carbon monoxide.

Thorud, Stiller, et al., developed a dynamic quasi-two-dimensional, distributed parameter tubular SOFC model based on available data for the Siemens design [73]. The model is the prime mover for a system comprising nondimensional prereformer, ejector, and afterburner models. The prereformer model is a Gibbs reactor and receives heat exchange from the fuel cell anode via radiation. Energy and material balance modeling within the fuel cell is consistent with the steady-state tubular SOFC model by Stiller [71]. The authors' use of the model is to develop steady-state performance maps of fuel cell states during part-load operation and to investigate dynamic response to load-following.

The dynamic simulations involve a load decrease of 100% to 55% and load increase from 55% to 100% using two independent open-loop control strategies, constant air utilization (UA) and constant fuel utilization (UF), for a total of four simulation cases; in each case, the non-constant utilization and air flow is linearly adjusted to reach the desired steady-state power. Settling times for the dynamic simulations range from 1,000 s for constant UA to 20,000 s for constant UF. The afterburner exit temperature is an important variable as it is also the turbine inlet temperature (TIT) in a GT-SOFC configuration. The constant UF modes in both load-change directions produce a more constant initial and final TIT temperature although the load decrease causes a spike in TIT; the constant UA mode causes a near first-order decrease/increase for a load change decrease/increase. The maximum radial thermal gradient moves in the same direction as the load-change for both constant UA and UF modes; this can be explained due to how local current flow increases with power leading to increased heat generation. Air and fuel utilization moves the opposite direction as the load-changes and exhibits minor numerator dynamics. The mean fuel cell temperature exhibits the slowest settling time due to thermal mass and low thermal conductivity of ceramic EEA materials.

Xue presents a dynamic, distributed parameter model of an anode-supported high-temperature tubular SOFC with fuel and air in a counter-flow configuration [78]. In Xue's model, fuel flows through a center tube with air flowing in the outer concentric ring; an insulation layer comprises the outermost layer. The cell is discretized in a quasi-two-dimensional manner such that each layer, cathode chamber, EEA, anode chamber, and insulation are each modeled as one-dimensional, lumped control volumes per axial segment; solid control volumes involve an energy balance while gas control volumes involve momentum, species, and energy balances with an ideal gas assumption. The authors do not mention employing a quasi-steady-state assumption to reduce mass or momentum dynamic equations. Radiation between the cell and thermal insulator is modeled with an infinite length concentric cylinder approach, and energy is permitted to leave the system via convection external to the thermal insulator. The electrical circuit is modeled as a set of independent sub-circuits with the polarization losses captured with ohmic and activation polarizations. A unique feature of their model is how the Nernst voltage is modeled as a discontinuous function of two unique equations.

The dynamic response to a load step-change indicates a simultaneous current-overshoot and a delayed overshoot with decreasing hydrogen flow rate and increasing steam vapor partial pressure. The cell temperatures increase under higher currents and power load. The slowest time constant is approximately 4000 s as driven by the solid thermal inertia.

Barzi presents a dynamic distributed parameter model to investigate the start-up behavior of a tubular SOFC [8]. The start-up procedure begins as warm air is passed through both chambers of the fuel cell until the cell reaches a minimum operating temperature in the range of 600-900°C; this minimum temperature ensures a sufficiently high ionic conductivity for electrical transport. The cell is connected to the external load, and power levels are increased to the nominal operating load. Issues considered in setting the heat-up time and profile are the absolute temperatures and gradients and power consumed during heat-up.

The system modeled is in the same geometrical configuration as the Siemens tubular SOFC but having smaller dimensions. The electrical model considers ohmic and activation losses; diffusive losses within the channel are considered within the mass transfer model, and diffusive losses within the porous electrodes are neglected due to the significantly lower magnitude versus other losses. A three-dimensional nodal network in radial, longitudinal, and circumferential directions based on the Kirchoff law models the potential distribution. The authors present a transient model for mass, momentum, and heat transfer model and mention that a finite volume approach is used for discretization. Density, viscosity, specific heat, and diffusivity terms are calculated as a function of local temperature, pressure, and concentrations. Adiabatic and impermeable boundaries exist at the boundary of the single cell model due to symmetry. The authors use an iterative solution procedure at each time step such that electrical, heat and mass sources, and conservations equations are solved sequentially until convergence is reached at the given time.

Barzi validated his model by comparing the polarization I-V curve to experimental data by Hagiwara and a model by Li. Barzi's results are more than 5% accurate than Li's model and match the data within 12% to 0.25% respectively as the current density increases. The heat-up simulation is performed over 2.5 hr in simulation time and causes a maximum temperature rise rate of 30° C/min; the rate that causes thermal shock is 1-2°C/min. Two dynamic simulations are performed such that the initial conditions are different before connecting the cell current at 104 A: (1) the fuel and cell temperatures are at 900°C and air temperature is at 600°C; (2) the fuel, cell, and air temperatures are all at 800°C. For case one, the temperature profile at the end of the heat-up phase is flat, and as electrical power is increased, the temperature profile gradually becomes convex with a steeper profile; the maximum temperature also shifts from near the entrance to the outlet as shown in Figure 2.8.

The start-up time for both cases is the same, requiring about ten thousand seconds each for both the heat-up and electrical load steady-state phases. The cases differ in how under case one the voltage curve exhibits numerator dynamics with a positive zero such that the voltage initially decreases from

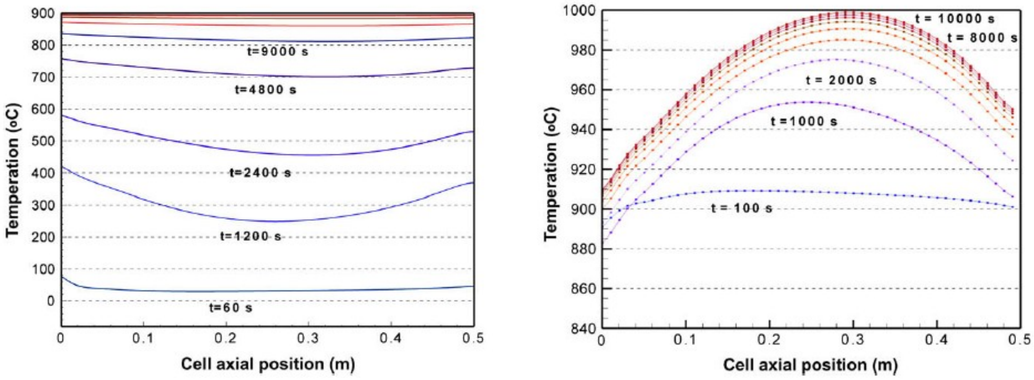

Figure 2.8: Case one, heat-up period ends with a flat cell temperature profile (left); temperature evolution after the electrical circuit is connected at 104 A (right). [8]

zero time before increasing past the initial value; in case two, the voltage increases monotonically with first-order dynamics. This study indicates the SOFC nonlinear dynamics as the initial condition affects the input-output transfer function. Another key observation from this study is that the species, electrical, and thermal response times may differ during the same case; for case one, species settling time was 16 min while voltage was 50 min and the cell temperature is increasing until 130 min.

2.2.2 Ejector

The ejector operates with three main steps: (1) accelerating the primary inlet flow to supersonic speeds and thereby accelerate a slower, secondary (entrained) inlet flow using a converging nozzle; (2) mixing the flows to have a homogeneous flow velocity and temperature, and (3) raising the mixed fluid static pressure by converting kinetic energy to potential energy in the form of pressure. The primary fuel nozzle and overall ejector geometries are both de Laval nozzles. A schematic of the ejector as modeled by Marsano, 2004, is shown in Figure 2.9.

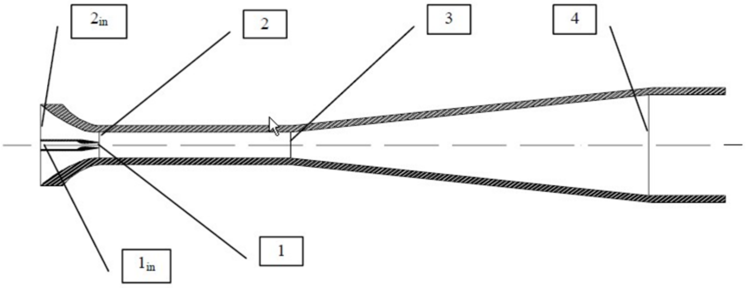

Figure 2.9: Ejector cross-section for the one-dimensional Marsano model [51]

Ejectors in an SOFC anodic recirculation circuit are characterized by a high entrainment ratio, low pressure increase, and exposure to high temperature gases and a different chemical composition than typical ejectors. Inlet primary fuel temperatures to the ejector are in the range of 400-600°C, and inlet secondary (entrained) fuel flow is near 1000°C. The SOFC ejector cannot be modeled accurately using the same approach as traditional ejector models for the reasons cited. The SOFC ejector must serve several necessary purposes as noted by Marsano: (1) maintain the fuel cell inlet pressure at sufficient levels for proper circuit gas recirculation; (2) provide sufficient heat via steam flow to the prereformer to drive the endothermic reformation reactions, and (3) provide sufficient steam concentration to the fuel cell to prevent carbon deposition and subsequent catalyst poisoning [51].

Marsano models the ejector using 1D, steady-state balances for energy, mass, and momentum; energy equations are composed of enthalpy and kinetic terms. Though the model considers properties at several locations within the ejector, the model uses a lumped approximation as only one equation is used for each set of conservation equations. Marsano creates the model for use in designing the ejector for ideal and off-design performance within the SOFC anodic recirculation system. The model assumes adiabatic walls and uses an iterative method to match outlet pressure by adjusting the inlet pressure and geometry. Marsano considers several design constraints: (1) the design value of the steam-carbon ratio is 2.4 with a lower limit of 1.8; (2) a conical diffuser shape is chosen due to size restrictions in the SOFC system and computational feasibility, and (3) the mixer length is set to 10 times the mixer diameter to ensure a homogeneous diffuser inlet velocity profile. The latter assumption is critical to prevent boundary layer separation and diffuser backflow. Marsano analyzed two geometries, a constant mixing pressure and constant mixing geometry ejector. The design results produced very similar geometries with rounded, approximate sizes as follows: mixing length of 0.2 m, mixing diameter of 0.02 m, diffuser length of 0.45 m, and diffuser diameter of 0.1 m.

Marsano also performs an off-design analysis with the primary flow inlet pressure as the manipulated variable. The results show how the pressure delta as produced by the ejector decreases as the mass flow rate increases, but the constant section mixer design provides a somewhat slower decrease in the pressure delta than with the constant pressure mixer. Marsano concludes with several additional observations for ejector operation with a SOFC system:

- As SOFC operating pressure is decreased, the steam-carbon ratio also decreases at air and fuel mass flow rates higher than the design point.

However, the lowest steam-carbon ratio occurs at very low air and fuel flow rates.

- Prereformer efficiency, as defined by the decrease in methane molar flow rate normalized by inlet methane molar flow rate, is very dependent on the ejector performance as efficiency increases with higher temperatures and inlet steam concentrations Efficiency is increased overall with greater mass flow since the steam concentration increases with greater secondary mass flow.
- Increasing the primary and secondary fuel flow inlet temperatures leads to a decrease in ejector outlet mass flow.
- A reduction in fuel utilization, which may be caused directly by reducing current and power, will lead to a decrease in steam-carbon ratio.

Zhu provides a very detailed description of a steady-state SOFC ejector model that evaluates gas velocity using a 2D equation while the overall model remains 1D [82]. The 2D velocity calculation is included to model more accurately the mean secondary flow velocity in an SOFC ejector; the secondary flow area is much larger for this application, and absolute errors may exceed 15%. The primary differences between Zhu's model and Marsano's model are that the mass flow rate is calculated from isentropic flow relations and the secondary flow is modeled as two-dimensional. As a result of the two-dimensional modeling, Zhu states that modeling flow inside the mixing chamber and diffuser are unnecessary, thereby reducing computational cost. The Zhu model is composed of nine algebraic equations that may be solved sequentially although the Mach number terms are solved using optimization on implicit equations. Key assumptions of the Zhu model are listed as follows: secondary flow velocity is non-uniform in the radial direction with a boundary layer near the ejector wall; the primary flow is uniform in the radial direction and has a much smaller flow area than the secondary flow; adiabatic walls; the primary flow reaches the secondary flow inlet temperature at the mixer inlet, and the secondary flow remains constant over the region; ideal gas flows; isentropic relations are accurate; and uniform pressure and temperature in the radial directions. The ejector model provides outputs consisting of the entrainment ratio, steam-to-carbon ratio, outlet temperature and concentrations.

Zhu validates the ejector model versus Marsano's ejector at on-design conditions and finds that the maximum difference between model results is 1.94%. The off-design investigation is performed in comparison to a Freon-based experiment and is valid in the critical mode, in which the ejector operation should reside. The study confirmed that the primary mass flow increases and secondary mass flow decreases in a logarithmic manner to a steady value with increasing inlet fuel pressure. Marsano's 1D model predicted that the secondary flow and entrainment ratio would increase with increasing fuel pressure; thus, in comparison to experimental data, the 2D model is shown to be more accurate in predicting total mass flow. The effect predicted by Zhu's model is due to how the secondary flow area at the mixer entrance reduces as primary fuel pressure increases; the secondary flow velocity is near constant in the critical model, and an increase in fuel pressure causes an increase in primary flow area.

Zhu also investigated the effect of integrating the ejector into an SOFC model. A primary difference in the SOFC study is that the secondary flow temperature and concentration are no longer constant but must be computed simultaneously with the SOFC model. These two variables are shown to affect the entrainment ratio by 0.72% at a constant pressure versus the stand-alone model but affect the steam-to-carbon ratio (SCR) by 18.8%. The SOFC power increases with increasing fuel inlet pressure but shows a diminishing increase and a near constant value at the design point of 10 bar; this effect highlights the importance of designing the ejector to provide the desired fuel cell controllability in particular since fuel inlet pressure is a critical manipulated variable for cell power output. The SCR ratio moves directly with the fuel cell pressure and indirectly with the fuel inlet pressure. Zhu chooses an SCR of 1.8 as the limit below which carbon deposition occurs. As fuel inlet pressure is increased to 13 bar, the SCR decreases below the limit for system pressures of 3.6 bar and below. At fuel utilizations below 0.8 the SCR again decreases below the carbon deposition limit.

2.2.3 Prereformer

The prereformer serves to convert higher hydrocarbons to methane and hydrogen through steam reformation and partially convert methane to hydrogen upstream of the fuel cell stack. Partial methane reformation has an additional benefit of reducing temperature gradients, the primary reason that SOFC systems may incorporate an internal reformer producing an inlet methane concentration approaching zero.

Stiller presents a detailed model of an SOFC prereformer modeled as a lumped, adiabatic Gibbs reactor [69]. The reformer model operates as quasi-steady-state and is based upon a two-step steam-reformation and water-gas shift reaction. A pressure drop can be calculated using a constant flow coefficient and inlet mass flow, molar flow, and density. Heat input to the pre-reformer may originate from either solely the inlet fuel flow or radiation from the SOFC [71].

2.3 SOFC Control Strategies

2.3.1 Control Objectives

The control strategy for the solid oxide fuel cell is critical to meeting the energy and cost demands required by fuel cell end-users. Primary goals for SOFC control are matching delivered power to external loads, operating at high efficiency, and ensuring an acceptable cell lifetime. To achieve these ends, researchers and practitioners choose among controlled variables that include power, voltage or current, cell temperatures, cell temperature gradients, fuel/air utilization, steam-to-carbon ratio, and outlet fuel/air flow temperatures. High-level manipulated variables may include inlet fuel/air concentration, flow rates and temperatures, system pressure, and current or voltage. These variables are controlled at the physical plant level by means of control valves, compressor or motor speeds, and power management controls. Additional auxiliary equipment such as natural gas processors, gas turbines, and additional grid elements including energy storage or renewable energy, may also be introduced into the control problem at multiple levels in the control hierarchy.

Achieving optimal operation with regards to simultaneous goals of load-following, efficiency, and reliability involves solving a multivariable constrained optimization problem. Most controlled variables are affected to a significant degree by multiple manipulated variables. The power output for a counter-flow, tubular SOFC without an air supply tube is affected by inlet fuel pressure and temperature, system pressure, and voltage/current. Likewise, these manipulated variables also affect cell temperatures and temperature gradients. The manipulated-controlled variable interactions are system-specific and dependent on fuel cell geometry, flow configuration, and material selection among other design parameters. For example, air flow may affect critical temperatures and gradients in anode-supported tubular cells but may have an insignificant effect on these CVs in cathode-support tubular cells. Besides gain interactions, controlled variables may have a very different time response to the same manipulated variable. Temperature gradients may change significantly within seconds though the local temperature may drift more slowly in a first-order step-response manner. The differences in multivariable responses are a primary justification for deciding the extent to which the controller is centralized, the combination of MIMO and SISO controllers used.

Besides multivariable interactions, physical plant nonlinearities also present a significant challenge for SOFC control. Researchers have discovered incidences of steady-state multiplicity for planar SOFCs [10]. The SOFC manipulated-controlled variable interactions are characterized by nonlinear gains which will reduce the accuracy of control models identified about a single operating point; nonlinear gains are evident in open-loop results by Aguiar [4]. Approaches to address nonlinearities may include nonlinear model predictive control using grey-box models or empirical models, such as Hammerstein models, or adaptive control [22].

2.3.1.1 Reliability Control

SOFC controlled variables related to reliability issues are anode backflow, fuel and air utilization, absolute temperatures, temperature gradients, and the steam-to-carbon ratio; the importance of each of these is described in the following. Anode backflow is the scenario whereby spent fuel flow from the downstream plenum back into the anode chamber and can occur during rapid pressure changes. Excessively high fuel or air utilization can result in fuel or air starvation. In the case of starvation, sufficient fuel or air does not reach the reaction site and local voltage drops simultaneously; cell degradation may occur due to oxidation and reduction occurring within the electrodes, reversal of cell potential, or catalyst corrosion [28, 65].

Cell thermal management is critical to fuel cell durability and both absolute temperatures and temperature gradients may affect fuel cell lifetime via thermal stresses. Fischer investigated thermal stresses within a cathode-supported tubular SOFC using a 2D finite-element mechanical model combined with a thermo-electrochemical model [30]. Study results found that a low local cell temperature is the primary contributor to high thermal stresses followed by high negative radial thermal gradients, i.e., a higher cathode than anode temperature; axial thermal gradients and positive radial thermal gradients are insignificant to thermal stresses for the cathode-supported tubular SOFC [30, 55]. The minimum cell temperature is a reliability issue due to the cell being sintered at higher than operating temperatures; thus, increasing the temperature relaxes thermal stresses. The results of this study are specific to the cell geometry, design, and fabrication referenced. Experiments have also found cycling to be a factor for crack growth in yttria-stabilized zirconia and nickel cermet materials for SOFC. Thermal cycling produces crack growth in a manner similar to fatigue with a dependence of crack length on log N, where N is the number of cycles; whereas, redox cycling of fuel flow induces more severe crack growth on the order of N [23]. Therefore, any control strategy should consider minimizing rapid cycling of manipulated variables, particularly fuel inlet pressure.

The steam-to-carbon ratio is important for reliability in order to mitigate carbon deposition. In the presence of high temperatures in the range of SOFC operation and low steam concentrations, methane and carbon monoxide may crack rather than undergo reformation and oxidation reactions, respectively, as shown in Equation 2.5:

$$\begin{aligned} CH_4 &\longleftrightarrow C + 2\,H_2 \\ 2CO &\longleftrightarrow 2C + O_2 \end{aligned} \tag{2.5}$$

2.3.1.2 Actuators and Sensors

The time response for actuators and sensors will affect controller performance if control sampling time is fast with respect to these. To control fuel/air utilization and the steam-to-carbon ratio, concentration measurements or estimates must be available for methane, hydrogen, steam, carbon monoxide, and carbon dioxide. A state estimator may also be used to reduce the number of concentration measurements necessary, but computational time for solution of the estimator must be considered. Response time of concentration, temperature, and pressure sensors relevant for SOFC control is less than 1 s [10]. Control valves commonly operate with acceptable variability on the order of 1-2% with a response time of 1 s [9]. A conservative estimate for microturbine compressor turbo lag is 1-3 s.

Table 2.2 summarizes the classical and model-based controllers that are reviewed in this section.

Table 2.2: Review of solid oxide fuel cell control literature

System	Controller type	Architecture	Model type (if applicable)	Manipulated variables	Controlled variables	Year published	Authors
Planar SOFC	PID	Multi-loop SISO		Air flow, fuel flow	Outlet gas temperature, average current density	2005	Aguiar, Adjiman, Brandon [4]
GT-SOFC tubular hybrid	PID	Multi-loop SISO		Current, fuel flow, turbine shaft speed, air flow setpoint	Power, fuel utilization, air flow, lumped cell temperature	2006	Stiller, Thorud, et al. [70]
GT-SOFC tubular hybrid	PI	Multi-loop SISO		Fuel flow, compressor air blow off	Power, lumped cell temperature	2007	Kandepu, Imsland, et al. [40]
planar SOFC	Model-based, RMS objective [a]	Multi-loop SISO + MISO	Steady-state 2D physics	Air utilization, inlet gas (fuel and air temperature)	Power, 1D temperature distribution	2006	Inui, Ito, et al. [37]
SOFC	optimal regulators	SISO	LTI state-space	Hydrogen flow	Power	2009	Sun, Ghantasala, El-Farra [72]
SOFC	MPC	MIMO	Hammerstein fuzzy model + ARX	Current, fuel flow	Power, voltage	2006	Jurado [39]
SOFC	MPC	Multi-loop SISO	Hammerstein, neural network + ARX	Current, fuel flow, oxygen flow	Power, voltage	2008	Huo, Zhu, et al. [35]
GT-SOFC planar hybrid	LQR	MIMO	LTI state-space	Current, GT power, fuel flow, combustor fuel flow	Temperature, voltage, GT shaft speed	2009	Mueller, Jabbari, et al. [52]
planar SOFC	H_∞	MISO	LTI state-space	Air flow, air inlet temperature	1D temperature distribution	2010	Fardadi, Mueller, Jabbari [28]
GT-SOFC planar system	PI	Multi-loop SISO		Current, fuel flow, two bypass valves, air bleed	Combustor temperature, power, air inlet temperature, stack temperature, compressor surge	2010	Mueller, Tarroja, et al. [53]
SOFC planar	MPC, NMPC	MIMO	State-space, first principles	Air, fuel, and steam flow	Voltage and cell temperature	2010	Murshed, Huang, and Nandakumar [54]
SOFC tubular	NMPC	SISO, MIMO	ARX, NAARX	Hydrogen flow, voltage	Power, fuel utilization	2010	Bhattacharyya and Rengaswamy [14]

[a] Uses a root mean square objective function

2.3.2 Classical Control

Aguiar presents a dynamic model and control results for a co-flow planar medium-temperature SOFC with a methane fuel source [4]. The model is based upon the Aguiar model described in the steady-state section for steady-state planar SOFCs. The dynamic simulations illustrate open- and closed-loop fuel cell response under load-following using the current density as a setpoint. A simple control strategy is implemented to change the fuel and air flow proportionally to the current in order to maintain constant utilizations. Two temperature PID control strategies are compared, one having a constant outlet temperature set-point and another having a temperature set-point that shifts proportional to the change in load. For both temperature controllers, the air flow rate serves as the manipulated variable. Open loop simulations demonstrate how the outlet gas temperature increases simultaneously with power increases and vice versa. As expected from the typical I-V curve, increasing power and current density produces a lower steady-state voltage; however, the dynamic voltage response illustrates numerator dynamics with a jump discontinuity and overshoot at the time of current density change followed by a first-order relaxation to the steady-state condition as shown by Aguiar. The power response likewise demonstrates a jump-discontinuity but without an overshoot.

Important conclusions arise from the Aguiar planar SOFC control study. The PID temperature controller with a fixed set-point is found to be unstable and produce oscillatory temperatures for load changes of increasing magnitude, 0.5 to 0.2 A cm^{-2}. For load changes with a magnitude less than 0.3 A

cm^{-2}, the temperature is controllable, but the temperature gradients increase and decrease respectively for decreasing and increasing power in a stable but uncontrolled manner. In the 0.3 A cm^{-2} power case, the gradient exceeds the author's limit. The PID controller with a heuristically-tuned adjustable set-point decreases the temperature set-point concurrently with a decreasing power set-point. This strategy allows the outlet temperature to migrate very near the open-loop steady-state temperature but to a controlled final steady-state value. In this second controller configuration, the temperature gradients remain near the open-loop gradient values as expected. Overall, the final controller produces very little change versus the open-loop response. An important conclusion from these results is that controlling the outlet gas temperature may not guarantee successful control of the SOFC reliability criteria, thermal gradients in this case.

Stiller proposed a control strategy for a hybrid system with tubular SOFC and gas turbine; he applies his strategy to a physics-based model of the GT-SOFC system implemented in gPROMS [70]. In addition to fuel cell reliability issues already described, Stiller notes hybrid system reliability objectives - preventing compressor surge and fuel cell degradation due to high local heat production rates. The latter issue can be mitigated by limiting current drawn from the cell. The control strategy should also be robust to drift disturbances such as cell degradation and compressor fouling. Stiller notes that standard controllability analysis is not applicable because the plant is strongly nonlinear difficult to linearize. Stiller's approach is to apply multi-loop SISO controllers: Power controlled by SOFC current in less than one second; fuel utilization controlled by fuel flow in a few seconds; air flow controlled by turbine shaft speed in one minute; and cell temperature controlled by air flow setpoint in minutes to hours. Current changes are assumed to be performed by the power electronics subsystem. Stiller permits fuel utilization to vary in the range of 75-90%; a lower utilization is used to ensure indirectly sufficient steam content. Stiller also sets a minimum voltage of 0.52 V to prevent passing the maximum point in the IV curve. Stiller implements the power and fuel utilization controllers using a multi-mode strategy to prevent constraint violations; the modes are as follows: normal operation, maximum UF, minimum UF, and minimum voltage. Temperature is controlled using inferential control whereby an exit gas temperature setpoint is calculated as a function of Power, ambient pressure, and ambient temperature. Stiller simulated small and large load steps, decreases and increases, defined by a 4.7% and 47% magnitude respectively followed by disturbance tests. The temperature control maintained the mean temperature within a bandwidth of 60K about the target; whereas power settles within 100 s, the temperature may require 10,000-100,000 s to settle. A change in fuel heating value and fuel cell degradation were found to be significant disturbances to operation; a fuel flow overestimation by 5% produces a maximum increase in mean temperature 45 K above nominal with a corresponding power increase. The Stiller multi-loop controllers address the control of SOFC mean temperature, fuel utilization, air flow, and power tracking.

Kandepu developed a comprehensive dynamic lumped GT-SOFC model including a two-stage gas-turbine, tubular SOFC, heat exchanger, reformer, combustor, inverter, generator, and grid, and he presents results for a decentralized PI controller as applied to the GT-SOFC system model [40]. He states that a dynamic SOFC model composed of two-lumped volumes in sequence is sufficiently accurate for his application as the dynamic plant in control studies by comparing results to a distributed dynamic model. The control objective is to provide autonomous load-following while mitigating temperature variation. Using a fixed voltage and allowing current and fuel utilization to vary results in uneven voltage and temperature distribution. The controls strategy involves a decentralized set of two PI controllers with power generation controlled with fuel flow as the MV and SOFC temperature variation minimized using an air blow off valve at the compressor outlet. The authors support the use of the air blow off valve as a superior MV versus additional combustor fuel or air bypass across the heat exchanger. To test the control strategy, the load setpoint is decreased with a first-order hold from 5 to 10 s; the system is allowed to reach a steady-state through 20 s, and the induction motor load is increased 50% in a step. Results indicate smooth control of power load in a first-order manner and SOFC temperature variation of less than 0.1 s. The authors acknowledge additional GT-SOFC control development is needed for other CVs such as compressor surge and turbine inlet temperature. In this study the authors assume that a lumped SOFC temperature is an acceptable controlled variable for minimizing SOFC thermal stresses.

Mueller presented the design, simulation and control of a gas-turbine solid oxide fuel cell model intended for use as a 100 MW-class coal syngas system [53]. The paper outlines key operating requirements for SOFCs: maintaining sufficient fuel and oxygen to prevent starvation - fuel and oxidant utilization limits are given as 95% and 35%, respectively; satisfactory fuel purity with little to no corrosive compounds or catalytic poisons; sufficiently high fuel cell temperatures to maintain ionic conductivity; low thermal stresses; and a reasonable fuel cell voltage to avoid degradation by high local heat production. Addressing these objectives, a decentralized controller comprised of PI control loops is implemented with the following input-output pairs: current-combustor temperature, fuel flow-power with a current governor, heat exchanger bypass-cathode inlet temperature, blow and bypass valve-stack temperature, and air bleed-compressor surge. The authors note that the controlled variables have multivariable interactions, such as the effect of depleted fuel, air flow, and fuel flow affect combustor temperature. Closed-loop simulations test the decentralized control performance through injection of concurrent load setpoint, ambient temperature, and hydrogen concentration disturbances. The power demand is satisfied with negligible tracking error. The fuel cell temperature is maintained within 2 K from nominal; the combustor temperature is maintained approximately between 1200 and 1300 K. The surge margin is maintained above approximately 0.1.

2.3.3 Model-Based Control

Urata proposed a planar SOFC temperature control for load-following operation [37]. The controller objective is to minimize cell temperature variation along the cell length from the nominal temperature curve for both co-flow and counter-flow planar SOFC. The average current density is varied manually from 0.05 to 0.3 A cm^{-2} to simulate load-following; however, the average current density cannot be used solely as the MV for load-following since the cell temperature distribution varies as it is changed. To address temperature control, the controller solves for the optimal value of air utilization and inlet gas (fuel and air) temperatures by minimizing temperature variation using a root-mean square objective function. The operating pressure, fuel recirculation, and fuel utilization are fixed at 0.1 MPa, 50% and 85% respectively. Air flow rate is used as the physical manipulated variable to match the optimal air utilization, and the fuel flow rate is not varied since the authors suggest that it has a weak relationship with temperature distribution. Urata developed a physics-based, two-dimensional, single channel model for a planar SOFC to perform steady-state simulations. The optimizer performs simulation runs of the SOFC model to solve for a one-dimensional channel temperature distribution as a function of air utilization and inlet gas temperatures. The controller is shown to control successfully the co-flow and counter-flow temperature variation within 10.3 K and 8.5 K respectively for the range of average current densities. Unanswered issues by Urata are as follows: what computational time is used, whether the control was applied on a plant model matching the control model or whether mismatch is included, how robust the control strategy is to disturbances, and how accurately a single channel model predicts temperatures for a planar SOFC with two-dimensional temperature variation.

Sun and El-Farra presented a model-based optimal feedback regulatory controller for controlling a distributed energy resource (DER) using a central controller over a bandwidth-constrained communication network utilized by multiple DERs [72]. The control objective is to regulate power output while minimizing network communication between the central controller and DER; this is intended to reduce network utilization and add robustness to communication disruptions. As the example DER in this study, the SOFC is modeled as a lumped system with dynamic species and energy balances. The configuration assumes that a supervisory controller provides optimal set-points to the feedback controller. The central feedback controller contains a linear state-space dynamic model of the SOFC with four states comprised of the delta of hydrogen, oxygen, and steam mole fraction and cell temperatures from nominal; the inlet molar flow rate of hydrogen is the manipulated variable. The controller with dynamic model permits discrete-time measurements from the SOFC to reduce network communication; the control law is linear as shown in the following: $u(t) = \; K\,x(t)$. The authors admit a limitation is the absence of manipulated variable constraints; the fuel flow rate is unbounded. They propose limiting the operating region to an invariant subset of a region that satisfies constraints. Model predictive control (MPC) is not chosen for this study due to the inherent difficulty in stability and performance analysis versus the chosen approach; however, MPC provides the same ability for discrete-time control with additional advantages being explicit constraints on MVs and CVs. Controller simulations are performed for both full-state feedback and output feedback, and robustness to an impulse disturbance in air flow rate is considered. Results present dynamic response of temperature and power versus their setpoint; the results indicate that a measurement sample rate of 1 per 5 s provides stable control for all cases and is a significant improvement of a 12 s sample delay.

Jurado applied a Hammerstein model predictive control (MPC) algorithm to a lumped, single-cell SOFC model for performing load-following and regulating the voltage dynamics to a nominal value [39]. The SOFC model assumes no pressure drop, no radiation in the energy balance, and a polynomial expression for specific heat to calculate enthalpies. The Hammerstein control model is comprised of a static nonlinear Takagi-Sugeno fuzzy submodel followed by a dynamic linear submodel; the combined model results in a nonlinear autoregressive moving average with exogeneous input (NARMAX) model as shown in Equation 2.6:

$$\hat{y}(k) = \sum_{i=1}^{n_a} A_i\, y(k-i) + \sum_{i=1}^{n_b} B_i\, f\left(u(k-i-n_d)\right). \tag{2.6}$$

Model predictive control has been shown in many applications to provide optimal control while maintaining constraints on the manipulated and controlled variables. An optimization occurs at each control step to provide optimal inputs. The optimization may be either explicit for a quadratic objective, linear model, and no constraints; otherwise, the routine is iterative. Jurado's controller uses quadratic programming with linear internal model control and transforms the optimal decision variables through an inverted fuzzy model to calculate the SOFC decision variables; this technique reduces the computational load since nonlinear programming and linearization are avoided. The objective function is comprised of two quadratic terms: a controlled variable error penalty and a move suppression term; Jurado mentions using a modified setpoint. The fuzzy model contains three antecedents, current, fuel flow, and temperature and one output, fuel cell voltage. Air flow is held constant. Jurado compares a linear MPC algorithm to the Hammerstein model and finds that the nonlinear model regulates voltage with a lower overshoot and has a smaller integrated time-weighted absolute error (ITAE) than the linear MPC, 352.6 to 1501.3.

Huo developed a set of two SISO control loops to perform load-following while regulating fuel utilization and voltage at their nominal values [35]. Voltage regulatory control is satisfied by a Hammerstein model comprised of a nonlinear static submodel represented by a radial basis function neural network (RBFNN) and a linear dynamic submodel approximated with an autoregressive with exogenous input (ARX) model. RBF are an advantageous neural network due to accurate approximation and faster learning versus many other neural network algorithms. Huo's SOFC model includes a fuel processing unit which reforms methane to hydrogen and is modeled as a first-order transfer function; the remainder of the fuel cell model is composed of first-order functions and the Nernst equation, i.e., the model is a lumped approximation. Load-following is achieved by adjusting the stack current. The voltage control Hammerstein model predicts output voltage as a function of natural gas input flow, oxygen flow, operating temperature, and stack current; a reference trajectory provides a modified setpoint to the controller as a linear function of the difference between terminal voltage and voltage setpoint. The constrained optimization problem is composed of a quadratic objective function, a function of errors and move suppression factors, and upper and lower limit constraints on the natural gas fuel flow. The Hammerstein model provides an accurate match of voltage dynamics. In closed-loop control simulations, a jump discontinuity in voltage occurs simultaneously with a step-change in current, and the controller moves the voltage to a slight overshoot, in comparison to the jump, below the setpoint before a smooth transition to the setpoint. Comparison with a proportional-integral (PI) controller indicates that PI control also provides zero-error voltage regulation; however, the PI control has greater oscillations. These may be mitigated with tuning but also less robust than a nonlinear model at various operating conditions. The resulting ITAE for the Hammerstein controller is approximately ten-percent lower than the PI controller.

In 2009, Mueller and Junker proposed a multi-input multi-output (MIMO) linear quadratic regulator (LQR) controller for performing load-following on a GT-SOFC bottoming power system while maintaining constraints and rejecting disturbances; the power generation unit produces 250 kW with 85% of power provided by the SOFC [52]. Mueller states that a centralized MIMO controller is expected to provide benefits based on relative-gain array (RGA) analysis that indicates coupling at time scales greater than 1 s; tight operating requirements and interactions make GT-SOFC control challenging. The LQR control objective is to minimize output variance with minimal controller variation, similar to typical multivariable model-predictive control formulations absent explicit constraints. Manipulated variables are fuel cell current, gas turbine power, anode fuel flow, and combustor fuel flow. Controlled variables (CVs) are chosen as power, fuel cell temperature, combustor temperature, fuel cell voltage, and gas turbine shaft speed. The temperatures have set-points of 1000 K and 1140 K while the latter two CVs must be held within a safe range; progressive tracking weights are used to weight importance of CV set-point tracking. This LQR formulation uses a linear time-invariant (LTI) state-space model produced by linearizing the nonlinear plant model and model reduction of states from 70 to 27. The quadratic control objective is shown in Equation 2.7:

$$J = \int_0^\infty \left(y^T Q y + u^T R u\right) dt. \tag{2.7}$$

Integral control action is applied to the power variable. The LQR controller is compared to a decentralized controller comprised of the following input-output pairs: current-power, air flow-stack temperature, combustor fuel flow-combustor temperature, and anode fuel flow-voltage control. Results indicate that the centralized controller minimizes variance of the voltage and fuel cell temperature while providing faster load-following, 20 s vs. 50 s settling time; the controller performs load-following subject to a daily ambient temperature fluctuation of 40°C and a five-percent methane concentration step-decrease. While the fuel cell temperature variation is mitigated by the controller, the mean temperature demonstrates an upward drift that is not explained by the authors.

In 2010, Fardadi, Mueller and Jabbari present a MISO H-infinity controller for minimizing one-dimensional spatial temperature variation in the flow direction of a planar SOFC [28]. The authors note that a major issue restricting SOFC load-following capability is an increase in thermal stresses consequently increasing the probability of degradation; however, power, fuel utilization, and combustor temperature control have received greater attention in published literature. The MISO temperature controller may be decoupled per the authors from these other control objectives due to the sizable thermal time constant. Manipulated variables are chosen as air flow rate and air inlet temperature; the former may be controlled with variable speed compressors, blowers, or inlet guide vanes while the latter is controlled by air recuperator bypass valves. The temperatures at five nodes in the flow direction are chosen as controlled variables; these temperatures are calculated as a function of three measurements. The control model is a standard linear model with deviation variables as states; it is reduced from 60 to 11 states per Hankel singular values. The authors use a H-infinity, or L-2 gain, controller that minimizes an estimate for bounding the output signal energy with respect to the disturbance signal, gamma, as shown in Equation 2.8:

$$\int \delta z^T \delta z \, dt \; = \; \gamma^2 \int \delta w^T \delta w \, dt. \tag{2.8}$$

Disturbances injected during the control simulation are nitrogen dilution in fuel, anode inlet temperature, and fuel cell voltage; the voltage is ramped from 0.75 to 0.82 V and later from 0.75 to 0.6 V.

Open-loop simulations illustrate how the cell temperatures will increase by 50-150 K following a voltage decrease (power increase) and will decrease by 20-50 K for increasing voltage. Closed-loop H-infinity control reduces the maximum temperature deviation from nominal under the same voltage conditions to 6 K. The authors do not directly control voltage but state that the current-combustor temperature controller provides sufficient indirect voltage control. The voltage decreases from approximately 0.85 to 0.75 V following a step-increase in load from 60 to 170 MW at 2 MW/s. For the planar cell, an increased air flow decreases the average temperature, and an air temperature increase mitigates spatial temperature variation - the voltage decrease causes the temperature profile to become more convex.

Murshed, et. al., developed linear and nonlinear MPC controllers for a planar SOFC system based upon zero-dimensional and one-dimensional models [54]. The system includes heat exchangers, a burner, and a reformer. The CV objectives are voltage tracking and a maximum constraint on the lumped cell temperature; as a 1D model, thermal gradients and local temperatures are not considered in this work. Fuel, air, and steam flow rates are the MVs. A step change in current serves as the load change and is a disturbance. The linear MPC demonstrated load following for step changes near 10% of nominal load with sufficiently long prediction horizons (100 s). The authors demonstrated improved load-following capability with nonlinear model prediction. Primary differences between this work and the present work is the use of a 1D fuel cell model and the absence of proven critical lifetime variables such as steam-carbon ratio and thermal gradients.

Bhattacharyya and Rengaswamy present a nonlinear MPC controller for tracking power and fuel utilization with a single-cell tubular SOFC [14]. The authors consider control in the seconds time scale and use a single cell, isothermal plant model that does not consider the affect of temperature drift over minutes or hours; the model is validated based on industrial data. SISO and MIMO models are identified as autoregressive with exogeneous input (ARX) and nonlinear additive autoregressive with exogeneous input (NAARX). For the MIMO controller, the MVs are voltage and hydrogen flow to track the two CVs. The SISO controller performs similarly to the reference PID control; however, the MIMO controller avoids overshoots in power and Uf that occur with multiloop PID control. Key differences with Bhattacharyya's work and the present work are the time scale, single cell vs. stack model, fewer CVs and absence of CVs that are constrained but not tracked, use of hydrogen as feed fuel, and potentially the absence of active MV constraints. An approach should demonstrate long-term SOFC control subject to MV and CV constraints and identify constraints that are critical for lifetime to be comparable to the present work.

2.3.4 Summary

The various SOFC control studies all recognize the need to provide load-following capabilities combined with robust cell lifetime and durability control for various failure modes. Failure modes include but are not exclusive to excessive thermal stress, thermal fatigue, catalyst poisoning, coking, reversal of cell potential, redox reactions within the EEA layer material, and catalyst corrosion. A comparison of various control approaches provides better informed perspective on the state of existing control with regards to control objectives, structure, optimization methodology, and model types. A full summary of the classical and model-based controllers reviewed in this chapter were shown in Table 2.2.

The literature review indicates that researchers often seek to mitigate thermal stresses and thermal fatigue using indirectly related controlled variables, whether control of voltage, lumped cell temperatures, and outlet gas temperatures; a couple labs have sought to model a one-dimensional planar temperature distribution and minimize the variation. In addition, a majority of previous control research has applied single output control methods. These studies have provided valuable knowledge of theoretical fuel cell operation, and it is clear that opportunities remain to investigate more advanced thermal modeling and multivariable control methods. An ultimate goal of more recent studies including this dissertation is to illustrate the potential for advanced control to improve solid oxide fuel cell performance and operational flexibility.

2.4 Reliability

Fischer, Seume, et. al., investigated thermal contributions to mechanical stress within the SOFC electrode-electrolyte assembly (EEA), and a primary conclusion from his work is that advanced control is warranted to prevent excursions into operating regimes disadvantageous for reliability [30]. Characterizing the stress distribution is important for assessing failure and degradation. Fischer developed a 2D finite element mechanical model for a tubular SOFC linked to a 2D thermo-electrochemical model and investigated the effect of differing operating conditions with and without internal methane reformation. Thermal stress may result from fabrication conditions, thermal cycling, high temperature gradients, and property mismatch between adjacent layers; thermally induced stress leading to micro-cracking is a primary cause of mechanical failure and degradation. A key assumption of the analysis by Fischer is that the SOFC EEA layers are sintered together at a uniform temperature of 1250°C; the assumption of sintering at uniform temperature is one made by multiple authors referenced by Fischer. Therefore, this temperature becomes the zero-stress reference temperature. The strain and crack probability calculations are critically dependent on the zero-stress reference temperature.

Fischer's analysis indicates that the minimum cell temperature is the primary contributor to thermally-induced tensile stresses within the EEA. Tensile stresses rising from a cell cold spot at 1173 K are one magnitude larger than the next largest contributor, maximum negative radial thermal gradients of -5000 K/m. Positive radial thermal gradients and axial gradients have a negligible effect on tensile stresses in the tubular SOFC; note that this conclusion only holds true for the tubular geometry, excluding the planar SOFC. One may question whether room-temperature conditions would be the likely worst stress case for the tubular SOFC. While it is not expected that the yield stress is exceeded at room temperature, the mode of failure below yield stress should be due to cycling between low stress, high temperature states to high stress, low temperature states.

Nakajo, et. al., likewise concluded that raising the minimum cell temperature and average cell temperature increases fuel cell probability of survival [55]; they also find that minimizing radial thermal gradients placing the anode and electrolyte in tension is critical for cell lifetime. The maximum radial thermal gradients occur in the fuel/air inlet where steam reformation occurs. This work is specific to the tubular SOFC geometry with a yttria-stabilized zirconia electrolyte.

Several key conclusions may be drawn from the stress analysis for modeling and control:

- Control strategies must focus on the proven main contributors to thermo-mechanical tensile stress. In the case of tubular SOFC, these are minimum absolute temperatures and maximum negative radial thermal gradients.
- Modeling half-reactions separately is not necessary for a sufficiently accurate characterization of stress; however, a radially discretized thermal model is necessary for stress prediction and management.

- Cycling SOFC startups should be avoided due to excursions into low temperature regimes. A more robust strategy for load-following would be maintaining all SOFC cells online and tracking loads dynamically.

Chapter 3

Solid Oxide Fuel Cell System Modeling

3.1 SOFC System Model Overview

The standard tubular solid oxide fuel cell system as based on the Siemens Power Generation unit contains an SOFC, ejector, and prereformer as shown in Figure 3.1. Full or partial load operation of the SOFC requires 1) a constant fuel input to the ejector, which may consist of fuels including natural gas, ethanol, and hydrogen, and must be desulfurized; 2) recirculation of steam from the SOFC outlet through the ejector to the SOFC inlet; 3)

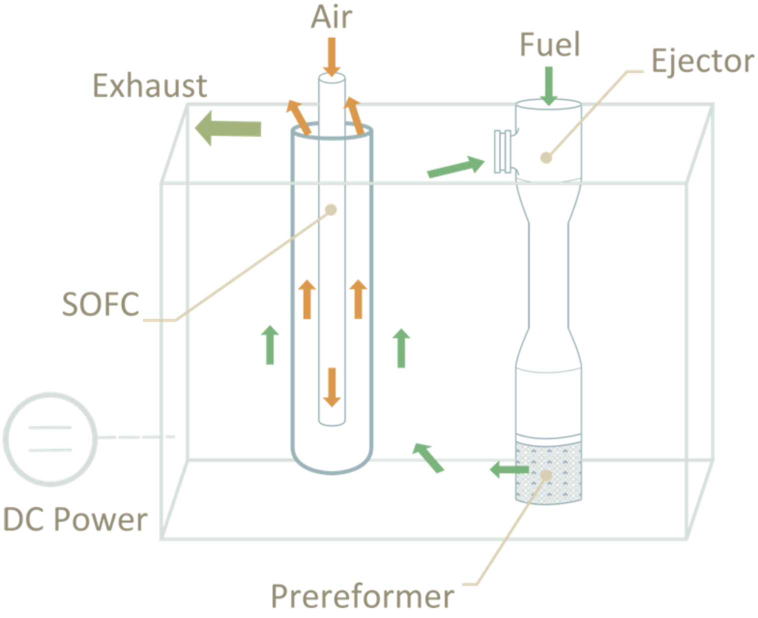

Figure 3.1: Internal fuel and air flow within the SOFC system

preheated air and fuel; and 4) an external electrical circuit. Typical systems will also have a combustor to consume effluent methane and hydrogen.

The SOFC system-level model presented here comprises three submodels with transport delays between the submodels. A tubular SOFC submodel, ejector submodel, and prereformer submodel are connected within MATLAB/Simulink to form the SOFC system-level model as shown in Figure 3.2; submodels are solved sequentially at each time step.

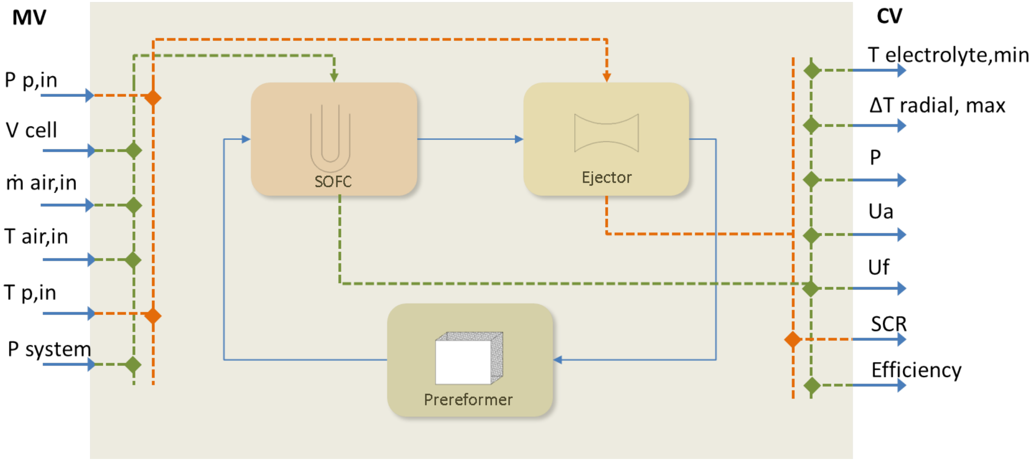

Figure 3.2: SOFC system schematic with connections between submodels

Internal system model variables exchanged between the submodels are gas transport states of temperature and molar flow for the SOFC and temperature, mass flow, and mole concentration for the ejector and prereformer. A gas transport delay block is applied to inlet variables of all submodels.

The SOFC system model presented here differs from many models reviewed in Chapter 2 in several key aspects. The SOFC submodel, as a two-dimensional, distributed parameter model, provides resolution in both axial and radial directions. The two-dimensional model provides more accurate dynamics and input-output relationships than a lumped model for the tubular SOFC; both of which are necessary to capture local causes of thermal stress. The system model contains all prime mover elements of the standard Siemens Power Generation tubular SOFC system, fuel cell, ejector, and prereformer, to ensure that the manipulated variables (MVs) can be changed with standard equipment. The objective of the present system model is to investigate open-loop and closed-loop dynamics of SOFC fuel cell reliability in the presence of load-following and fuel quality disturbances. As such, it does not contain some features found in lumped SOFC models in literature, such as electrical balance of plant (BOP) or gas turbines.

The external manipulated variables chosen for the SOFC system are inlet fuel pressure and temperature, cell voltage, inlet air mass flow and temperature, and system pressure. The inlet fuel pressure and temperature are connected to the ejector submodel, and all other MVs are connected to the fuel cell submodel. The manipulated variables may be changed by balance of plant equipment as shown in Figure 3.3. The fuel and air temperatures may be changed with recuperators and bypass control valves. Fuel pressure, air mass flow, and system pressure may be changed using two variable speed compressors. Cell voltage may be changed via the electrical regulatory controls.

Controlled variables (CVs) for the system are the power, minimum cell temperature, maximum radial thermal gradient, air utilization, fuel utilization, steam-to-carbon ratio (SCR), and efficiency. The SCR is calculated from the ejector submodel, and all other CVs are calculated from the fuel cell model.

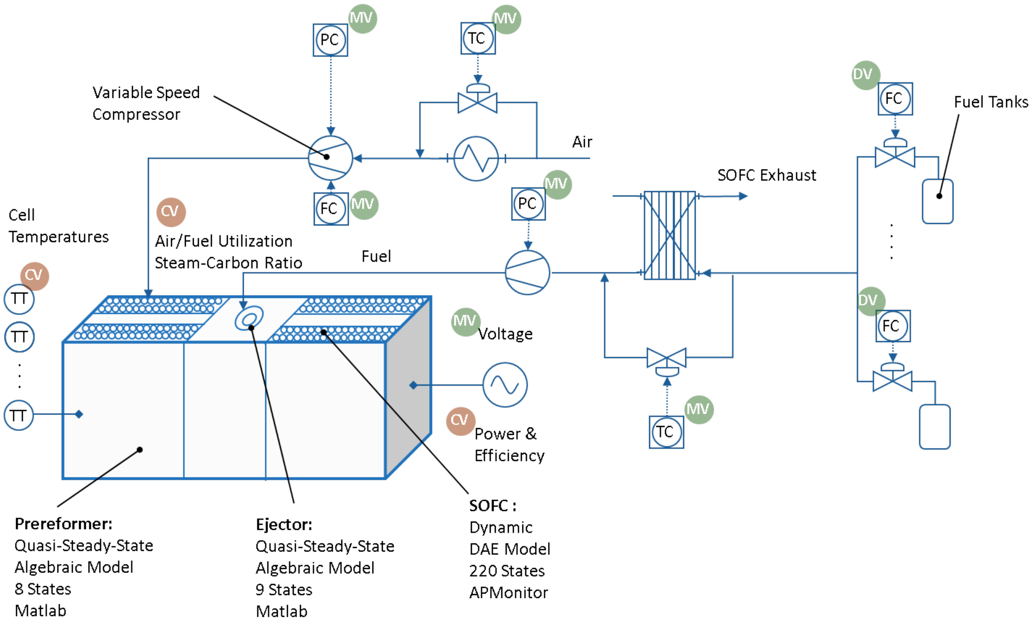

Figure 3.3: The SOFC system process and instrumentation diagram

These CVs are chosen to satisfy performance criteria of load-following and efficiency and lifetime criteria. In this study, power and minimum cell temperature are chosen as tracked CVs. The operation range of all operability CVs - temperatures, utilizations, and SCR - are also limited with soft constraints. Justification for choosing these CVs is provided in more detail within Chapter 2, Background. Since the number of CVs is greater than MVs, including all of the CVs will result in a *thin plant* case regardless of whether the controller structure is centralized or decentralized. If SOFC system operation is sufficiently far from at least one CV constraint in this case, the controller will effectively act like the *square* or *fat plant* case [62].

The SOFC submodel is modeled dynamically while the ejector and prereformer submodels are modeled as quasi-steady-state (QSS) since only gas properties are considered in these latter two submodels. In the same manner gas transport in the SOFC submodel is modeled as QSS. The three transport delay models account for gas phase transport delays. The transport delay time is calculated by evaluating the ratio of volume to volumetric flow rate:

$$\tau = \frac{V}{Q} = \frac{\rho V}{R T \dot{m}} \tag{3.1}$$

with volume, V, pressure, p, universal gas constant, R [J/$(kg\,K)$], temperature, T, and mass flow, $\dot{m}$, calculated as a function of the upstream flow. The delayed states are upstream temperature and upstream molar flow for the SOFC submodel; the delayed states for the ejector and prereformer models are upstream temperature, mass flow rate, and molar concentrations. The transport delays are implemented in Simulink using the variable time delay block.

The dynamic changes modeled for the SOFC system are electrical load setpoint changes and inlet fuel concentration disturbance changes. The electrical load setpoint is determined by the electrical grid demand; the variance of electrical load will depend on the SOFC system configuration with energy storage and the grid. As the SOFC fuel type is commonly natural gas, the fuel quality can be expected to vary in methane concentration, particularly in unconventional applications such as landfills or biofuel plants. The mean concentration of CH_4 in unprocessed natural gas is ninety-five-percent [42] though this figure may vary significantly, and the remainder of fuel may contain CO, CO_2, N_2, and vapor H_2O. Natural gas is commonly known to contain hydrogen sulfide, and this impurity is expected to be removed by upstream processing to negligible concentrations. Current and voltage disturbances are expected to be handled by an external DC converter controller and are thus not considered in this model. Ambient temperature would be a disturbance if the air or fuel temperatures were not considered as MVs.

3.2 Tubular SOFC Submodel

3.2.1 Modeling Approach and Assumptions

The solid oxide fuel cell models may have differing steady-state assumptions, discretization, and constants to suit the model purpose. Common modeling objectives are fuel cell design, system balance of plant design, steady-state and dynamic operational knowledge, and control studies. The dynamic model as developed here has three primary objectives: (1) investigating the dynamic response of important controlled variables subject to disturbances; (2) testing advanced control strategies; and (3) optimizing the system size and inlet variables. In consideration of these objectives, the computational model is designed as follows:

- A two-dimensional, distributed parameter model calculates fuel cell variables spatially in the axial and radial directions. Symmetry is assumed in the circumferential direction.
- A finite-volume approach ensures conservation of energy between adjacent nodes.
- The single cell modeled exists within the stack center and assumes no net heat exchange between cells, end-effects, or heat exchange with the environment. The single cell model is representative of all cells in the stack.
- The air and fuel chambers may contain up to seven chemical species: H_2, vapor H_2O, O_2, N_2, CH_4, CO, and CO_2.

- Temperature-critical properties are modeled as a function of temperature: the air and fuel specific heat capacities, thermal resistance of each electrode-electrolyte assembly (EEA) layer, reaction constants, Nernst voltage, and polarization losses.

- Concentric tube radiation occurs between the air supply tube and cathode surface.

- The steam reformation endothermic heat generation term is a surface reaction on the outer diameter of the anode, and the electrochemical exothermic heat generation term is a volumetric reaction within the electrolyte.

- The fuel and air chamber has uniform pressure with the pressure calculated based upon Darcy's law. The use of Darcy's law is satisfactory for compressible flow given a pressure drop less than ten-percent.

- Current flows in the circumferential direction but not longitudinal due to equipotential voltage. The electrochemical reaction considers hydrogen as the fuel reactant; the rate of carbon monoxide oxidation is much slower.

- The dynamic model time update is sufficiently long, one second, such that the quasi-steady-state assumption for electrical and gas transport dynamics is valid.

A cross-section demonstrating the two-dimensional model is shown in Figure 3.4 with a single finite volume having an axial length of Δx. Each

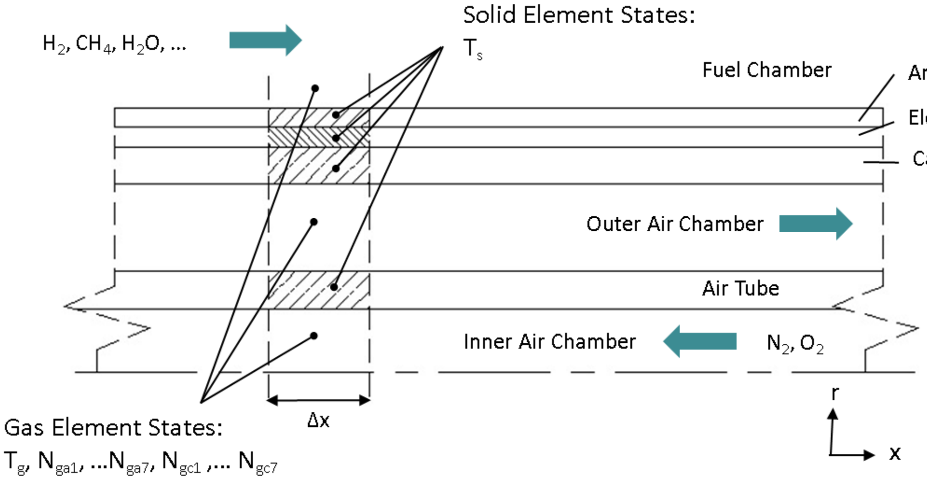

Figure 3.4: The SOFC cross-section illustrates the seven finite volumes in the radial direction (not to scale)

unique fuel cell layer is modeled with one finite volume in the radial direction; the fuel cell layers are listed as follows: the supply tube air chamber, supply tube solid, cathode air chamber, cathode solid, electrolyte solid, anode solid, and anode air chamber. Each radial layer is discretized in the axial direction with forty volumes for the steady-state model and ten volumes in the dynamic model.

Use of calibration factors for model fitting is limited to variables not provided by the literature that was used for validation: thermal contact resistance, fuel flow area between cells, and heat transfer coefficient multipliers. A thermal contact resistance factor should exist in the experimental fuel cell due to account for imperfect interfaces between EEA layers, material property variation, and the existence of microcracking; the factor is included as a fraction of the overall conductive resistance. The outer diameter of the anode chamber has not been specified in commonly cited literature for the Siemens

Power Generation SOFC. In addition, this gap is not constant around the SOFC circumference. The gap is chosen conservatively on the same order as the cell radius. A constant heat transfer coefficient is a simplifying assumption, and multipliers are applied to the coefficient calculated from the Nusselt number. These multipliers do not exceed a factor of four.

3.2.2 Input and Output Variables

The solid oxide fuel cell submodel requires inputs from the reformer submodel within the fuel cell system and the external MVs. The SOFC external MVs are mass flow and temperature of inlet air, system pressure, and the equipotential cell voltage. The voltage can be changed practically by adjusting external resistance via the power conversion equipment. Output variables from the fuel cell are the outlet gas temperature and molar concentrations for both fuel and air streams, minimum electrolyte temperature, electrolyte temperature distribution, maximum EEA radial thermal gradient, current, power, efficiency, fuel utilization, and air utilization. A description of all input and output variables along with their source or sink is presented in Table 3.1.

3.2.3 Material Balance

The conservation of species is accounted by performing a quasi-steady-state (QSS) mole-basis material balance for each gas volume in the axial direction. The mole-basis form ensures molar conservation whereas mole or mass fraction balances do not always provide this guarantee. The QSS assumption is applied for gas transport in the axial direction assuming the gas dynamics settling time for step changes is less than the time-step for dynamic model up-

Table 3.1: SOFC Submodel Input and Output Variables

Input

Variable	Description	Units	Source
$\dot{m}_{air,in}$	inlet air mass flow	kg/s	external MV
$T_{air,in}$	inlet air mass temperature	K	external MV
$T_{fuel,in}$	inlet fuel mass temperature	K	prereformer
P_{system}	system pressure	bar	external MV
V_{cell}	cell voltage	V	external MV
$\dot{m}_{fuel,in}$	inlet fuel mass flow	kg/s	prereformer
X_{fuel,in,H_2-CO_2}	inlet fuel H_2-CO_2 concentration	n/n%/100	prereformer

Output

Variable	Description	Units	Sink
P	power	W	external CV
η_{LHV}	efficiency	%	external CV
i	current	A	
U_a	air utilization ratio	%/100	external CV
U_f	fuel utilization ratio	%/100	external CV
$T_{electrolyte,min}$	minimum electrolyte temperature	K	external CV
$T_{electrolyte,1-10}$	volume electrolyte temperatures	K	
$\Delta T_{radial,max}$	maximum radial temperature gradient	K/m	external CV
$T_{air,out}$	outlet air mass temperature	K	
$T_{fuel,out}$	outlet fuel mass temperature	K	ejector
$X_{air,out,O_2\,\&\,N_2}$	outlet air O_2 & N_2 concentration	n/n%/100	prereformer
X_{fuel,out,H_2-CO_2}	outlet fuel H_2-CO_2 concentration	n/n%/100	prereformer

dates. The assumption of QSS applies rather than steady-state since the QSS variables are updated over time as driven by the solid temperature dynamics. Open-loop tubular SOFC gas dynamic response settles within less than 1 s for step changes of 0.1-0.2 V and 10-14% of fuel flow rate at the considered nominal value [13]. These step-changes are of similar maximum magnitude as those considered in the dynamic simulations considered here. The species balance is calculated according to Equation 3.2 as follows:

$$\dot{N}_{i,out} = \dot{N}_{i,in} + \sum_{j=1}^{3} v_i \, r_j \quad [mol \, s^{-1}] \tag{3.2}$$

where $\dot{N}_i$ is the species molar flow rate in mole/s, v_i is the stoichiometric coefficient, r_j is the reaction rate in mole/s, i refers to the species, and j refers to the reaction. The species considered are H_2, H_2O, O_2, N_2, CH_4, CO, and CO_2. The three reaction terms for the fuel chamber are steam reformation, water-gas shift, and electrochemical reactions. Air within the outer air chamber is only affected by the electrochemical reaction rate, and air within the inner air chamber undergoes no reactions.

3.2.4 Reformation and Shift Reactions

The reaction expressions for methane reformation and water-gas shift reactions are shown respectively in Equation 3.3.

$$\begin{aligned} CH_4 + H_2O \quad &\overset{r_{CH_4}}{\longleftrightarrow} \quad CO + 3\,H_2 \\ CO + H_2O \quad &\overset{r_{shift}}{\longleftrightarrow} \quad CO_2 + H_2 \end{aligned} \tag{3.3}$$

Due to SOFC high-temperature operation in excess of 600°C, fuel may be reformed directly along the anode surface. A fuel mixture primarily consisting of methane, hydrogen, and steam is considered as the fuel at the anode inlet in a similar manner as Campanari and Aguiar [3, 16]. Tubular reaction models commonly use an area-based methane reformation model [17, 71]. The model chosen here is based upon the empirical equation proposed by Achenbach and Riensche [2] which is first-order in methane partial pressure for a 80 wt.% ZrO_2 and 20 wt.% Ni cermet[1]; the reaction expression is shown as follows in Equation 3.4:

$$r_{CH_4} = A \exp\left(-\frac{E_a}{RT}\right) p_{CH_4} \quad [mol\, m^{-1}\, s^{-1}], \tag{3.4}$$

with the frequency factor A, activation energy E_a, gas constant R, anode temperature T, and methane partial pressure p_{CH_4}. The frequency factor and activation energy were found empirically by the same authors as follows in Equation 3.5:

$$\begin{aligned} A &= 4,274 \;\; [\tfrac{mol}{m^2\, bar\, s}] \\ E_a &= 82 \;\; [\tfrac{kJ}{mol}]. \end{aligned} \tag{3.5}$$

Belyaev likewise found the reaction rate to be first-order in methane and zero order in water for a Ni-(5 wt.%) ZrO2-(2 wt.%) CeO_2 anode [12]. A more complete discussion of proposed methane reaction mechanisms is discussed in the literature review.

The water-gas shift reaction is commonly considered to be at equilibrium since it reaches completion very quickly at high temperatures greater than 600°C at which catalysts are typically not used. The expression for the shift reaction is shown as follows in Equation 3.6:

$$r_{shift} = k \left(X_{H_2O}\, X_{CO} - \frac{X_{H_2}\, X_{CO_2}}{K_{eq}}\right) \quad [mol\, m^{-3}\, s^{-1}] \tag{3.6}$$

---

[1] a composite material containing ceramic and metallic materials

with the mole fractions denoted by X, pre-exponential factor k, and equilibrium constant K_{eq}. The pre-exponential factor may be chosen heuristically to ensure the shift reaction proceeds to completion. The equilibrium constant is calculated via an empirical equation as follows in Equation 3.7:

$$\begin{aligned} K_{eq} &= \exp\left(-0.2935\,\zeta^3 + 0.635\,\zeta^2 + 4.1788\,\zeta + 0.3169\right) \\ \zeta &= \tfrac{1000}{T} - 1. \end{aligned} \tag{3.7}$$

where the temperature T is in Kelvin[36].

3.2.5 Electrochemical Equations

The primary electrochemical reaction within the SOFC is hydrogen oxidation and is composed of two half-reactions occurring at the anode and cathode respectively as shown in Equation 3.8. These two equations are followed by the combined redox reaction.

$$\begin{aligned} H_2 + O^{-2} &\xrightarrow{r_{anode}} H_2O + 2\,e^- \\ O_2 + 4e^- &\xrightarrow{r_{cathode}} 2\,O^{-2} \\ 2\,H_2 + O_2 &\xrightarrow{r_{redox}} 2\,H_2O \end{aligned} \tag{3.8}$$

The electrochemical reaction expressions represent how oxides, such as yttria-stabilized zirconia, are pure ionic conductors allowing only the oxygen anion to permeate through the electrolyte. Oxidation of carbon monoxide to carbon dioxide is not considered here as in most literature due to dominance by the fast water-gas shift reaction. The electrochemical hydrogen oxidation reaction is central to calculating species molar concentrations, exothermic heat release, and current profiles along the fuel cell length.

The difference in thermodynamic potentials between the anodic and cathodic reactions determines the open-circuit voltage. The open-circuit voltage is calculated using the Nernst equation as a combination of 1)the open-circuit voltage at standard temperature and pressure and unity activity as a reference voltage and 2)a term dependent upon local reactant-product partial pressures and cell temperature as shown in Equation 3.9:

$$\begin{aligned} V_{oc} &= V_{H_2}^{0} + \frac{RT}{2F} \ln\left(\frac{p_{H2}\, p_{O_2}^{0.5}}{p_{H_2O}}\right) \\ V_{H_2}^{0} &= -\frac{\Delta G_0}{2F} + \frac{\Delta S_0}{2F} (T - 298) \end{aligned} \tag{3.9}$$

with the open-circuit voltage V_{oc}, standard voltage $V_{H_2^0}$, universal gas constant R, Faraday's constant F, partial pressures p_i in bar, and temperature T in Kelvin. Values for constants within the Nernst equation may be readily found in literature [57].

The actual cell voltage V_{cell} is calculated as the difference between open-circuit voltage and polarization losses, or overpotential, as shown in Equation 3.10:

$$V_{cell} = V_{oc} - \eta_{act} - \eta_{conc} - \eta_{ohm}, \tag{3.10}$$

with activation losses η_{act}, concentration losses η_{conc}, and ohmic losses η_{ohm}. The concentration, or diffusion, overpotential is neglected in some literature since it is orders of magnitude below the activation and ohmic losses in the primary operating range; other literature have set the loss equal to 50 mV [69]. These losses are inherent in all fuel cells and are a function of fuel and oxidizer properties, cell design, and materials. The overall activation and concentration losses are a combination of activation and concentration losses at the anode and cathode. All losses are considered in this work. Whereas the losses and open-circuit voltage are locally dependent, the cell voltage is commonly considered to be constant across the fuel cell length; this is commonly known as the equipotential assumption.

Ohmic overpotential is due to ionic and electronic conductive resistance within the fuel cell circuit. The current-collector, anode, electrolyte, and cathode contribute to conductive resistance, and ohmic loss is calculated via Ohm's law as shown in Equation 3.5:

$$\eta_{ohm} = \; I\, R_{ohm}, \tag{3.11}$$

with finite volume current I in amps and volume resistance R_{ohm} in ohms. Individual layer resistances are calculated based upon published expressions for thermal conductivity as a function of temperature for the four cell layers as shown in Table 3.2[17]. Unidirectional current flow in the radial direction within the collector and electrolyte and circumferential direction within the electrodes is considered for calculating the effective ohmic resistance; no current is considered to flow axially due to the equipotential assumption.

Activation overpotential represents the effect of electrode half-reaction kinetics. Proceeding with the electrochemical reaction requires overcoming an activation energy barrier thereby causing a voltage drop; the losses decrease as the cell temperatures increases as the reactions occurs more quickly. The activation overpotential is calculated via the Butler-Volmer relations as shown in Equation 3.12:

$$i \;=\; i_0 \left[\exp\left(\beta \, \frac{n\, F\, \eta_{act}}{R\, T} \right) \;-\; \exp\left[-\,(1-\beta)\, \frac{n\, F\, \eta_{act}}{R\, T} \right] \right] \; A/m^2, \tag{3.12}$$

with the current density i, exchange current density i_0, electronic transfer coefficient β, and the number of electrons involved in the half-reaction n [20]. For low activation overpotential conditions, the Butler-Volmer relation in Equation 3.12 may be approximated by a linear relation as shown in Equation 3.13:

$$\eta_{act} = \frac{R\,T\,i}{n\,F\,i_0}. \tag{3.13}$$

The exchange current density is calculated as a function of local partial pressures and cell temperature as shown in Equation 3.14:

$$\begin{aligned} i_{0,an} &= \gamma_{an} \left(\frac{p_{H_2}}{p_{amb}}\right) \left(\frac{p_{H_2O}}{p_{amb}}\right)^m \exp\left(-\frac{E_{act,an}}{R\,T}\right)\; A/m^2, \\ i_{0,cat} &= \gamma_{cat} \left(\frac{p_{O_2}}{p_{amb}}\right)^{0.25} \exp\left(-\frac{E_{act,cat}}{R\,T}\right)\; A/m^2, \end{aligned} \tag{3.14}$$

with the values for all constants as found in literature [17, 20].

Concentration overpotential, or diffusion overpotential, is included in the voltage polarization losses to compensate for voltage losses resulting when the reaction site concentration is lower than the bulk concentration due to diffusion mass transfer. The overall diffusion overpotential is calculated as the sum of anodic and cathodic overpotentials as shown in Equation 3.15:

$$\begin{aligned} \eta_{conc} &= \eta_{conc,an} + \eta_{conc,cat} \\ &= \frac{R\,T}{2\,F}\,\ln\left(\frac{X^b_{H_2}\,X^r_{H_2O}}{X^r_{H_2}\,X^b_{H_2O}}\right) + \frac{R\,T}{4\,F}\,\ln\left(\frac{X^b_{O_2}}{X^r_{O_2}}\right), \end{aligned} \tag{3.15}$$

with the molar fractions X for bulk b and reaction r site locations. The diffusion overpotential increases as current increases, but within the operating range less than peak SOFC power, the ohmic and activation losses are orders of magnitude greater than the concentration overpotential. Expressions for the mole fractions at reaction sites are derived by applying Fick's law over two diffusion steps in the radial direction for the anode and two steps for the cathode.

An expression for the molar flux of hydrogen is shown in Equation 3.16:

$$\begin{aligned} J_{H_2} &= -\tfrac{p_{an}\,D}{RT}\,\tfrac{dX_{H_2}}{J_{tot}} + X_{H_2}\,J_{tot} \\ J_{tot} &= J_{H_2} + J_{H_2O} = 0 \end{aligned} \tag{3.16}$$

with the molar flux of hydrogen J_{H_2} and the total molar flux J_{tot} being equal to zero since the steam flux is equal and opposite the hydrogen flux. This expression can be integrated over the two diffusion steps, from the bulk to local electrode concentration and from the local to reaction site concentration. A complete description of equations needed to calculate the concentration overpotential is given by Campanari[17].

3.2.6 Ohmic Resistance

Given the equipotential assumption, current flow within the fuel cell is contained within the circumferential and radial directions and is driven by radial potential gradients [20]. The circuit diagram is illustrated in Figure 3.5. Oxidation of the fuel at the anode-electrolyte interface provides free electrons that migrate through the external circuit and re-enter the cell at the interconnect. Reduction at the cathode creates oxygen anions which then migrate across the electrolyte oxide, completing the transport of negative charge. Note in Figure 3.5 that the arrows indicate the direction of electrical transport which is the opposite direction as current flow.

EEA layer resistances are calculated based upon published expressions for thermal conductivity as a function of temperature [17]. Table 3.2 illustrates the material and geometry data used to calculate the ohmic resistance.

The tubular SOFC cross-section is discretized circumferentially and

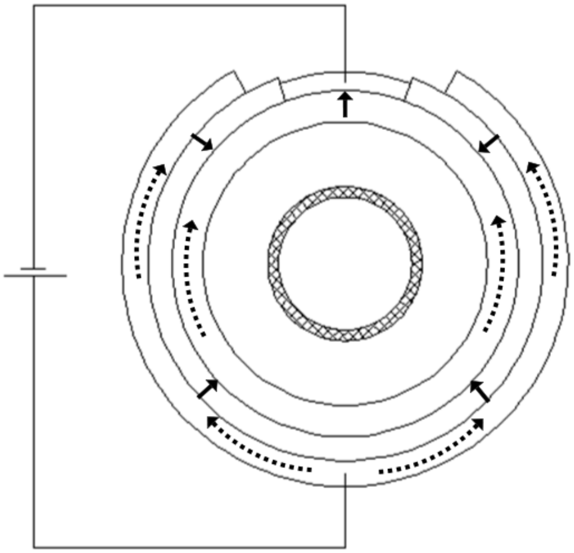

Figure 3.5: Electrical circumferential and radial transport within the tubular cell

Table 3.2: Ohmic resistivity of SOFC layers

EEA Layer	$\rho\ (\Omega\, m)$	$thk\,(m)$
Anode	$2.98\left(10^{-5}\right)\exp\left(-\frac{1392}{T_{s,a}}\right)$	$100.0\left(10^{-6}\right)$
Electrolyte	$2.94\left(10^{-5}\right)\exp\left(\frac{10350}{T_{s,e}}\right)$	$40.0\left(10^{-6}\right)$
Cathode	$8.11\left(10^{-5}\right)\exp\left(\frac{600}{T_{s,c}}\right)$	$2.2\left(10^{-3}\right)$
Interconnect	0.025	$85.0\left(10^{-6}\right)$

radially into volumes of 45° segments, and resistance for volumetric segment i may be calculated from the resistivity as shown in Equation 3.31:

$$R_i = \frac{\rho_i\,\delta_i}{A_i}, \tag{3.17}$$

with the thickness δ calculated as the length in the direction of electrical transport, and the area A is the area of electrical transport normal to the direction of transport. An expression for the total resistance per radial element is shown as R_{ohm} in the appendix. Note that R_{tc} is the thermal contact resistance tuning parameter. Since the circumferential and radial potential gradients remain in the same direction, the equivalent resistance of the two-dimensional cell circuit may be calculated from individual segment resistances with series and parallel circuits.

3.2.7 Energy Balance

Heat transfer within the tubular SOFC is closely coupled with current distribution and gas species distributions as the EEA electrical conductivities are temperature dependent. Key modes of heat transfer involve convection along the cathode, anode, and air tube, radiation between the cathode and air tube, and radial and axial thermal conduction along all layers and the air tube. The primary of mode of heat transfer to the fuel and air is convection; gas conduction along the axial direction is negligible versus convection. With the single-cell model the cell is located within the center of a bundle and is assumed to be representative of all cells; due to symmetry the interface between the cell and other cells is adiabatic. Heat transfer with the surroundings and end-effects are not considered for the single-cell model. Assumptions are chosen to represent a balance between accuracy and computational complexity for use in system-level studies and are common with other researchers.

3.2.7.1 Convection

Researchers conducting detailed steady-state analysis have found that gas flow on the anode side is within the laminar regime whereas flow on the cathode side lies within the transition region [3, 17]. Convection heat exchange is calculated as a function of the heat transfer coefficient and the temperature difference between gas and solid temperatures as shown in Equation 3.18:

$$Q_{conv,ij} = \sum_j h_j \, A_j \, (T_{s,surf,ij} - T_{g_i}) \tag{3.18}$$

with the total heat transfer to the gas denoted by $Q_{conv,ij}$, the solid surface temperature $T_{s,surf}$, and i and j refer to gas volume and solid volume respectively. Campanari used constant Nusselt numbers averaged along the axial length of the fuel cell solid-gas interfaces, and the same convention is applied here. The Nusselt number relates convective heat transfer to fluid conductive heat transfer as shown in Equation 3.19:

$$N_u = \frac{h}{L_c \, k_f}, \tag{3.19}$$

with the convection coefficient h, characteristic length of heat transfer L_c, and fluid thermal conductivity k_f. The Nusselt number chosen for the fuel chamber, outer air chamber, and inner air chamber are 4.2, 5.5, and 11 respectively.

3.2.7.2 Radiation

Due to high operating temperatures near 1000°C and significant temperature differences between cell surfaces, radiation should be considered between the cathode inner radius and air tube outer radius. No radiation from the anode outer radius is considered due to the adiabatic boundary between cells in the single-cell model. The view factor for directly opposite elements is calculated based on the relation for parallel plates with midlines connected by the perpendicular. The view factors for both radiation from the cathode to anode and vice versa are multiplied by a coefficient based upon the concentricity of cylinders relation. This relation accounts for the fraction of radiation emitted from the outer cylinder that contacts the inner cylinder. The view factor from the inner air tube is unity while the view factor from the outer cathode is 0.3. Total radiation by heat transfer is calculated using the grey body radiation equation shown in Equation 3.20:

$$Q_{rad,ij} \;=\; \varepsilon \, A_i \, F_{ij} \, \sigma \, \left(T_i^4 \, - \, T_j^4\right), \tag{3.20}$$

with the emissivity ε chosen as 0.8 in accordance with Stiller [69]. Radiation is only considered between opposing volumes; exchange between diagonal volumes is significantly less due to the high aspect ratio that results from discretizing the model into ten volumes.

3.2.7.3 Gas Energy Balance

The gas energy balance applies to the fuel chamber, the inner air chamber, and the outer air chamber. The thermal capacitance of the air and fuel is lower by 10^{-1} - 10^{-2} than the thermal capacitance of the solid, and the gas flow velocity is an order of 10^2 times the number of discrete segments which suggest the QSS is valid for the time step of interest, one second. The gas energy balances are modeled as QSS balances as shown in Equation 3.21:

$$
\begin{aligned}
&\dot{N}\,MW\,c_p\,T_g|_{i,out} \;= \\
&\qquad \dot{N}\,MW\,c_p\,T_g|_{i,in} + \sum_j h_j\,A_j\,\left(T_{s,surf_{ij}} - T_{g_i}\right) - \sum_k \Delta H_{ik}\,r_{ik}, \qquad (3.21)
\end{aligned}
$$

with the total molar flow rate of the finite volume $\dot{N}$ in mol/s, the gas temperature T_g in K, the solid surface temperature $T_{s,surf}$, the combined mixture molecular weight MW, the reaction rate r in mol/s, i as an axial index for the finite volumes, j as a radial index for the solid surfaces surrounding the chamber, and k as an index for the reactions. Fourier's law of heat conduction is applied in the radial direction to model the conductive resistance between the solid temperature located in the center of the finite volume and the surface as shown in Equation 3.22:

$$Q_{cond,ij} = \frac{k\,A}{\Delta r}\left(T_{s,surf_{ij}} - T_{s_{ij}}\right), \qquad (3.22)$$

with the core solid temperature T_s, thermal conductivity k, and half layer thickness Δr. The heat of conduction in Equation 3.22 is equal to the heat of convection in the overall energy balance, Equation 3.21, allowing the elimination of the surface temperature. The mixture molecular weight, MW, is calculated as a sum of the individual species molecular weights weighted by the mole fraction, X_i, corresponding to each species as shown in Equation 3.23:

$$
\begin{aligned}
MW &= \sum_i MW_i\,X_i \\
X_i &= \tfrac{\dot{N}_i}{\dot{N}}.
\end{aligned} \qquad (3.23)
$$

The specific heat capacities are calculated as a function of temperature using a constant pressure equation of state. A polynomial expression for the species is used in the form shown in Equation 3.24:

$$\frac{c_{p,ig}}{R} = \alpha + \beta T + \gamma T^2 + \frac{\varsigma}{T^2}, \tag{3.24}$$

with the coefficients α, β, γ and ς dependent on the species [58] and $c_{p,ig}$ and R in terms of $J\,mol^{-1}\,K^{-1}$.

3.2.7.4 Solid Energy Balance

The dynamic energy balance for the solid layers of the fuel cell, the anode, electrolyte, cathode, and air tube, are separately modeled to capture the slow thermal response having a time frame of hours. The dynamic solid layer energy balance is a function of heat and mass convection, heat conduction, and radiation. In addition, the electrolyte layer has a heat of reaction term. The generic energy balance is shown in Equation 3.25:

$$\begin{aligned}\rho\, V\, c_{p,i}\,\frac{dT_{s,i}}{dt} &= h\,A\,(T_{g_i} - T_{s,surf,i}) + k\,A\,\frac{dT_{s,i}}{dx} \\ &\quad + k\,A\,\frac{dT_{s,i}}{dr} + \varepsilon\,F_i\,\sigma\,A\,\left(T_{s,opp}^4 - T_s^4\right)|_i + \dot{Q}_{elec},\end{aligned} \tag{3.25}$$

with the electrochemical exothermic heat release, Q_{elec}, only applied to the electrolyte layer, the radiation term only applied to the cathode and air tube layers, the index for layer s, and the index for volume i. The solid energy balance is in the form of a partial differential equation and must be reduced into ordinary differential equation form for solution with the DAE solver. The spatial temperature gradient is discretized using a second-order Euler's approximation as shown in Equation 3.26:

$$\frac{dT_{s,i}}{dx} = \frac{T_{s,i+1} - 2\,T_{s,i} + T_{s,i-1}}{\Delta x}, \tag{3.26}$$

for a center volume with the sum of two differences of three temperatures. If the current volume is a boundary volume, only one difference of two temperatures is considered.

The exothermic heat release from electrochemical reactions is calculated as the difference between the potential power as the heat of reaction and the realized power produced by the cell as shown in Equation 3.27:

$$\dot{Q}_{elec} = \left(\frac{\Delta H_{f,H_2O(g)}}{n\,F} - V_{cell} \right) \cdot i, \tag{3.27}$$

with the heat of steam formation $\Delta H_{f,H_2O(g)}$ nearly constant versus temperature over the operating range.

3.2.8 Momentum Balance

A steady-state momentum balance is applied to update the density and pressure for the fuel and air chambers as a function of system temperature. Pressure drop in the system has been considered to be approximately two-percent [71], and the model here assumes constant pressure along each chamber since a linear interpolation of the end pressure drops showed negligible effect on other properties. Consistent with all equipment models, the SOFC model calculates pressure using a downstream pressure as a model input. The pressure drop from chambers to downstream pressure is calculated as a function of frictional head loss. The equations involved in calculating the three SOFC pressures, p_{fuel}, $p_{air,1}$, and $p_{air,2}$, are shown as follows:

$$\rho_j = \frac{p_d}{R_g\,T_{j,avg}}, \tag{3.28}$$

$$v_j = \frac{\dot{m}_j}{\rho_j\,A_j}, \tag{3.29}$$

$$\mu_j = \alpha\, T_{j,avg} + \beta, \tag{3.30}$$

$$p_j = p_d + \frac{f\, L\, v_j^2}{2\, D_h}, \tag{3.31}$$

with the density ρ, downstream pressure p_d, gas constant R_g [J/(kg*K)], average chamber temperature T_{avg}, velocity v, mass flow rate $\dot{m}$, flow area A, viscosity μ, friction factor f, chamber length L, and hydraulic diameter D_h. The viscosity expression is an empirical fitting of temperature-dependent data.

3.2.9 Controlled Variables

The available SOFC controlled variables are calculated from the mass, energy, and electrical balances and are comprised of the minimum cell temperature $T_{electrolyte,min}$, maximum radial thermal gradient $\Delta T_{radial,max}$, power P, air utilization U_a, fuel utilization U_f, and efficiency η_{LHV}. The minimum cell temperature is simply the minimum electrolyte temperature in the axial direction. The radial thermal gradients are calculated as the difference between the mean layer temperatures divided by the radial distance at each radial element i. The radial thermal gradient between the anode and electrolyte layers is shown in Equation 3.32:

$$\frac{\Delta T_{sa-se,i}}{\Delta r} = \frac{\mid T_{sa} - T_{se} \mid_i}{0.5\;(thk_{sa} - thk_{se})}. \tag{3.32}$$

The gradient between the electrolyte and cathode is calculated in the same manner as Equation 3.32. The power is the product of current and voltage, $P = I\,V$, with the current I as the sum of all individual currents in each axial segment. The fuel utilization is equal to the amount of fuel consumed with respect to fuel supplied in molar quantities per Equation 3.33 [69]:

$$U_f = 1 - \frac{\dot{N}_{out,H_2} + \dot{N}_{out,CO} + 4\,\dot{N}_{out,CH_4}}{\dot{N}_{in,H_2} + \dot{N}_{in,CO} + 4\,\dot{N}_{in,CH_4}}. \tag{3.33}$$

Note that the fuel utilization equation requires stoichiometric coefficients. Air utilization is equal to the amount of oxygen consumed versus oxygen supplied and is calculated as shown in Equation 3.34:

$$U_a = 1 - \frac{\dot{N}_{out,O_2}}{\dot{N}_{in,O_2}}. \tag{3.34}$$

Efficiency is calculated by comparing power produced to the lower heating value (LHV) of fuel supplied as shown in Equation 3.35:

$$\eta_{LHV} = \frac{P}{H_{0,H_2}\,\dot{N}_{in,H_2} + H_{0,CO}\,\dot{N}_{in,CO} + H_{0,CH_4}\,\dot{N}_{in,CH_4}}. \tag{3.35}$$

Note that efficiency is not used as a CV in the control simulations herein but is available as a CV.

3.3 Ejector Submodel

3.3.1 Modeling Approach and Assumptions

Fuel cell ejectors operate as a mixer and avoid any moving parts by using the Venturi effect to recycle spent fuel flow with pure feed fuel flow. As shown in Figure 3.6, the secondary flow, spent fuel, is rich in steam at high temperatures and mixed with lower temperature, carbon-rich, primary flow feed fuel, delivered by an external fuel compressor. Primary flow is delivered at high pressure and low velocity from the compressor upstream (Section 0), and primary flow is accelerated at the de Laval nozzle throat (Section 1) to sonic speed as pressure energy is converted to kinetic energy. The primary flow further accelerates to supersonic speeds within the expander to the nozzle exit (Section 2). A lower pressure region occurs around the high-velocity primary flow and entrains the secondary flow. This effect is a direct result

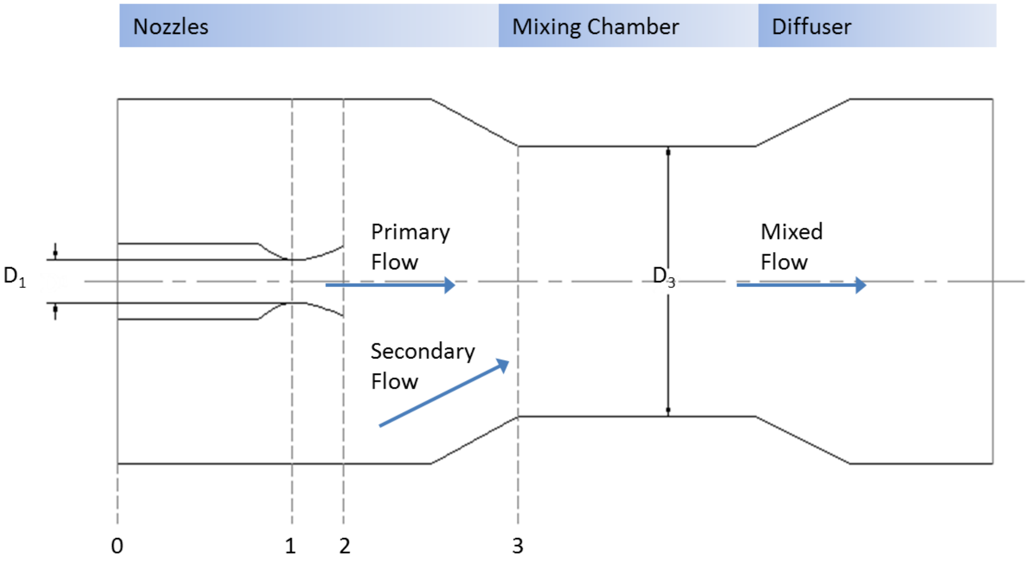

Figure 3.6: The SOFC ejector cross-section illustrates the four ejector flow regions

of the underexpanded primary fluid at Section 2 undergoing expansion upon exiting the nozzle to create suction between Sections 2 and 3. The entrained secondary flow accelerates from the entrance through the mixing chamber. The primary and secondary flows begin mixing at the entrance of the mixing chamber (Section 3) and are fully mixed at the outlet of the mixing chamber. In order to overcome the pressure drop from the fuel cell inlet to exit, the ejector converts the dynamic pressure of accelerated, mixed fluid to static pressure within the expander thereby increasing the recycled fuel pressure from ejector inlet to outlet. Acceleration to sonic conditions at the primary fuel nozzle throat is important to produce choked flow thereby ensuring that the mass flow is dependent solely upon the upstream pressure, excluding a downstream pressure contribution.

As a static component, the design of the ejectors is critical to produce the desired steady-state steam-to-carbon ratios, fuel flows, SOFC inlet temperature and pressure, and fuel and air utilization. The design is also important to provide dynamic control using the fuel inlet pressure or mass flow rate as an MV. In order to represent the ejector design, a steady-state one-dimensional ejector model is presented that is consistent with validated modeling approaches in literature [51, 82]. This model differs from common ejector models for refrigeration applications; in particular, fuel cell applications mix hot gases rather than saturated vapor and require a much lower pressure increase in the recycled flow. The model also uses a two-dimensional function for velocity as presented by Zhu [82]. Once the ejector model is combined with the SOFC and prereformer model in the Simulink sub-model, the ejector throat diameter D_1 and mixing chamber diameter D_3 are tuned along with other factors to provide the intended system design performance in an approach similar to Marsano [51]. The model presented here has a design point that approximates the Plant B SOFC inlet conditions as presented in Campanari for the inlet temperature, mole fractions, and fuel mass flow [17].

Several of the key modeling assumptions are discussed. The recycled and feed fuel flows are considered as ideal gases within adiabatic walls. Isentropic relations are used for calculating friction loss. The velocity of the recycled flow is non-uniform in the radial direction; feed fuel velocity is considered to be uniform in the radial direction. Pressure and temperature of all flows are uniform in the circumferential and radial directions.

3.3.2 Input and Output Variables

The ejector submodel receives inputs upstream from the fuel cell in the form of the secondary, entrained, gas temperature, pressure and mole fractions as shown in Table 3.3. In addition, the primary fuel gas temperature, pressure, and mole fractions are external manipulated variables. The ejector calculates the mixed fuel temperature, pressure, and mole fractions as outputs sent to the prereformer submodel, and the steam-to-carbon ratio is calculated as an external controlled variable.

3.3.3 Model Equations

The following ejector model is based upon model derivations by Zhu [82]. The equations may be grouped to calculate the primary states such that all equations within each group are solved simultaneously and implicitly, but groups of equations are solved sequentially, or explicitly.

Table 3.3: Ejector Submodel Input and Output Variables

Input

Variable	Description	Units	Source
$T_{p,in}$	primary fuel inlet temperature	K	external MV
$P_{p,in}$	primary fuel inlet pressure	bar	external MV
$T_{s,in}$	secondary fuel inlet temperature	K	SOFC
$P_{s,in}$	secondary fuel inlet pressure	bar	SOFC
X_{p,in,H_2-CO_2}	primary inlet fuel $H_2 - CO_2$ concentrations	$n/n\%/100$	external DV
X_{s,in,H_2-CO_2}	secondary inlet fuel $H_2 - CO_2$ concentrations	$n/n\%/100$	SOFC

Output

Variable	Description	Units	Sink
$T_{m,out}$	mixed fuel outlet temperature	K	prereformer
$\dot{m}_{m,out}$	mixed fuel mass flow	kg/s	prereformer
X_{m,in,H_2-CO_2}	mixed outlet fuel $H_2 - CO_2$ concentrations	$n/n\%/100$	prereformer
SCR	outlet steam-to-carbon ratio		external CV

3.3.3.1 Primary Flow

The fundamental equations for ejector primary flow are relations between the Mach number and velocity and an expression for the specific heat capacity of an ideal gas as shown in Equations 3.36 and 3.37 as follows:

$$V_p = M a_p \sqrt{k R_{g,p} T_p}, \tag{3.36}$$

$$c_p = \frac{k R_{g,p}}{k-1}, \tag{3.37}$$

with the ratio of constant pressure specific heat to constant volume specific heat k. The mass flow for the primary flow at Section 1 is derived by combining isentropic expressions for temperature, pressure, and density at Sections 0 and 1 with energy conservation accounting for thermal energy and kinetic energy. The average gas constant for primary flow is calculated as shown in Equation 3.38. The average density is calculated per Equation 3.40 with the gas constant for the primary fuel, $R_{g,p}$, calculated per Equation 3.39.

$$\dot{m}_{p,1} = \sqrt{\varphi k R_{g,p} T_{p,0}} \left(\frac{2}{k+1}\right)^{\frac{k+1}{2(k-1)}} \rho_{p,0} A_t, \tag{3.38}$$

$$R_{g,p} = \frac{Ru \sum_j N_{p,0}^j}{\sum_j N_{p,0}^j MW^j}, \tag{3.39}$$

$$\rho_{p,0} = \frac{p_{p,0}}{R_{g,p} T_{p,0}}, \tag{3.40}$$

The flow friction loss is considered by including an isentropic coefficient φ. The universal gas constant is denoted by R_u. The inlet moles $N_{p,0}$ can be calculated from the inlet mole fractions and from iteration with the calculated mass $m_{p,0}$ as shown in Equations 3.41- 3.44, given the conservation of mass.

$$MW_{p,avg,0} = \sum_j X_{p,0}^j MW^j, \tag{3.41}$$

$$\dot{N}_{p,0} = \frac{\dot{m}_{p,0}}{MW_{p,avg,1}}, \tag{3.42}$$

In order to calculate the secondary fuel mass flow rate, the diameter of primary and secondary flow at Section 3 must be calculated. To this end, the Mach number and velocity of primary flow are calculated in Equations 3.43-3.44.

$$M_{p,3} = \sqrt{\frac{2\left(\frac{p_{p,0}}{p_{s,0}}\right)^{\frac{k-1}{k}} - 2}{k - 1}}, \tag{3.43}$$

$$V_{p,3} = M_{p,3}\sqrt{k\,R_g\,T_{s,0}}, \tag{3.44}$$

The diameter of full expansion for the primary flow is calculated from mass and energy balances as shown in Equation 3.45 as follows:

$$D_{p,3} = \frac{D_t}{\xi_m}\sqrt{\frac{1}{M_{p,3}}}\left(\frac{2 + (k - 1)\,M_{p,3}^2}{k + 1}\right)^{\frac{k+1}{4(k-1)}}, \tag{3.45}$$

with ξ_m as the mixing frictional loss coefficient and D_t as the throat diameter at Section 1.

3.3.3.2 Secondary Flow

A novel improvement of the Zhu model is how it accounts for a non-constant velocity profile for the secondary flow in the radial direction at Section 3. The velocity of the primary flow is considered constant, but the velocity of secondary flow calculated as a polynomial. The expression for the velocity is shown in Equation 3.46.

$$v\left(r\right) = \begin{cases} V_{p,3} & 0 \leq r \leq R_{p,3} \\ V_{p,3}\left(\frac{R_3 - r}{R_3}\right)^{\frac{1}{n_v}} & R_{p,3} < r \leq R_3 \end{cases} \tag{3.46}$$

The exponent n_v is calculated from Equation 3.46 at $r = R_{p,3}$ as shown in Equation 3.47; this expression is derived based on the assumption that the temperature of the primary flow equals the temperature of the secondary flow at Section 3 and that the secondary flow has lost no heat energy.

$$n_v = \frac{\ln\left(1 - \frac{R_{p,3}}{R_3}\right)}{-\ln\left(M_{p,3}\right)} \tag{3.47}$$

To calculate the total secondary mass flow at Section 3, the mass flow is expressed as an integral equation between the limits of $r = R_{P,3}$ and $r = R_3$ with the flow area as a function of radius. The mass flow expression post-integration is shown in Equation 3.48.

$$m_{s,3} = 2\,\pi\,V_{p,3}\,\rho_{avg}\left[\frac{n_v\,R_3^2}{n_v\,+\,1}\left(1 - \frac{R_{p,3}}{R_3}\right)^{\frac{n_v+1}{n_v}} - \frac{n_v\,R_3^2}{2\,n_v\,+\,1}\left(1 - \frac{R_{p,3}}{R_3}\right)^{\frac{2\,n_v+1}{n_v}}\right] \tag{3.48}$$

The average density ρ_{avg} is calculated according to Equations 3.49 and 3.50.

$$R_{g,s} = \frac{R_u \sum_j N_{s,0}^j}{\sum_j N_{s,0}^j\,MW^j} \tag{3.49}$$

$$\rho_{avg} = \frac{P_{s,0}}{R_{g,s}\,T_{s,0}} \tag{3.50}$$

3.3.3.3 Energy Balance

The ejector outlet temperature is calculated by performing an energy balance over the ejector inlet and outlet as shown in Equation 3.51:

$$\sum_j m_{p,0}Y_{p,0}^0 c_p^j T_{p,0} + \sum_j m_{s,0}Y_{s,0}^0 c_p^j T_{s,0} = \sum_j m_4 Y_4^0 c_p^j T_4 + E_{loss}, \tag{3.51}$$

with the specific heat c_p calculated as a function of temperature per Equation 3.24; these equations are solved simultaneously to provide a more accurate temperature calculation than using a constant specific heat or no iteration.

3.3.3.4 Steam-to-Carbon Ratio

The steam-to-carbon ratio (SCR) is calculated based upon exit conditions from the ejector as shown in Equation 3.52.

$$SCR = \frac{\dot{N}_{H_2O}}{\dot{N}_{CH_4} + \dot{N}_{CO}} \tag{3.52}$$

This calculation of SCR is consistent with published literature [69, 82].

3.4 Prereformer Submodel

3.4.1 Modeling Approach and Assumptions

The prereformer breaks down higher hydrocarbons than methane and converts a portion of methane to hydrogen. The reformer is modeled as an adiabatic reactor with the heat necessary for reactions provided by the inlet fuel. A QSS assumption can be used since the states, temperature and mole fractions, are gas properties, consistent with the SOFC and ejector models. The lumped approximation is used since local temperature calculations within the prereformer are unnecessary.

3.4.2 Input and Output Variables

Upstream temperature, mass flow, mole balances, and system pressure comprise the input variables to the prereformer, and all inputs besides the pressure are provided by the ejector submodel as shown in Table 3.4. The prereformer submodel calculates the temperature, mole fractions, and mass flow resulting from the endothermic reformation reactions.

3.4.3 Model Equations

The prereformer lumped model calculates the outlet fuel temperature and mole fractions by evaluating steady-state material and energy balances. The material balance is evaluated with the same approach as the SOFC material balance as shown in Equation 3.53:

$$\dot{N}_{i,out} = \dot{N}_{i,in} + \sum_{j} v_i \, r_j. \tag{3.53}$$

Table 3.4: Prereformer Submodel Input and Output Variables

Input			
Variable	Description	Units	Source
T_{in}	fuel inlet temperature	K	ejector
$\dot{N}_{in,H_2-CO_2}$	inlet fuel $H_2 - CO_2$ molar flow rate	mole/s	ejector
$\dot{m}_{in}$	inlet fuel mass flow	kg/s	ejector
P_{system}	system pressure	bar	external MV
Output			
Variable	Description	Units	Sink
T_{out}	fuel outlet temperature	K	SOFC
X_{out,H_2-CO_2}	outlet fuel $H_2 - CO_2$ concentrations	$n/n\%/100$	SOFC
$\dot{m}_{out}$	outlet fuel mass flow	kg/s	SOFC

The energy balance is composed of transport terms and endothermic generation from the reformation reactions as shown in Equation 3.54:

$$\dot{N}\, MW\, c_p\, T_g\, |_{i,out} = \;\; \dot{N}\, MW\, c_p\, T_g\, |_{i,in}\, - \sum_j \Delta H_{ik}\, r_{ik}. \tag{3.54}$$

The specific heat is calculated as a function of temperature as shown in Equation 3.24, consistent with the SOFC submodel. The reaction model is composed of methanation and water-gas shift reactions identical to the SOFC reactions in Equation 3.3. Additional background for the reaction model is provided in the SOFC submodel modeling section and background chapter.

3.5 Summary

Steady-state and dynamic simulation results and validation are provided in Chapter 4. Steady-state simulations illustrate how well model matches with detailed models in literature and steady-state plant operating data. The model is extended for dynamic simulations, and the settling time and input-output relationships are discussed with reference to existing literature.

Chapter 4

SOFC System Simulation

4.1 Steady-State Simulation

The steady-state SOFC model presented in Chapter 3 is solved to provide the basis for a validated steady-state and dynamic model and to investigate manipulated variable (MV) and controlled variable (CV) interactions. For steady-state simulations, these manipulated and controlled variables are inputs and outputs of the fuel cell model rather than the full SOFC system model. The steady-state model uses a finer grid discretization than the dynamic model, and a comparison of results from the two levels of discretization demonstrates consistency between the models.

4.1.1 Steady-State Model Validation

Validation of the SOFC model involves several steps: (1) comparing the spatial distribution of temperatures and concentrations of the model without radiation to results from Campanari's tubular SOFC 2D model as commonly cited in SOFC literature [17, 71]; (2) incorporating radiation and comparing results to tubular SOFC 2D models having radiation [8]; and (3) comparing results from the present model to experimental data as performed by other researchers [17, 71]. The Campanari model is chosen for initial validation of the spatial variables due to insufficient data elsewhere to fully validate distributed parameter models. In all of these comparisons, the present model agrees with published results.

4.1.1.1 SOFC Model without Radiation

The SOFC model results are initially compared to results from Campanari's tubular SOFC quasi-two-dimensional model. The present model is designed after the tubular Siemens-Westinghouse design and obtains many parameters from Campanari. The present model calculates temperatures for each EEA layer whereas the Campanari model uses lumped solid temperatures. On the scale of this figure, all temperatures appear to match the cathode temperature, but individual anode, electrolyte, and cathode calculations are necessary for calculating radial temperature gradients. Since radiation is not included in the Campanari model, this initial version of the present model likewise neglects radiation.

A comparison of the steady-state model to Campanari's model illustrates how temperature profiles are similar in Figure 4.1. Note that all plots in this chapter refer to the 267.5 kWe SOFC plant with 3.5 bar operating pressure and power output near maximum capacity as the nominal condition; a 120.7 kWe plant case is only used for validation versus plant operating data. In Campanari's plot, T_a, T_c, T_s, and T_f refer to the anode, cathode, solid, and fuel temperature respectively.

The shape of temperature profiles are driven by several thermal mechanisms. Heat generated by ohmic resistance peaks near the center of the cell where current generation is highest. Likewise, heat generation from the

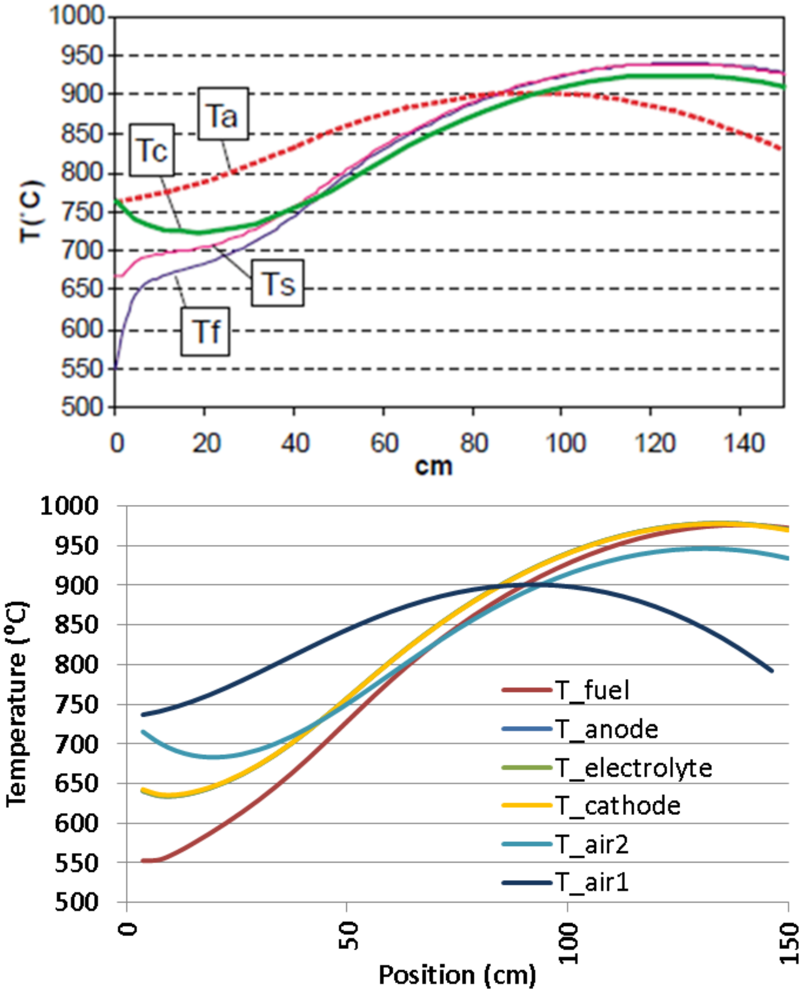

Figure 4.1: Temperatures for Campanari (upper) and the present model without radiation (lower)

exothermic electrochemical redox reactions increases with increasing current. The inlet fuel temperature, T_{fuel}, is lower than the air temperature at the same axial location. Inlet air temperature, $T_{air,1}$, cools as it passes through an air supply tube which provides some thermal insulation from EEA solid temperatures, T_{anode}, $T_{electrolyte}$, and $T_{cathode}$. The cathode-side air, $T_{air,2}$, converges towards the solid temperatures but later cools due to heat exchange with $T_{air,1}$. The solid air tube, temperature not shown because of the absence in Campanari's figure, exchanges heat via convection with both air temperatures. The temperature profiles demonstrate that the present model matches well with Campanari's model. The solid temperatures are most critical for SOFC reliability modeling, and the mean absolute percentage error for solid temperatures between the present model and Campanari's model is 3.85%. Note some difference exists in the fuel temperature near the inlet. This difference is exaggerated due to the coarser discretization of the model presented here, forty volumes; however, matching the fuel temperature match is less important than matching the fuel cell temperature.

Mole fraction profiles likewise match well with the Campanari mole fraction profile as shown in Figure 4.2. Fuel flows from the left-side of the figure. The fuel mole fraction profiles illustrate the steam reformation of methane. Until the methane is fully consumed near 40 cm, the steam concentration decreases and the hydrogen concentration increases. Following methane consumption, these two concentrations pass through extrema points and then progress monotonically with decreasing hydrogen and increasing steam. The carbon monoxide and dioxide curves are likewise driven by the extinction of the reformation reaction at 50 cm since carbon monoxide is a product of reformation and a reactant of the water-gas shift reaction.

Differences between the present model without radiation and Campanari model may be explained by modeling differences relevant for thermal and chemical characterization: (1) the Nernst equation is chosen to match com-

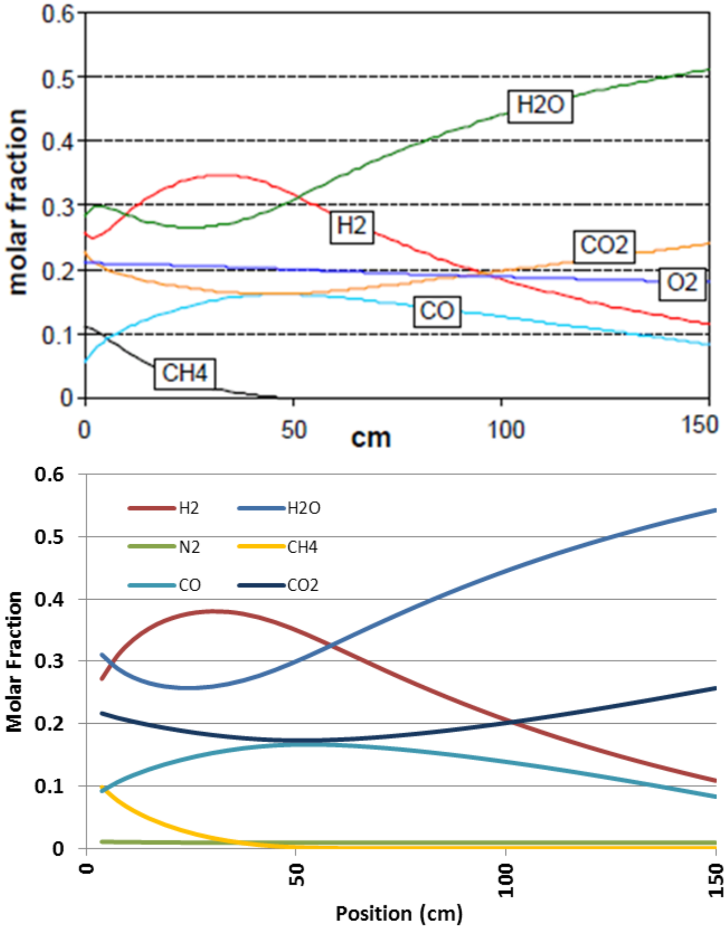

Figure 4.2: Fuel mole fraction profiles for Campanari (upper) and the present no-radiation model (lower)

mon formulations rather than the equation given by Campanari; (2) the fuel specific heat capacities are chosen based on a polynomial rather than a linear expression; and (3) discretization is more coarse in the presented model to reduce computational time, 40 vs. 100 volumes, or 3.75 cm vs. 1.5 cm axial resolution. In addition, several key equations and constants for the electrochemical reaction heat of formation, heat transfer coefficients, water-gas shift reaction, electrical resistance, and calibration variables are not provided by Campanari. The calibration variables chosen for the present model are discussed in detail within the tubular SOFC modeling approach and assumptions section in Chapter 3. The comparison demonstrates that the present model without radiation matches well with Campanari's model.

4.1.1.2 Final SOFC Model with Radiation

While the present model uses many of the same parameters as Campanari, radiation between the concentric air supply tube and cathode cannot be neglected at the high SOFC operating temperatures as noted by other models [71]. SOFC steady-state results from the present model with radiation demonstrate that radiative heat transfer is 10x larger in magnitude than conductive and convective radial heat transfer, which have similar magnitudes. Radiation heat transfer must be included for accurate modeling and to verify the final present model versus plant data.

The steady-state temperature and mole fraction profiles for the present model with radiation demonstrate that including radiation makes a significant difference in overall SOFC operation. Examining the temperature profile, the peak air temperature within the air supply tube is much closer to the peak solid temperature than without internal radiation heat exchange, and the entire temperature profile for the inlet air more closely matches the solid temperatures than without radiation. The temperature profile shown in Figure 4.3 matches well with the temperature profile shown by Barzi with electrolyte temperatures at the peak temperature and at 150 cm are in close agreement though inlet conditions are not completely defined by Barzi [8].

The electrolyte temperature at the anode chamber inlet is much lower than results presented by Barzi since he uses pure hydrogen as fuel, thereby avoiding endothermic steam reformation reactions at the anode chamber inlet.

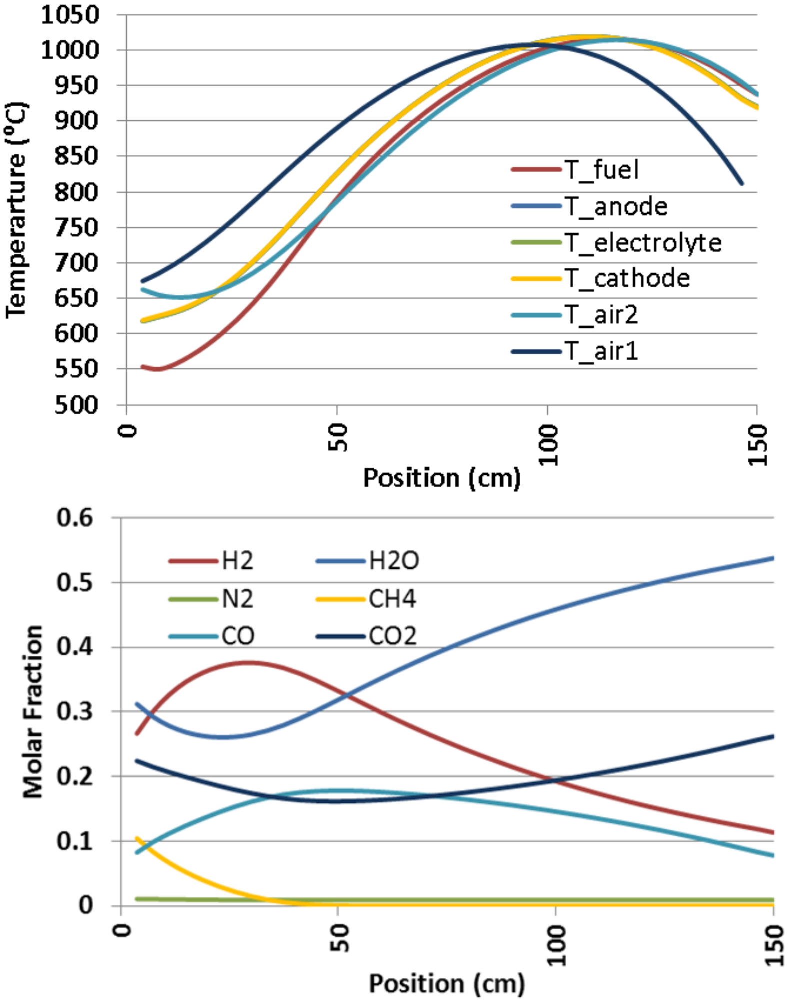

Figure 4.3: Temperature and concentration profiles demonstrate the effect of radiation

The effect of radiation on mole fraction profiles is less significant than the effect on temperature profiles. A higher peak for carbon-monoxide mole fraction indicates that the reformation reaction rate exceeds the water-gas-shift reaction rate deeper into the fuel cell than without radiation as shown in Figure 4.3.

The common validation approach for tubular SOFC models in published literature is to compare model results for steady-state power, current density, voltage, fuel utilization, and air utilization versus plant operating results [17, 71]. Two unique plants based on the Siemens-Westinghouse tubular SOFC design but having a different number of cells are run under different conditions. Plant A represents a 120.7 kWe SOFC plant comprised of 1152 cells operating at ambient pressure. Plant B represents a 267.5 kWe SOFC plant with 1704 cells operating at 3.5 bar. Besides these values, the fuel and air mass flows and cell voltage are provided as inputs from the plant data; Campanari estimates inlet fuel and air temperatures and inlet fuel concentration. In the final present steady-state model with radiation, total current density is specified as a user-identified input. Voltage is compared versus plant results along with power, fuel utilization, and air utilization as shown in Table 4.1.

The validation results illustrate that the present model with radiation matches the plant data within a similar accuracy as Campanari data. Error is calculated normalized to the expected results per plant data. The present model is more accurate to plant data for all outputs in the pressurized SOFC case than the Campanari model with a maximum of 1.6% error for fuel utilization. Error in both the present model and Campanari model may be attributed to the absence of complete inputs from plant data, discretization, and modeling assumptions.

Table 4.1: Validation of the SOFC steady-state model with plant operating data

Plant A	Model	Expected	Error	Campanari Error
Single cell power output (W)	109.0	104.8	4.0	1.6
Current density (A/m^2)	1792.0	1800.0	0.4	0.4
Voltage (V)	0.7294	0.6981	4.5	1.6
Fuel utilization (%)	68.4	69.0	0.8	0.6
Air utilization (%)	17.3	17.8	2.6	1.7

Plant B	Model	Expected	Error	Campanari Error
Single cell power output (W)	158.0	157.0	0.6	3.0
Current density (A/m^2)	3000.0	3000.0	0.0	1.1
Voltage (V)	0.6315	0.6275	0.6	3.0
Fuel utilization (%)	70.1	69.0	1.6	2.9
Air utilization (%)	23.8	23.8	0.1	1.7

Electrical characterization demonstrates how the primary sources of overpotential, activation, and ohmic losses move inversely to the local SOFC temperature as shown in Figure 4.4. Several phenomena occur as methane is fully consumed - current reaches its maximum value, and both losses decrease with activation polarization approaching zero. The activation losses occur as a result of chemical reactions that exchange electrons at the electrode; the decrease to zero is primarily driven by the increase in exchange current density with increasing temperature [45]. Ohmic losses likewise decrease with increasing temperature but at a slower rate. Examination of the current and ohmic loss profiles provides insight into heat generation. The peak heat generation due to ohmic resistance occurs at the same location as the peak current.

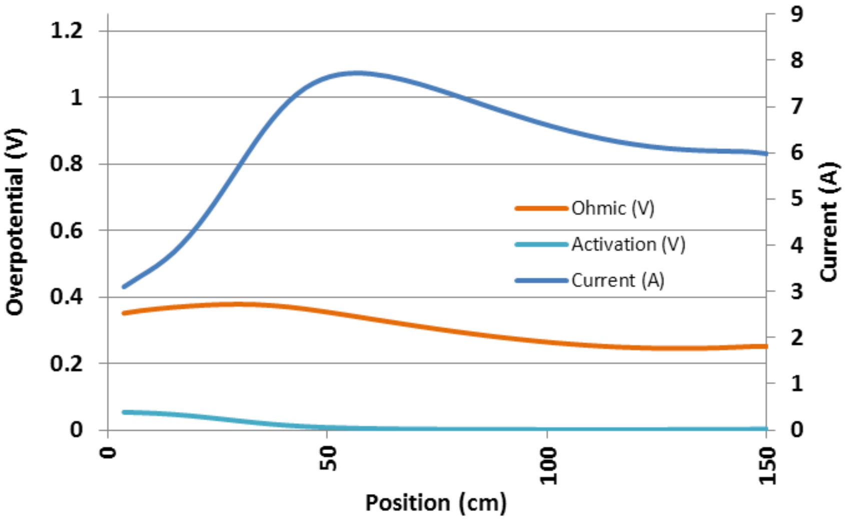

Figure 4.4: Overpotential and current distributions within the SOFC at steady-state

4.1.2 Multivariable Gain Analysis

The steady-state model is used to investigate multivariable interactions between potential manipulated and controlled variables as shown in Figure 4.5. The controlled variables are listed by row, and manipulated variables are listed by column. Note that these gains are specific to the SOFC model and do not include effects of the prereformer and ejector on steady-state performance. Additional CVs not shown were included in the study, such as axial temperature gradients and average stack temperatures; however, the absent CVs are not expected to be critical or accurate for reliability monitoring per published

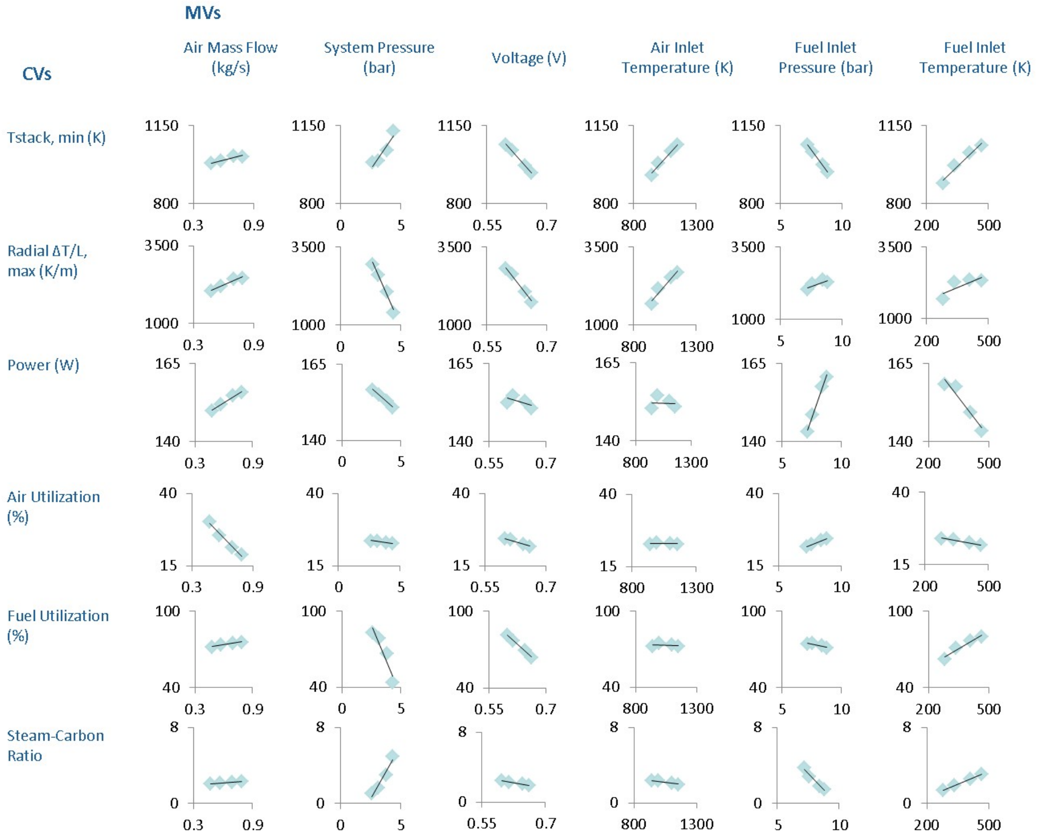

Figure 4.5: Multivariable MV and CV interactions for the SOFC

research on tubular SOFC reliability [30].

Steady-state gain analysis provides an initial measure of variable interactions for developing the control structure. The fuel inlet pressure and temperature have the most significant effect on power generation; voltage has a nonlinear effect on power due to the nominal value being near peak power at the nominal fuel flow rate. Air mass flow is the only significant MV affecting air utilization. The minimum stack temperature is affected by all MVs similarly besides air mass flow. The system pressure, voltage, and air temperature have a significant effect on the maximum radial thermal gradient. The system pressure is a primary driver for fuel utilization. Likewise, the system pressure and fuel inlet pressure have the most significant effect on the steam-carbon ratio. Dynamic simulations as presented later in this chapter provide a more conclusive measure of interactions. Though some variable combinations have significant steady-state gains, the time constant for an MV-CV interaction will determine conclusively whether an interaction is important for control.

4.1.3 Radial Temperature Gradient Analysis

Thermal analysis of SOFC is important for reliability characterization with regards to microcracking and thermal fatigue. Radial thermal gradients have a higher magnitude in tension than axial thermal gradients for the tubular SOFC since the EEA thickness is little more than 2.2 mm whereas the tube length is 1.5 m. At the fuel inlet side, the gas temperature gradient across the EEA is over 100 K at the nominal case as shown in Figure 4.3 and decreases as air and fuel temperatures converge. The anode gas, fuel, temperature is lower than cathode gas, air, temperature at this location thereby producing a negative radial thermal gradient with decreasing temperatures at larger radii. The anode and electrolyte will be placed in tension as the cathode thermally expands. As the barrier for charge transport, the electrolyte is particularly critical for cell lifetime.

Thermal analysis of SOFC is important for reliability characterization with regards to microcracking and thermal fatigue. Radial thermal gradients have a higher magnitude in tension than axial thermal gradients for the tubular SOFC due to the fuel cell aspect ratio. The anode gas, T_{fuel}, temperature is over 100 K lower than cathode gas, $T_{air,2}$, temperature at this location as shown in Figure 4.3 thereby producing a negative radial thermal gradient. The anode and electrolyte will be placed in tension as the cathode thermally expands. As the barrier for charge transport, the electrolyte is particularly critical for cell lifetime.

The difference between the maximum radial thermal gradient in tension versus the maximum axial thermal gradient is significant as shown in Figure 4.6. The maximum thermal radial gradient at nominal conditions is in excess of -2250 K/m whereas the maximum axial gradient remains below 750 K/m. Results by Fischer demonstrate a similar trend and magnitude for thermal gradients as those shown in Figure 4.6 at the location of worst gradients and likewise demonstrate that the greatest radial gradient is between the anode and electrolyte [30]. Conditions that decrease the fuel inlet temperature and increase the air temperature near the fuel inlet will cause the radial gradient to increase further.

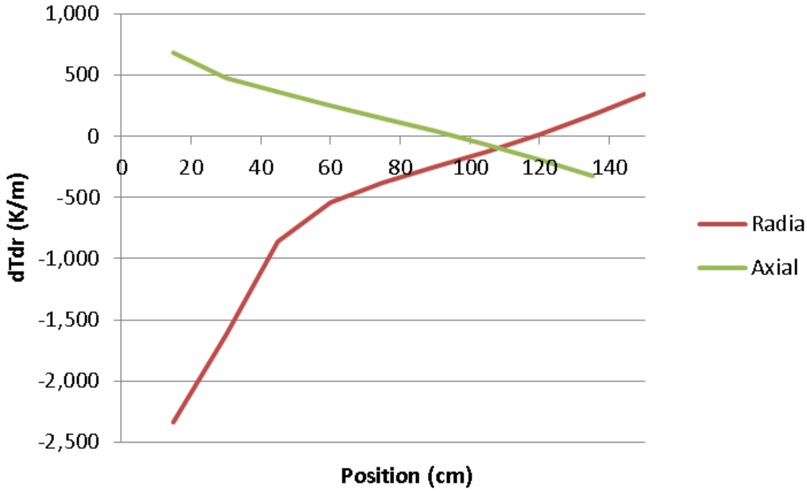

Figure 4.6: Axial and radial thermal gradients along the SOFC length at nominal conditions

4.1.4 Discretization Analysis

To reduce computational cost for dynamic simulations, the dynamic model is reduced to ten finite volumes from the steady-state model which contains forty volumes. A comparison of the SOFC steady-state temperature profiles at nominal conditions for each discretization level is shown in Figure 4.7. The ten volume model is near the forty volume model particularly near the fuel outlet. The MAP error for fuel cells temperatures in the ten volume model versus the forty volume model across the SOFC length is 7.58%. A majority of dynamic SOFC models presented in literature for control studies are lumped models as shown in Chapter 2. This comparison demonstrates the importance of discretization to producing accurate SOFC dynamic models, besides the need for discretization to calculate reliability CTQs. Further comparison of the ten and forty volume models is shown in Table 4.2. This table indicates how system outputs besides thermal outputs match well between the

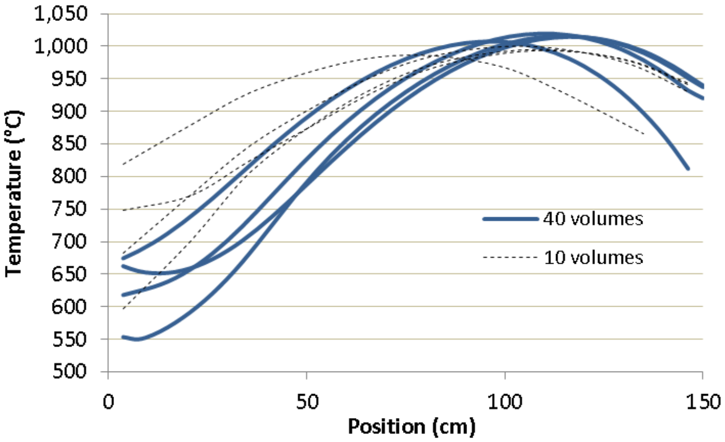

Figure 4.7: A comparison of temperature profiles for two levels of model discretization

two models.

Since lumped models are most often used in dynamic SOFC analysis, the difference between the ten and forty volume models is deemed acceptable for further dynamic controls and optimization studies using the ten volume model.

Table 4.2: **SOFC outputs at discretizations of 10 and 40 volumes**

	Volumes	
	10	40
Minimum stack temperature (°C)	682.34	617.86
Maximum radial thermal gradient (K/m)	2123.11	1857.14
Efficiency (%)	38.9	39.0
Power (W)	157.7	158.0
Air utilization (%)	23.8	23.8
Fuel utilization (%)	70.1	70.1
Current	250.26	250.2

4.2 Dynamic Simulation

Dynamic simulations of the SOFC system, as shown in Figure 3.2, are performed for verification of the dynamic model, investigation of manipulated-controlled variable interactions, and characterization of how disturbances affect controlled variables. The dynamic model involves solving a dynamic tubular SOFC submodel and quasi-steady-state ejector and prereformer models at each time step; further details of the model are provided in Chapter 3. Open-loop dynamic simulations characterize the SOFC system as follows:

- the SOFC system settling time subject to fuel pressure step changes.
- the dynamic model response at time steps of varying lengths.
- the effect of including transport time delays between submodels.

- the dynamic interaction of manipulated variables (MVs) and controlled variables (CVs) subject to staircase step changes in MVs.
- CV response to sinusoidal and step disturbances in methane fuel purity.

The dynamic simulations solve discretely at one second intervals in model time using MATLAB/Simulink, and within each time step, the SOFC system sequentially solves the submodels in the system model such that each submodel runs once per time step. The dynamic SOFC submodel solves all states and parameters simultaneously using constrained nonlinear programming (NLP) optimization with APMonitor/APOPT as the modeling language/solver. The quasi-steady-state ejector and prereformer submodels solve in MATLAB using the nonlinear least-squares algorithm *fsolve*. The dynamic model is used further in Chapter 5 for control model system identification and controller studies.

4.2.1 Dynamic Model Verification

Modeling and simulation (M&S) verification is the process of determining the degree to which the model accurately represents the intended description and specification for the model. Verification is unique from validation which involves confirming the model accurately represents real world phenomena [21]. Many researchers in SOFC modeling have noted the absence of experimental data for validating dynamic SOFC models, and particularly the tubular SOFC [13, 69]. Some researchers have validated the steady-state model based upon an experimental apparatus [78]. Others verify performance using published steady-state simulation and empirical results [8] and extend the steady-state model for dynamic analysis. Many individual equations used in SOFC modeling, such as chemical and electrochemical reaction rates, are based on empirically validated models as discussed in Chapters 2 and 3, and many dynamic tubular SOFC models shown in literature have consistent settling times, dynamic response characteristics (i.e., numerator dynamics or first-order responses), and MV-CV gain interactions. The model presented here should meet specifications as follows: having a consistent dynamic response versus the body of published literature in dynamic SOFC modeling and having a sufficiently small spatial and temporal discretization to have a negligible effect on accuracy.

4.2.1.1 Time Discretization

The SOFC dynamic model response to a voltage step change is examined using different discrete time steps in order to identify the largest time step size that provides sufficient accuracy in order to minimize computational time as shown in Figure 4.8. The simulation uses the full SOFC system including transport time delays. The dynamic power response demonstrates a significant reduction in settling time by reducing the discrete time step length from 30 s to 1 s and a diminishing effect with further reductions to 0.5 s. The 30 s simulation case has an 80 s artificial settling time difference from the 0.5 s case due to the coarse time discretization. The artificial time difference of the 1 s to 0.5 s case is approximately 3.5 s. The advanced control studies will use a controller time step and setpoint change time step greater than the time difference between 1 s and 0.5 s cases. In addition, the mass transport settling time is less than 1 s as discussed in Chapter 3 [13]. Thus, the 1 s case

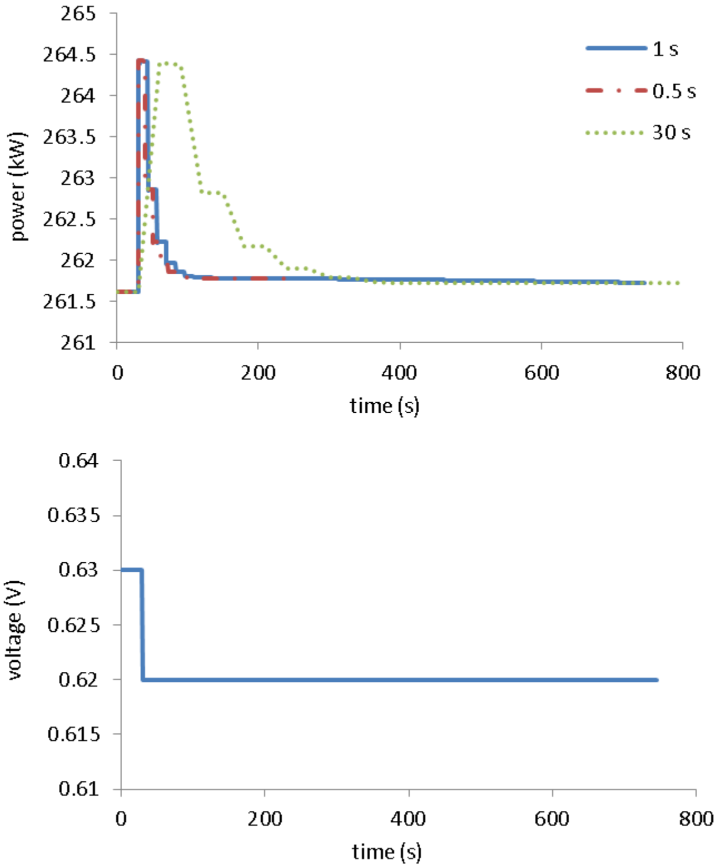

Figure 4.8: Dynamic response of the power to a voltage step at different time discretization levels

provides an acceptable compromise between dynamic response accuracy and computational time requirements.

4.2.1.2 Transport Time Delays

Since gas transport is modeled as QSS in the three submodels, a transport delay must be incorporated into the Simulink model to represent dynamics accurately. The transport delay calculation is updated based on the flow properties as shown in Equation 3.1. A voltage step, same as performed in the time discretization study, is applied to compare dynamics with and without transport delays. The dynamic response of fuel cell power and inlet fuel mass flow into the fuel cell are plotted as shown in Figure 4.9. The plots indicate that including gas transport delays affect the dynamic response within a time frame of 75 s from the change in manipulated variable. The absence of gas transport delays would affect the dynamics in a time range of interest for the control studies; therefore, including the gas transport delays will provide a more accurate dynamic response for the intended purpose of the dynamic

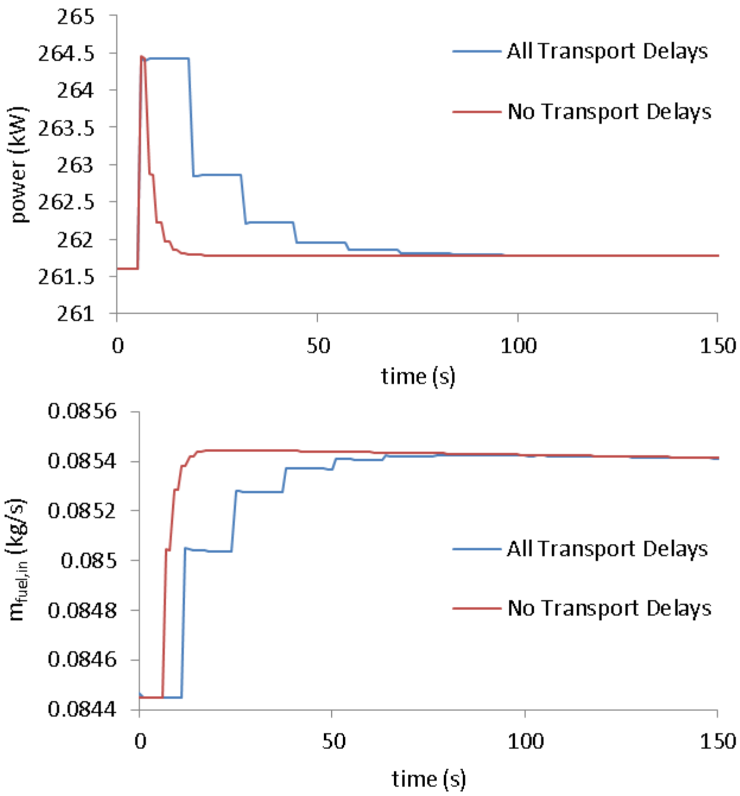

Figure 4.9: The fuel cell dynamic response with and without transport delays

model.

4.2.1.3 Open-Loop Settling Time

The open-loop dynamic response is examined by inducing an inlet fuel pressure step increase and decrease from the nominal, 8 ± 1 bar. The dynamic responses of the controlled variables, power, minimum cell temperature, steam-to-carbon ratio, radial thermal gradient, fuel utilization, and air utilization, are shown in Figure 4.10.

The open-loop dynamic response of the CVs provides insight into the physical phenomena associated with SOFC operation. As fuel inlet pressure increases, the power likewise increases, and the strong relationship between fuel pressure and power at steady-state as shown in Figure 4.5 holds during the dynamic simulation. The power response indicates both a fast and slow time constant suggesting numerator dynamics. For the step increase in fuel pressure, the power quickly reaches a maximum and then decreases with a slower, first-order approach to steady-state as shown in Figure 4.10(a); the fuel pressure step decrease has similar dynamics. The fast time constant is caused by the quick response of electrochemical reactions to changing fuel partial pressures. The slow time constant is attributed to thermal inertia causing a longer-term drift in SOFC properties until thermal equilibrium is reached.

The minimum cell temperature undergoes a first-order decrease to steady-state as the power increases and demonstrates a 95% settling time of 9846 s for the step increase and 2038 s for the step decrease. The thermal settling time

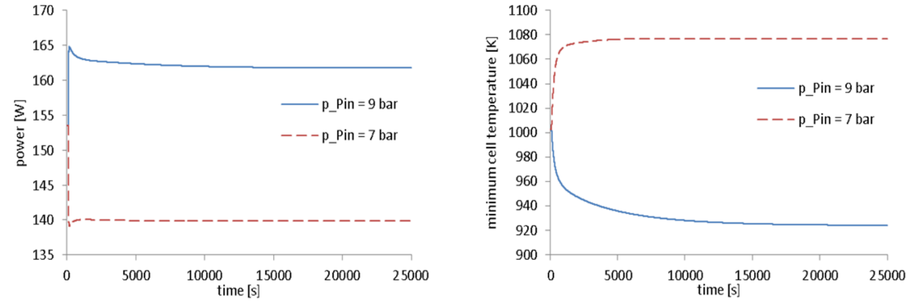

(a) power (W) (b) minimum cell temperature (K)

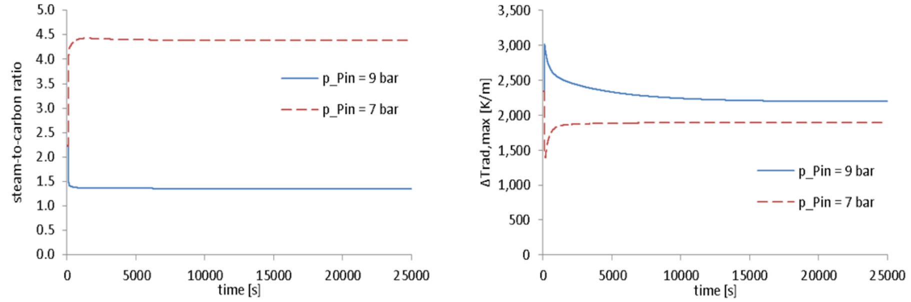

(c) steam-to-carbon ratio (d) ΔTrad,max (K/m)

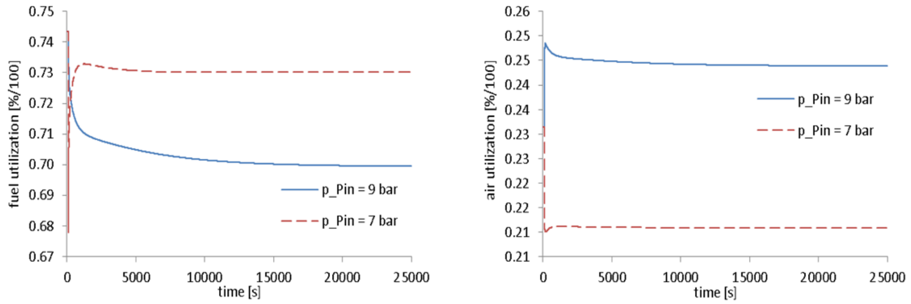

(e) fuel utilization (%/100) (f) air utilization (%/100)

Figure 4.10: Open-loop dynamic response to step changes in fuel inlet pressure

constant is consistent with literature that has been reviewed in this work. A key observation is that the minimum cell temperature moves inversely to power increases. This phenomenon is consistent with the body of tubular SOFC literature; as power increases, the fuel cell temperatures near the inlet and exit decrease while the maximum temperature increases producing a steeper axial profile. Since the cell temperature is constrained at a lower limit due to reliability concerns, increases in cell power may be limited by the temperature constraint.

The steam-to-carbon ratio (SCR) likewise moves inversely to the power with a first-order rise or decline. As seen in Figure 4.10(c), the SCR decreases rapidly below 1.5 simultaneously with the power increase. In this case, an increased fuel pressure increases the steam production rate but introduces carbon at a greater rate. The SCR demonstrates nonlinearity in how fuel pressure changes of equal magnitude cause an SCR response of differing magnitudes. The SCR will be an additional constraint when the controller moves to increase power from nominal.

Increasing power causes a direct increase in the maximum radial thermal gradient. This gradient demonstrates numerator dynamics similar to the power. The fast time constant for the maximum radial thermal gradient is a product of the quickly changing anode chamber thermal conditions. The step increase in fuel flow rate instantaneously decreases the anode ambient temperature. Since the maximum gradient occurs between the relatively thinner anode and electrolyte layers which are on the order of 10^{-6} m thick, the maximum radial gradient increases instantaneously with the fuel pressure increase, besides gas transport delays. As fuel cell EEA temperatures rise at a slower rate, the maximum gradient relaxes to a lower steady-state value. Since the maximum radial temperature gradient is constrained by an upper limit and increases simultaneously with power, it will be an additional constraint on power increases.

The dynamic response of fuel and air utilizations also exhibits numerator dynamics. The fuel utilization demonstrates a nonlinear response with differing dynamics for the fuel pressure increase and decrease. The increased fuel pressure and flow rate causes two phenomena that work together to decrease fuel utilization – an increased fuel consumption and power generation and a decreased cell temperature, which reduces reformation rates and increased ohmic losses. The decreased fuel pressure causes a prompt decrease in power, decreasing fuel utilization, but the rising fuel cell temperature increases reformation rates and reduces ohmic losses, improving efficiency and increasing fuel utilization. The air utilization moves in a similar manner as power with increased air utilization at a higher power level and vice versa.

4.2.2 Staircase Tests for MV-CV Interactions

Dynamic staircase tests are performed with the ultimate goal of identifying the necessary control structure for advanced SOFC control. The staircase tests identify signs and magnitudes of MV-CV gains, assess nonlinearities, and characterize the type of dynamic response (e.g., first order or numerator dynamics, rise time). Staircase tests provide a more detailed dynamic characterization than step tests since the staircase tests traverse a wider operating region.

In the present work, the staircase tests are performed by making sequential step increases or decreases in each MV independently with a first-order hold over 5 s at 300 s intervals and monitoring the dynamic response of CVs.

The staircase pattern of MV step changes is shown in Figure 4.11 for inlet fuel pressure; the pattern is identical for all MVs. Table 4.3 provides the size of MV step changes and highest and lowest values of the pattern. The step size is chosen to cover the feasible operating range of each control element. For example, the inlet fuel temperature is preheated with a recuperator, and thus room temperature is a reasonable lower limit for the fuel temperature MV.

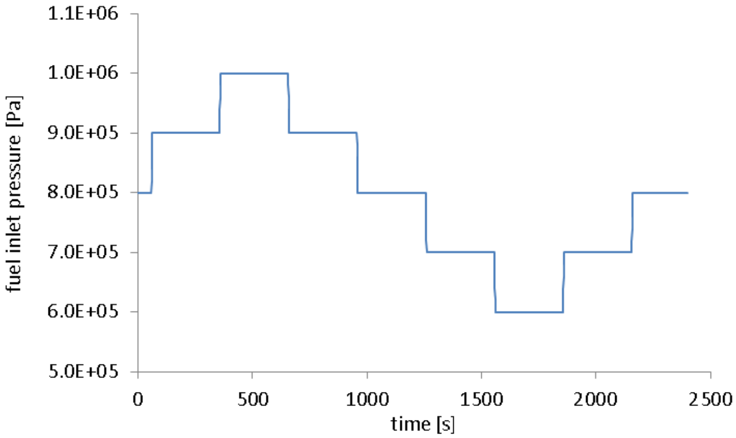

Figure 4.11: The MV step change pattern used for the staircase dynamic simulations

The staircase tests identify the inlet fuel pressure and inlet fuel temperature as the primary MVs for controlling power generation as shown in Figure 4.12. The inlet fuel pressure shows a direct relationship with power while the fuel temperature shows an inverse relationship. The pressure-power relationship has been explained previously in the open-loop settling time discussion. The power increases with lower fuel temperatures as the fuel becomes more dense at lower temperatures thereby increasing partial pressure. Voltage or current is often an MV for controlling power, but these variables become poor MVs as the current or voltage approaches the peak power at a given

Table 4.3: Staircase test parameters for the manipulated variables

Manipulated variable	Mean	Step size	Lowest value	Highest value
Inlet fuel pressure (bar)	8.0	1.0	6.0	10.0
Cell voltage (V)	0.6	0.04	0.55	0.71
Air mass flow (kg/s)	0.634	0.08	0.474	0.794
Air temperature (K)	1050.0	50.0	948.0	1150.0
Inlet fuel temperature (K)	373.0	50.0	273.0	473.0
System pressure (bar)	3.5	0.45	2.6	4.4

fuel and air flow rate. In this case the nominal power output of 153 W is shown to be near the peak power within the power-current curve. As voltage is increased from 0.6 V, the power decreases monotonically as expected when operating from the region to the left of peak power on the I-V curve as shown in Figure 4.12(b). However as voltage is decreased from 0.794 V to 0.474 V, the power begins to increase before decreasing during the last two step decreases in voltage. Power decreases at a faster rate when voltage reaches the lowest value. The voltage curve demonstrates that the power has reached and exceeded the peak power in the I-V curve; thus, the voltage is not an ideal MV for power control in this case. Note also that the numerator dynamics of the voltage-power relationship is consistent with published literature. As shown in Figure 4.12(f), the system pressure also has a fast effect on system power with numerator dynamics having a faster time constant for the output than the input derivative; however, changing the system pressure does not provide sufficiently increased fuel flow rates to control power well. System pressure, air mass flow, and air temperature have a negligible effect on power compared to the inlet fuel pressure and temperature.

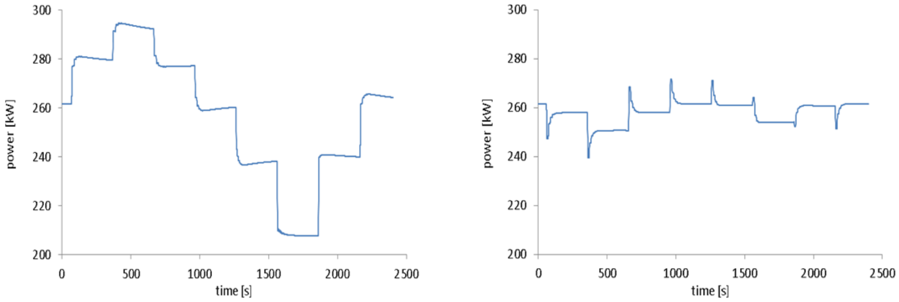

(a) MV: inlet fuel pressure (b) MV: cell voltage

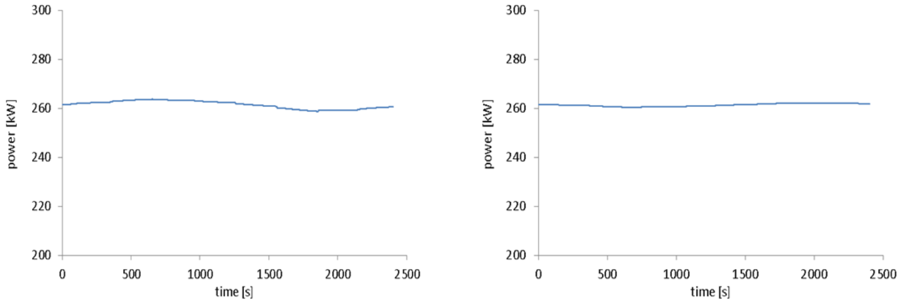

(c) MV: air mass flow (d) MV: air temperature

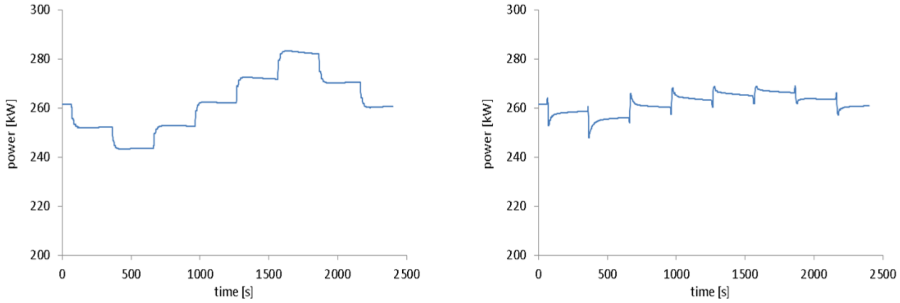

(e) MV: inlet fuel temperature (f) MV: system pressure

Figure 4.12: Dynamic response of power to staircase changes in MVs

Plots of the absolute cell temperatures demonstrates the effect of changing power and fuel cell conditions on temperature profiles as shown in Figure 4.13. As power increases during $t = 0 - 700s$ in Figure 4.13(a) and

$t = 700 - 1900s$ in Figure 4.13(e), the minimum temperature, Volume 1, decreases; the minimum cell temperature consistently decreases with increasing power, and vice versa. As power decreases to a minimum at 208 kWe, the minimum temperature rises steeply. Several effects contribute to this rise. The SOFC inlet receives fuel flow at a lower temperature than air flow; as the fuel flow decreases, the warmer air flow begins to dominate. As power decreases, the flattened temperature profile increases the percentage of current that flows through the SOFC volumes near the fuel inlet. The fuel temperature has a direct effect on the minimum cell temperature as expected. The third and final MV that has a significant effect on the minimum cell temperature is the system pressure. Increasing pressure causes an increased minimum cell temperature; this effect can be explained in relation to the power pressure-power plot. From $t = 0 - 700s$ the power decreases, current decreases, and temperature distribution becomes flatter. From $t = 700 - 1900s$ the current increases and temperature distribution becomes steeper. Another important conclusion from these plots is that the midpoint cell temperature at Volume 5 does not move parallel to the minimum cell temperature. This observation implies that the mean temperature is not an ideal CV for reliablity.

Plots of the maximum radial thermal gradients in Figure 4.14 demonstrate numerator dynamics for the inlet fuel pressure, inlet fuel temperature, and system pressure MVs. The numerator dynamics are expected since step changes in these MVs produce an instantaneous change in convection heat exchange on the anode surface, and the maximum radial thermal gradient is responsive to small changes in anode and electrolyte temperatures; the gradient is less responsive to changing cathode-side conditions due to the cathode

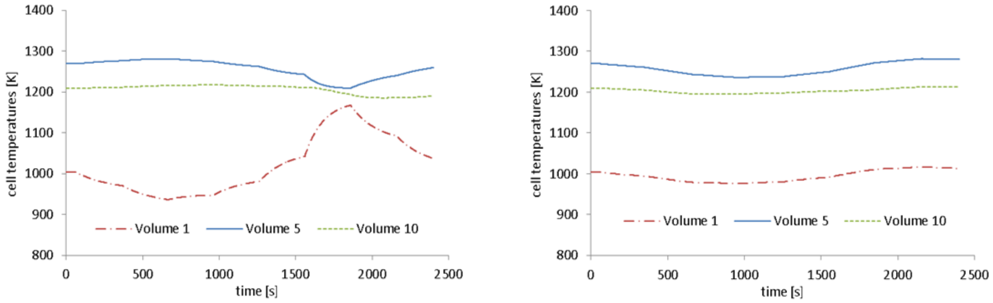

(a) MV: inlet fuel pressure (b) MV: cell voltage

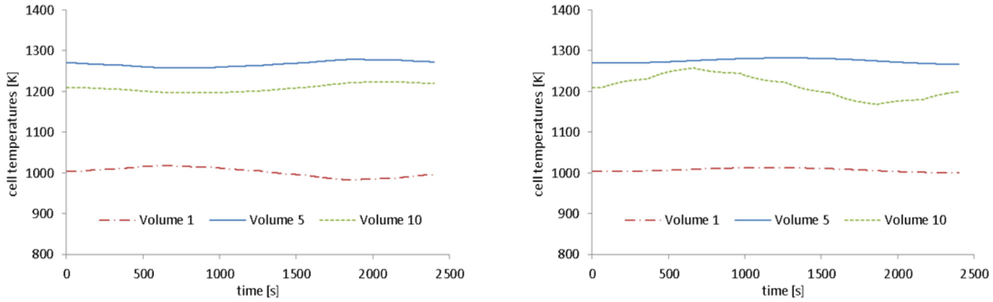

(c) MV: air mass flow (d) MV: air temperature

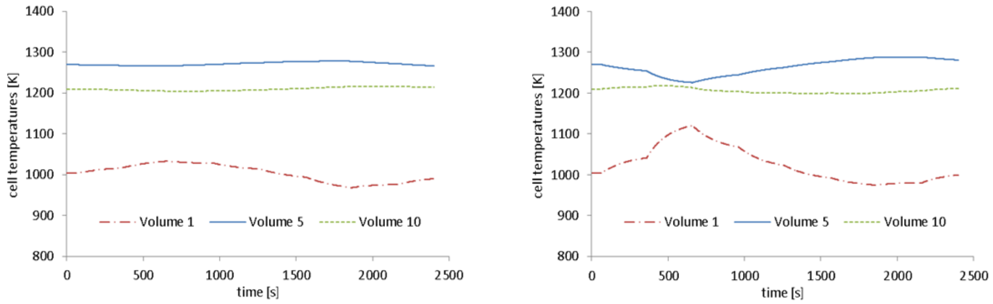

(e) MV: inlet fuel temperature (f) MV: system pressure

Figure 4.13: Dynamic response of cell temperatures to staircase changes in MVs

having a thickness one-thousand times greater than the other two EEA layers. The slower time constant for the gradient occurs as the fuel cell approaches thermal equilibrium. Increases in fuel flow rate and decreases in fuel temperature produce a higher thermal gradient due to greater anode-side convection.

The decreasing thermal gradient in response to increasing system pressure is attributed to the higher steam reformation rate producing more hydrogen, which has a specific heat several times other fuel species. Further support for this conclusion is that the maximum radial gradient occurs near the fuel inlet same as the reformation reaction.

The air mass flow, air temperature, and cell voltage may have a significant steady-state effect on the maximum radial thermal gradient as shown in Figure 4.5; however, the effect of these MVs is minimal within the time scale of interest. Dynamic analysis is critical for controller design to determine MVs that produce a significant and quick CV change. In addition, a key observation from the maximum radial temperature gradient plots is that increasing power causes higher gradients. Finally, unusual dynamic gradient behavior occurs in Figure 4.14(a) between $t = 1250 - 2000s$ with non-monotonic behavior occurring well past the MV step change. This behavior results when the location of maximum radial temperature gradient changes.

The steam-to-carbon ratio plots in Figure 4.15 indicate that all MVs besides air mass flow and temperature have a significant effect on the SCR, taken at the ejector exit. The SCR plots also demonstrate significant nonlinearities between the SCR and certain MVs, inlet fuel pressure and system pressure. As the inlet fuel pressure increases to its highest value, the steam mole fraction decreases to nearly an equal value with the carbon mole fraction. Since the recommended minimum SCR is approximately 1.8 to 2.0 per literature discussed in Chapter 2, increasing power beyond nominal will place the SCR in an unsafe operating zone. The cell voltage has an inverse relationship with

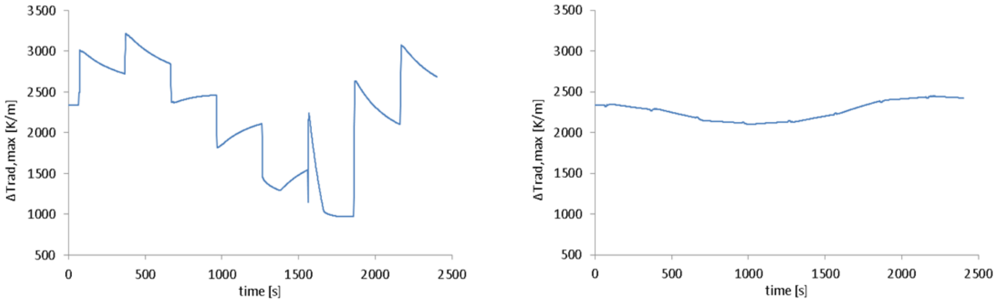

(a) MV: inlet fuel pressure (b) MV: cell voltage

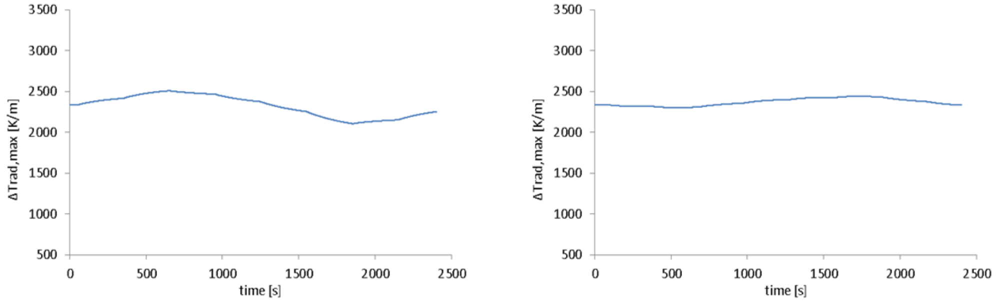

(c) MV: air mass flow (d) MV: air temperature

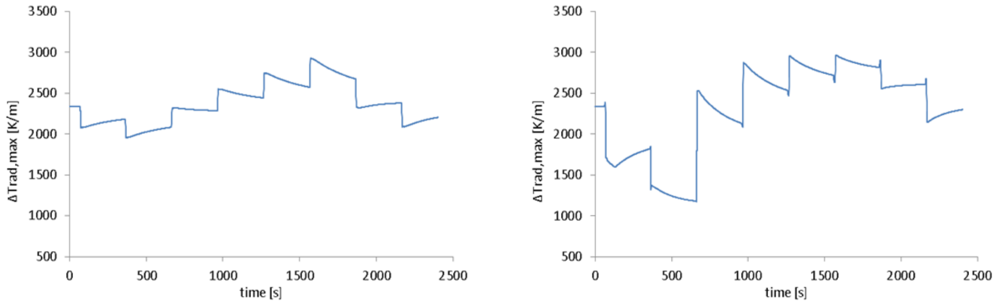

(e) MV: inlet fuel temperature (f) MV: system pressure

Figure 4.14: Dynamic response of the maximum radial thermal gradient to staircase changes in MVs

SCR due to the inverse relationship between voltage and current. The monotonic, inverse current-voltage relationship is demonstrated in Figure 4.17(b) since U_a moves directly with current per the redox reaction. Hence, the fuel cell will produce less steam via the electrochemical reaction at higher voltages as seen in Figure 4.15(b). Since higher temperatures lead to higher SOFC current, increasing the fuel temperature causes an increased SCR as seen in Figure 4.15(e). Increasing the system pressure shows a significant increase in SCR, indicating that the system pressure is a good candidate for controlling SCR. Higher system pressure increases the spent fuel recycle flow which contains steam. The air mass flow and temperature have a minimal effect on SCR in the timescale of interest due to ceramic insulation from the fuel stream.

The dynamic response of fuel utilization to staircase input steps, shown in Figure 4.16, indicates that the cell voltage is the primary MV for controlling U_f; the inlet fuel temperature and system pressure also have a significant effect. As discussed with the steam-to-carbon ratio plots, the cell voltage has a monotonic, inverse effect on cell current. Increasing the voltage will decrease current and thereby decrease fuel utilization in a linear manner within the ohmic loss regime, and vice versa, as shown in Figure 4.16(b).

The response of air utilization corresponds linearly with current dynamics for all plots in Figure 4.17 besides Figure 4.17(c) since oxygen depletion is linearly coupled to current generation. These plots demonstrate that air mass flow rate has the most significant effect on U_a when MVs travel within their feasible operating range. The inlet fuel pressure and cell voltage also have a significant effect on air utilization. Air utilization is defined as the percent of oxygen flow depleted by the fuel cell during operation. Since the air mass flow rate has a negligible effect on power as shown in Figure 4.12(c) for the present tubular SOFC, increased air flow rate naturally increases the amount of undepleted oxygen exiting the fuel cell. In following with the current-voltage

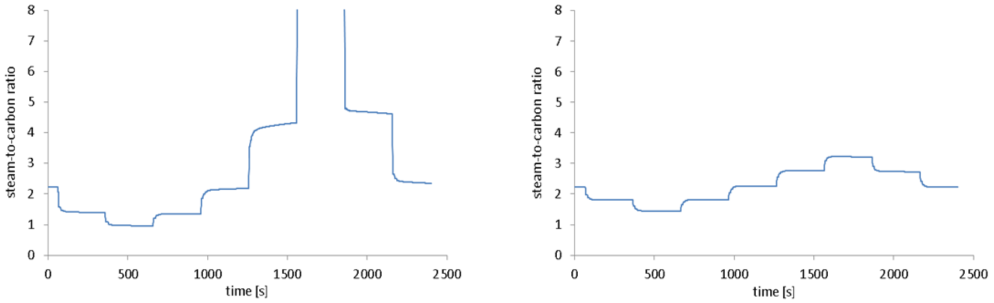

(a) MV: inlet fuel pressure (b) MV: cell voltage

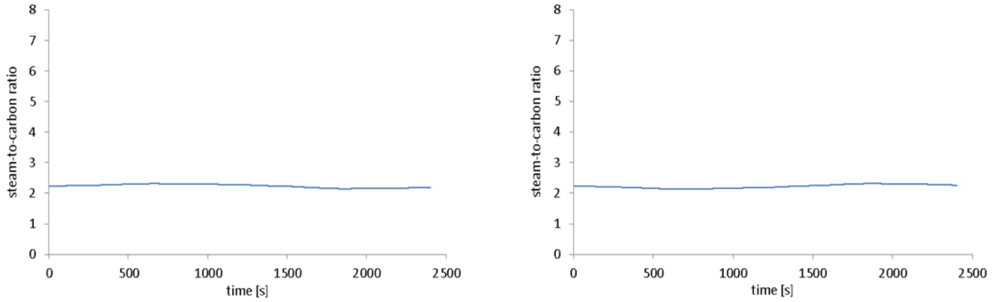

(c) MV: air mass flow (d) MV: air temperature

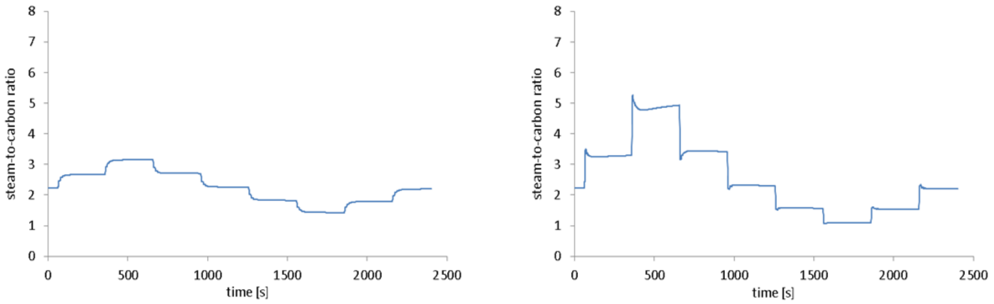

(e) MV: inlet fuel temperature (f) MV: system pressure

Figure 4.15: Dynamic response of the steam-to-carbon ratio to staircase changes in MVs

relationship already discussed in this section, increased voltage is expected to have a nearly linear effect on U_a although this effect diminishes at the lowest voltage, likely due to peak power being reached. The coupled effect of voltage on the temperature and steam reformation rate may have prevented

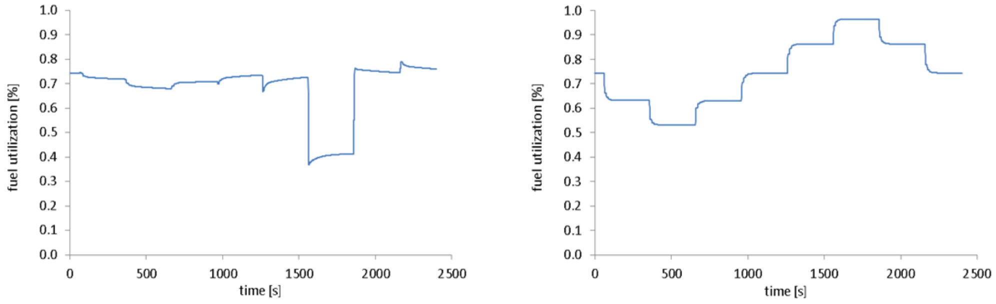

(a) MV: inlet fuel pressure (b) MV: cell voltage

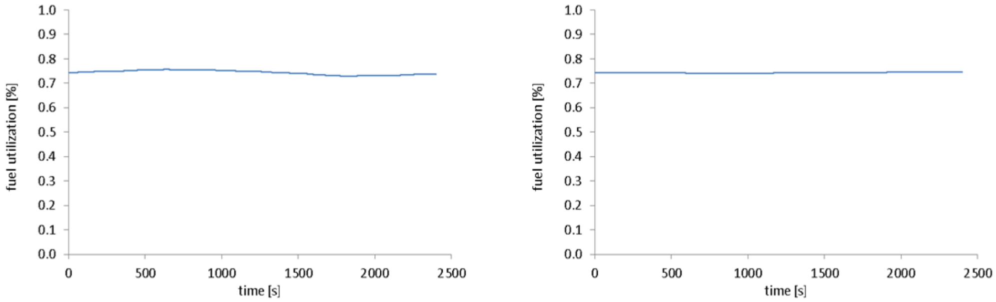

(c) MV: air mass flow (d) MV: air temperature

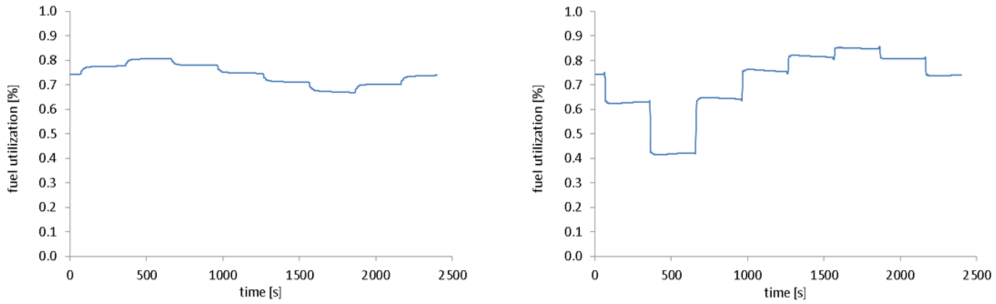

(e) MV: inlet fuel temperature (f) MV: system pressure

Figure 4.16: Dynamic response of the fuel utilization to staircase changes in MVs

numerator dynamics from occurring for the voltage-fuel utilization shown in Figure 4.16(b). Increasing inlet fuel pressure may be expected to increase air utilization since this also increases power generation.

The dynamic plots for efficiency shown in Figure 4.18 mirror those

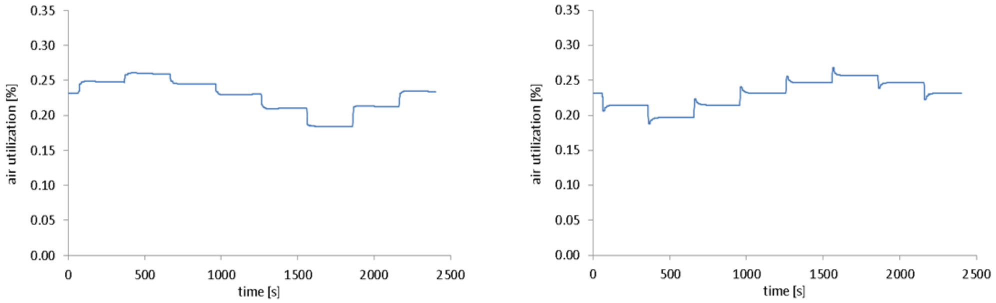

(a) MV: inlet fuel pressure

(b) MV: cell voltage

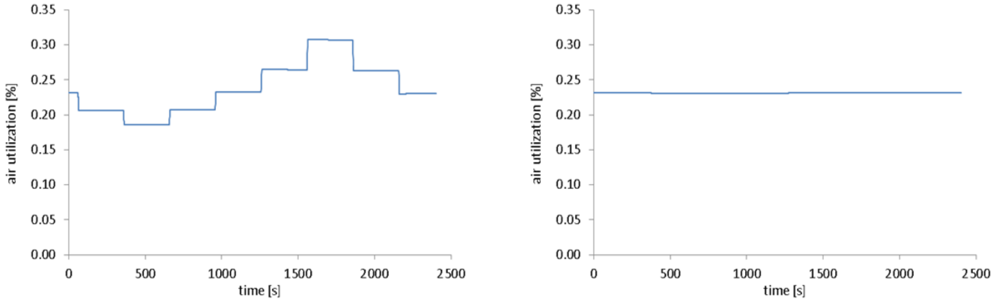

(c) MV: air mass flow

(d) MV: air temperature

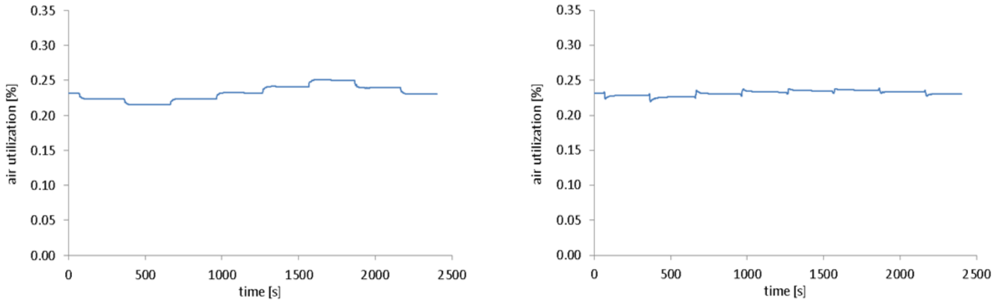

(e) MV: inlet fuel temperature

(f) MV: system pressure

Figure 4.17: Dynamic response of the air utilization to staircase changes in MVs

shown for the fuel utilization in Figure 4.16. This coupling is expected due to the definition of fuel utilization and efficiency. Efficiency is defined as the electrical energy produced divided by energy consumed, per a lower heating value (LHV) standard, in this case. Fuel utilization is the ratio of fuel consumed to fuel provided. The ratio between moles of hydrogen consumed to energy produced is constant for the electrochemical reaction. Therefore, as more fuel is utilized for a given amount of fuel provided, more power is produced relative to energy input. Also, moles of methane fuel are incorporated along with hydrogen in the same manner for fuel utilization and efficiency calculations.

Conclusions from the staircase tests are incorporated into the controller design. The air temperature has little dynamic effect on any CVs in the time frame of interest. The air mass flow primarily affects the air utilization, suggesting that the air mass flow is not needed to control other CVs. The plots demonstrate that increasing power without regard for other CVs will cause reliability variables, the minimum cell temperature, maximum radial thermal gradient, fuel utilization, and the steam-to-carbon ratio, to reach or exceed their safe operating limits.

4.2.3 Fuel Quality Disturbance Tests

The primary disturbance to SOFC operation is fuel quality variation. This disturbance is most likely to occur when the SOFC generates power for industrial applications, such as landfills, agriculture, chemical plants, and biofuel processing plants. A future promising application that would also require disturbance handling is electricity production using methane derived from algae proteins and carbohydrates. Natural gas produced as a biogas may contain CO_2 concentration in the range of 40% before scrubbing and $20-30\%$ after scrubbing [61].

To simulate fuel quality disturbances associated with biogas applica-

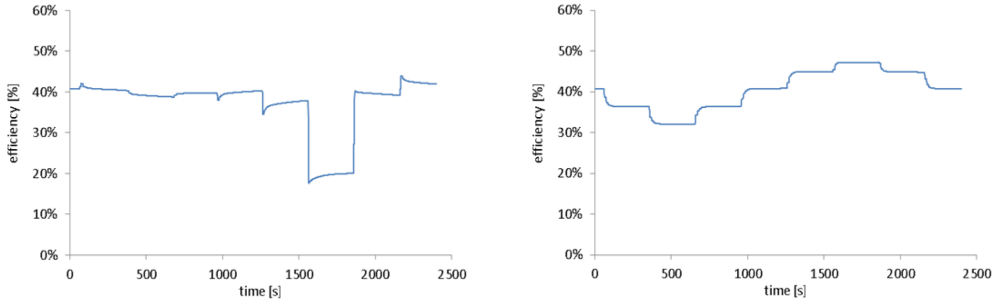

(a) MV: inlet fuel pressure (b) MV: cell voltage

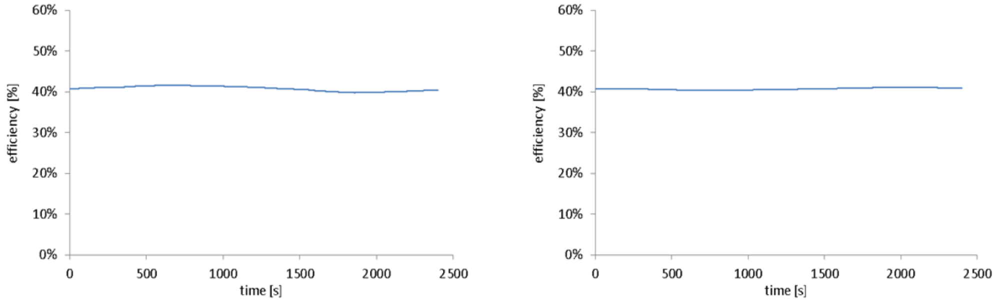

(c) MV: air mass flow (d) MV: air temperature

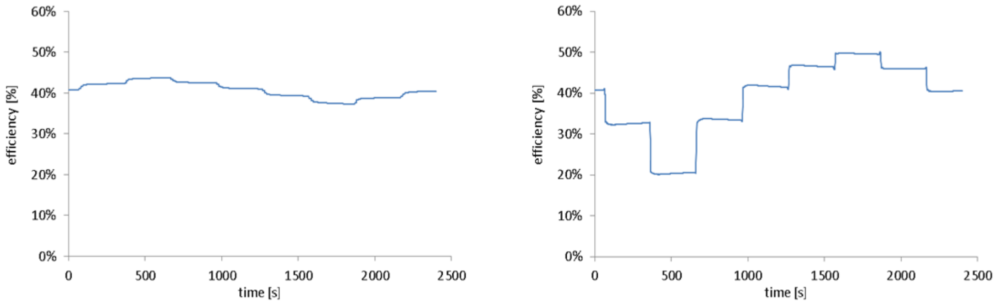

(e) MV: inlet fuel temperature (f) MV: system pressure

Figure 4.18: Dynamic response of the efficiency to staircase changes in MVs

tions, sinusoidal and step variations in CH_4 and CO_2 are sent to the plant during steady-state open-loop operation as shown in Figures 4.19 and 4.20. The sinusoidal variation is equal to ±10% from a nominal value of $90\% \, CH_4$, and the step size is a 15% decrease from the initial value of $100\,\% CH_4$.

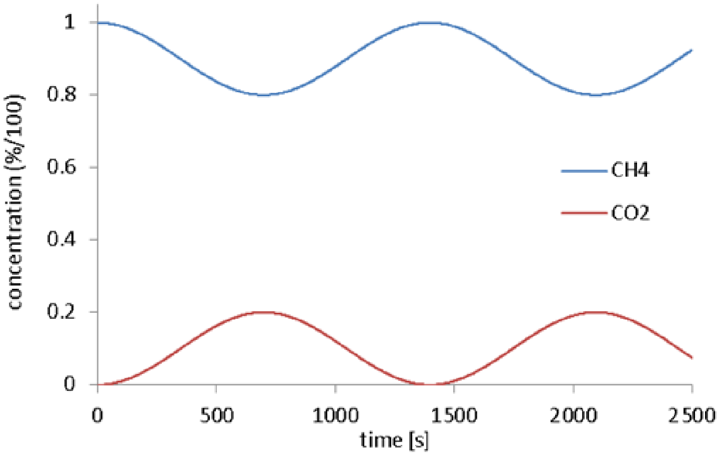

Figure 4.19: The sinusoidal disturbance in fuel quality

The purpose of the fuel quality disturbance tests is to assess how fuel quality variation affects the SOFC ability to satisfy load targets and reliability constraints. The dynamic response of CVs to the fuel quality variation is shown in Figure 4.21. The plots demonstrate that the valleys of CH_4 concentration coincide with valleys in power, the maximum radial thermal gradient, and

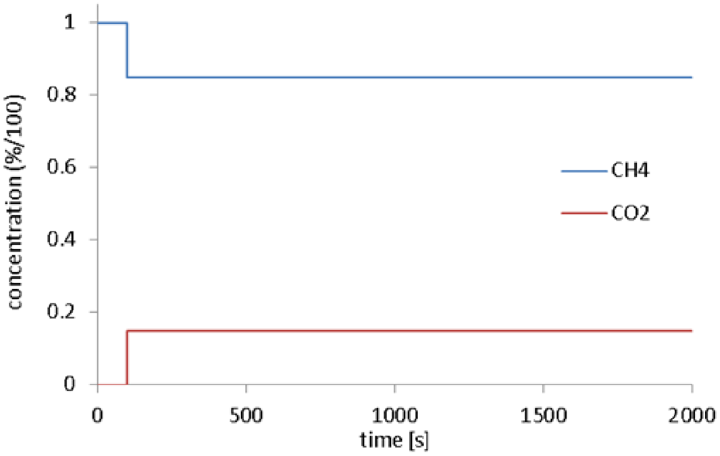

Figure 4.20: The step change disturbance in fuel quality

air utilization, and peaks in the minimum cell temperature, SCR, and fuel utilization. The mean of the sinusoidal plots also show slight trends upwards or downwards. A decrease in 20 % CH_4 concentration causes a 60 kWe, or 23 %, reduction in power output, and fuel utilization is in excess of 90%. Additional reliability CVs will be constrained if the controller seeks to maintain power output with lower methane concentrations.

The step decrease in CH_4 concentration by 15% causes a 44 kWe, or 17%, decline in power generation as shown in Figure 4.22. The result of the step decrease is similar as for the valleys in CH_4 concentration shown in Figure 4.21. Though power declines as less fuel is supplied, the fuel utilization simultaneously increases. The open-loop equilibrium for the SOFC favors a higher power output than if the fuel utilization had remained more steady.

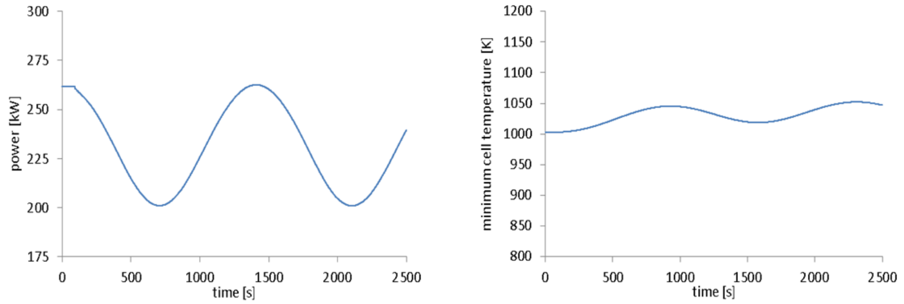

(a) power (W)   (b) minimum cell temperature (K)

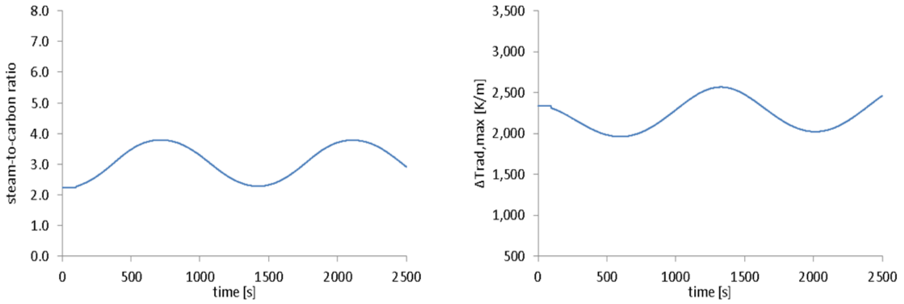

(c) steam-to-carbon ratio   (d) ΔTrad,max (K/m)

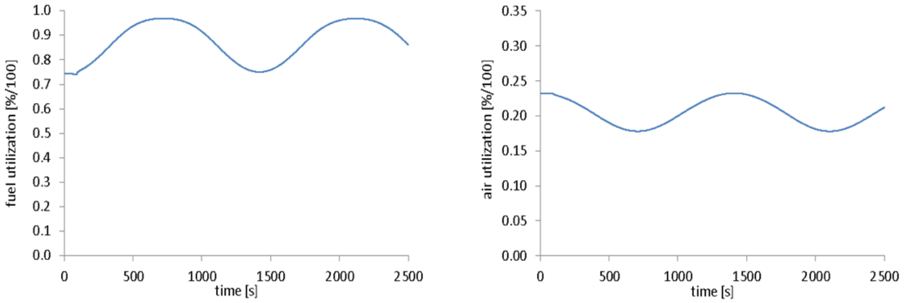

(e) fuel utilization (%/100)   (f) air utilization (%/100)

Figure 4.21: Open-loop dynamic response to sinusoidal variation in fuel CH_4 and CO concentration

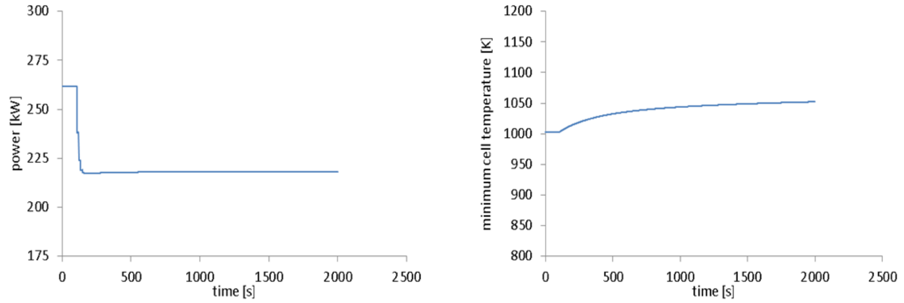

(a) power (W) (b) minimum cell temperature (K)

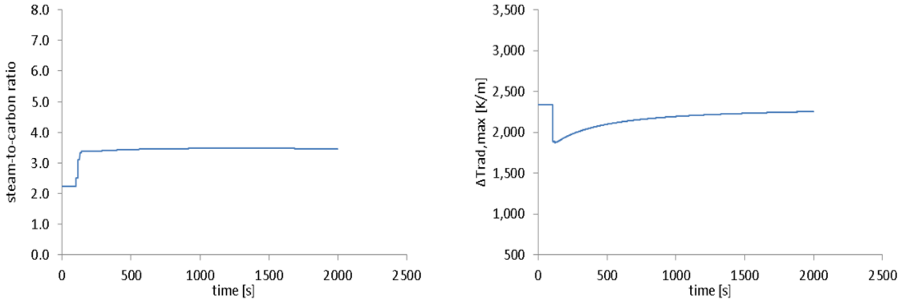

(c) steam-to-carbon ratio (d) ΔTrad,max (K/m)

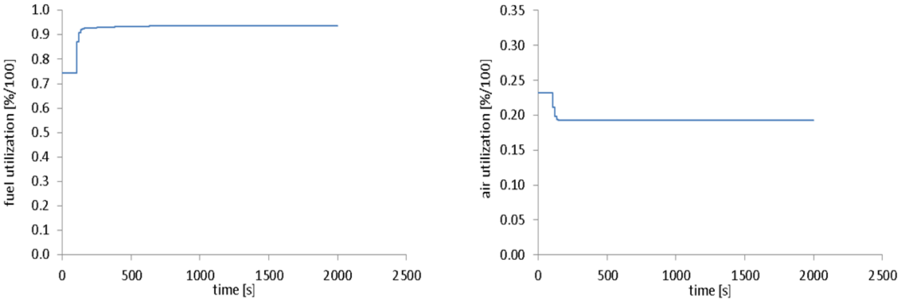

(e) fuel utilization (%/100) (f) air utilization (%/100)

Figure 4.22: Open-loop dynamic response to a step change in fuel CH_4 and CO_2 concentration

Chapter 5

MIMO Model Predictive Control

Planning the control strategy for an SOFC in particular requires prioritization of control objectives, particular consideration for the SOFC power system at hand, and understanding of the complex system dynamics and disturbances. Control of SOFC operation requires satisfying often competing performance and reliability objectives. Load-following is the primary performance objective, and efficiency maximization may be a secondary performance objective. Reliability goals primarily involve providing sufficient steam to prevent carbon deposition, ensuring thermal stresses do not cause premature fatigue or failure, and maintaining an adequate supply of fuel and oxidant for redox reactions. The SOFC geometry, flow configuration, and inlet conditions are primary factors requiring unique controller design for the system at hand. For instance, the primary driver for thermal stress in the tubular SOFC, the minimum cell temperature, is correlated with sintering temperatures. The endothermic steam reformation reaction produces a thermal sink at either the inner or outer diameter of the tubular SOFC depending on flow configuration. The SOFC dynamics are characterized by nonlinear, multivariable interactions between manipulated and controlled variables driven by electrical, chemical, and thermal time constants with orders varying from milliseconds to hours. Finally, common SOFC disturbances are ambient temperature and fuel quality variation. Various applications, particularly using biogas feed, may produce varying fuel purity, and controller robustness to these disturbances is examined. For the present model, heat transfer to the ambient through stack walls is not considered since the model represents a cell in the stack center, and gas temperatures are controlled, thereby mitigating the effect of ambient conditions on gas streams. Note that using a single cell model to represent all stack cells is a common assumption as discussed in Chapter 2.

In consideration of the complex dynamic interactions, unique system configuration, and competing control objectives, the need for advanced control of SOFC is apparent. Model predictive control (MPC) is an ideal general advanced controller that provides capability for constrained, multivariable model-based regulatory and tracking control. Constrained control satisfies reliability constraints with minimum effect on load-following, and multivariable models permit a more accurate prediction of system dynamic responses than SISO models.

5.1 Controller Design

The control system consists of two output feedback MPC controllers, one MIMO and one SISO. Most MVs and CVs have multivariable interactions, but $\dot{m}_{air}$ has no effect on most CVs besides U_a. For this closed-loop system, all CVs are measured outputs, and the Kalman filter converges on these outputs to estimate the initial conditions for the model states as shown in Figure 5.1. In a real system, some CVs, such as $\Delta T_{rad,max}$, will likely need to be calculated if not estimated using model-based estimation; the physical and empirical models

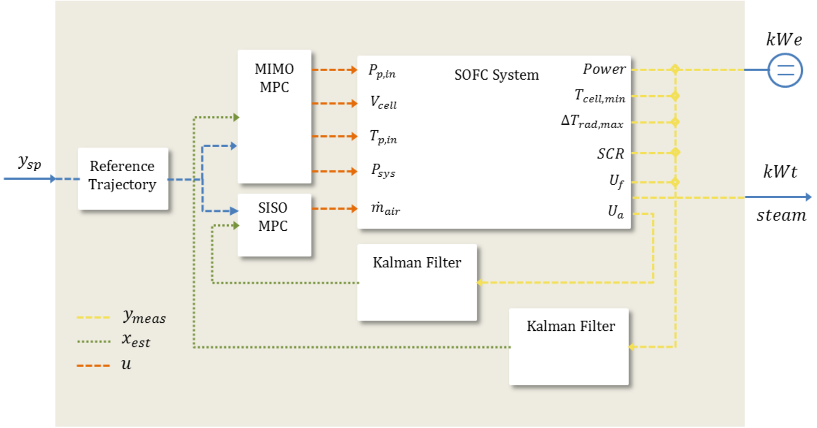

Figure 5.1: The SOFC linear model predictive control system architecture

used here to estimate $\Delta T_{rad,max}$ likewise may be extended for state estimation. While many authors have decoupled the multivariable SOFC control problem, the simulation results in Chapter 4 demonstrated how operability CVs respond in the same time scale as the power CV and have significant responses to the primary MVs for power control. Thus, coupling all interacting MVs and CVs is necessary.

5.1.1 Control Model Description

The control model is based upon a linear state-space model of ordinary differential equations (ODEs). The model as shown in Equation 5.1 is multivariable and discretized at the control time step of 10 s:

$$\begin{aligned} x_{n_x}(k+1) &= A_{n_x}x_{n_x}(k) + B_{n_x}u(k) \\ y(k) &= C_{n_x}x_{n_x}(k). \end{aligned} \tag{5.1}$$

The state-space model is derived from transfer function models, which are identified using the MATLAB System Identification Toolbox. The MISO transfer function model for each CV may be first- or second-order and may have numerator dynamics as shown in Equation 5.2:

$$\begin{aligned} Y(s) &= G(s)\,U(s) \\ G(s) &= \begin{bmatrix} \frac{K(\tau_a\,s+1)}{(\tau_1\,s+1)(\tau_2\,s+1)} & \cdots & \frac{K(\tau_a\,s+1)}{(\tau_1\,s+1)(\tau_2\,s+1)} \end{bmatrix}. \end{aligned} \tag{5.2}$$

The sum of transfer function orders for all CVs determines the state-space model index, n_x. Since the state-space model order is reasonably small, 22, no need exists for further model reduction. The transfer function model is identified from empirical input-output data produced with restricted and variable length random walk signals that span the feasible control region. To aid identification the gain signs and order of zeroes are constrained based upon expected behavior from staircase tests. The transfer function is converted to state-space form as shown in the appendices.

Integral action is incorporated into the state-space model by forming an augmented state-space model as shown in Equation 5.3:

$$\begin{aligned} \begin{bmatrix} \Delta x_{n_x}(k+1) \\ y(k+1) \end{bmatrix} &= \begin{bmatrix} A_{n_x} & 0_{n_x}^T \\ C_{n_x} A_{n_x} & I_{n_y} \end{bmatrix} \begin{bmatrix} \Delta x_{n_x}(k) \\ y(k) \end{bmatrix} + \begin{bmatrix} B_{n_x} \\ C_{n_x} B_{n_x} \end{bmatrix} \Delta u(k) \\ y(k) &= \begin{bmatrix} 0_{n_x} & I_{n_y} \end{bmatrix} \begin{bmatrix} \Delta x_{n_x}(k) \\ y(k) \end{bmatrix}. \end{aligned} \tag{5.3}$$

Integral action is necessary to eliminate the steady-state offset in closed-loop control due to plant-model mismatch. Note that the matrices and vectors are used throughout the remainder of the dissertation without size subscripts, n_x and n_y.

5.1.2 MPC Formulation

The model predictive controller is formulated as a nonlinear programming (NLP) problem and solved using the MATLAB *fmincon* interior-point solver. The objective function is formed to minimize the output error while suppressing control moves and suppressing use of slack variables as shown in Equation 5.4:

$$\min_{\boldsymbol{u(t)}} J = \frac{1}{2}\left(\mathbf{y}-\mathbf{y}_{ref}\right)^T \mathbf{Q}\left(\mathbf{y}-\mathbf{y}_{ref}\right) + \frac{1}{2}\Delta\mathbf{u}^T\mathbf{R}\Delta\mathbf{u} + \frac{1}{2}\boldsymbol{\xi}^T\mathbf{V}\boldsymbol{\xi}, \tag{5.4}$$

where $\boldsymbol{y}$ is the vector of CVs at all prediction time steps, $\boldsymbol{y}_{ref}$ is the reference trajectory, $\Delta\mathbf{u}$ is the change in MV between each control time step, and the slack variables are necessarily defined as $\boldsymbol{\xi} \geq 0$. Slack variables are included to provide soft constraints on outputs, $\boldsymbol{y}$. The objective function as shown in Equation 5.4 is further described as a function of state variables as shown in Equation 5.5:

$$\min_{\boldsymbol{u(t)}} J = \frac{1}{2}\left(\mathbf{x}-\mathbf{x}_{ref}\right)^T \widetilde{\mathbf{Q}}\left(\mathbf{x}-\mathbf{x}_{ref}\right) + \frac{1}{2}\Delta\mathbf{u}^T\mathbf{R}\Delta\mathbf{u} + \frac{1}{2}\boldsymbol{\xi}^T\mathbf{V}\boldsymbol{\xi}, \tag{5.5}$$

where

$$\mathbf{x}-\mathbf{x}_{ref} = \left(\Gamma\,\Delta\mathbf{u} + \Omega\, x_0\right) - \widetilde{\mathbf{C}}\,\mathbf{y}_{ref}, \tag{5.6}$$

and $\widetilde{\boldsymbol{C}}$ is a block diagonal matrix of C^{-1} and Γ is derived directly from Equation 5.3. Equations 5.3-5.5 demonstrate that the optimization problem is an NLP rather than QP. The objective function is not quadratic.

Constraints on the MVs and CVs ensure that the optimal solution to Equation 5.4 lies within the feasible region. Two types of MV constraints exist in this work. Actuator operating limits constrain the actuator operating range, and delta limits set a maximum limit on $\Delta\boldsymbol{u}$. Both may be incorporated as hard constraints (i.e., without slack variables). CV constraints are critical to remain within the safe operating region for extending SOFC lifetime; these are incorporated as soft constraints to prevent NLP infeasibilities as shown in Equation 5.7.

$$\begin{array}{ccccc} \boldsymbol{u_{min}} & \leq & \boldsymbol{u(k)} & \leq & \boldsymbol{u_{max}} \\ \Delta\boldsymbol{u_{min}} & \leq & \boldsymbol{u(k)-u(k-1)} & \leq & \Delta\boldsymbol{u_{max}} \\ \boldsymbol{y_{min}} & \leq & \boldsymbol{y(k)}+\boldsymbol{\xi(k)} & \leq & \boldsymbol{y_{max}} \end{array} \tag{5.7}$$

For the case when the disturbance is modeled, the $\Delta u(k)$ vector is augmented to include the measured disturbance, $d = X_{CH_4}$, as shown in Equation 5.8:

$$\Delta\tilde{u}(k) = \begin{bmatrix} \Delta u(k) \\ \Delta d(k) \end{bmatrix}. \tag{5.8}$$

The instances of $\Delta u(k)$ are replaced by $\Delta\tilde{u}(k)$ for the model prediction but not for constraint calculation.

5.1.3 Reference Trajectory

To provide for gradual, near monotonic setpoint tracking, the $\boldsymbol{y}_{sp}$ is filtered to produce $\boldsymbol{y}_{ref}$. When the higher level controller or operator provides a new load setpoint, the filter recalculates the reference trajectory according to a first-order transfer function as shown in Equation 5.9:

$$\boldsymbol{y}_{ref} = y_0 + \boldsymbol{y}_{sp}\left(1 - \exp\left(-\frac{t}{\tau_r}\right)\right) \tag{5.9}$$

where τ_r is a time constant chosen as a function of the prediction horizon and $t \epsilon [0, t_{ss}]$.

5.1.4 Analytical Derivatives

To expedite the NLP solution, analytical derivatives of the objective function are provided to the solver *fmincon*. The analytic Jacobian is calculated via matrix calculus as shown in Equation 5.10:

$$\begin{aligned}\frac{dJ}{d\tilde{\boldsymbol{u}}} &= \left[\frac{dJ}{d\boldsymbol{u}}, \frac{dJ}{d\boldsymbol{\xi}}\right]\\ \frac{dJ}{d\boldsymbol{u}} &= \Big((\mathbf{x}-\mathbf{x}_{ref})^T\,\widetilde{\mathbf{Q}}\,\Gamma\ +\Delta\mathbf{u}^T\mathbf{R}\Big)\,\frac{d\Delta\boldsymbol{u}}{d\boldsymbol{u}}\\ \frac{dJ}{d\boldsymbol{\xi}} &= \boldsymbol{\xi}^T\mathbf{V}\end{aligned} \tag{5.10}$$

5.1.5 Output Feedback State Estimation

Because the MPC algorithm uses a linear control model, a standard Kalman Filter is sufficient for reproducing the state variables from output measurements. For linear systems the Kalman Filter provides a linear unbiased minimum variance estimate. A brief overview of the state estimation algorithm is provided here as a complete description of Kalman Filtering. The following algorithm is iteratively performed at the current time for each measurement, j.

Taking the current time as $t = k$, the previous state vector, X_0, and covariance matrix, $\bar{P}_0$, at k - 1 is integrated forward to the current time to provide the *a priori* state estimation vector, X^-, and covariance matrix, $\bar{P}$, at time k as shown in Equation 5.11:

$$\begin{aligned}X^-(k)_j &= A_j\,X_0(k-1)_j\,+\,B_j\,\Delta u(k)_j\\ \bar{P}(k)_j &= \phi_j\,\bar{P}_0(k-1)_j\,\phi_j^T\\ \phi_j &= A_j.\end{aligned} \tag{5.11}$$

The *a posteriori* state vector, X^+, is calculated as the summation of X^- and a correction term, $\Delta x(k)$, based on the Kalman gain as shown in Equation 5.12:

$$\begin{aligned} X^{+}(k)_j &= X^{-}(k)_j + \Delta x(k)_j \\ \Delta x(k)_j &= K(k)_j\, \Delta y(k)_j \\ \Delta y(k)_j &= Y(k)_j \,-\, G(k)_j \\ G(k)_j &= C_j\, X^{-}(k)_j, \end{aligned} \tag{5.12}$$

where $Y(k)_j$ is the measurement j at time k and $G(k)_j$ is the measurement variable calculated from state estimates.

The Kalman gain, K, is calculated directly from matrix algebra as shown in Equation 5.13:

$$\begin{aligned} K_j &= \bar{P}(k)_j\, \widetilde{H}_j \left(\widetilde{H}_j \bar{P}(k)_j \widetilde{H}_j^T\right)^{-T} \,+\, R \\ \widetilde{H}_j &= C_j, \end{aligned} \tag{5.13}$$

where R is a weighting matrix chosen by the user, an identity matrix in this case the same for all measurements j. The state vector is updated j times, once for each measurement at the current time k.

5.2 Closed-Loop Control Results

The MPC controller described has been implemented in closed-loop with the dynamic SOFC plant as shown in Figure 5.1. The MPC tracking objectives and constraints are set as shown in Table 5.1 unless otherwise noted.

5.2.1 Controller Tuning

Initial studies are performed to identify satisfactory tuning values for the controller. Power is the only tracking variable with all other CVs con-

Table 5.1: Regulatory, tracking, and constraints settings for the MPC

	Regulatory	Tracking	Upper limit		Lower limit	
Power	off	**on**	off		off	
$\Delta T_{rad,max}$	off	off	**3,000**	K/m	off	
$T_{cell,min}$	**on/off**	off	off		**1,000**	K
U_f	off	off	**0.90**		off	
SCR	off	off	off		**2**	
U_a	off	off	**0.32**		off	

strained at either an upper or lower limit. A prediction horizon study is performed by implementing step changes in $\boldsymbol{y}_{sp}$ for power, an increase to 273 kW and decrease to 239 kW from a nominal 262 kW with a time step of 10 s; the control horizon is adjusted to be one-fourth the prediction horizon. Results are shown in Figure 5.2. The results indicate that the MPC controller generally satisfies the control objectives for prediction horizons of 5, 10, and 20. However, the prediction horizon *ph* of 5 time steps produces less satisfactory results in several areas: (1) the load profile versus time exhibits oscillatory behavior; (2) some overshoot is seen on the load decrease, and (3) the steam-to-carbon ratio briefly violates the lower limit during the steep load increase. The prediction horizon must be sufficiently long to compensate for the slow time response of $T_{cell,min}$. The controller must foresee that $T_{cell,min}$ is near the lower limit, as with a prediction horizon of 10 or 20 to prevent drastic MV moves driven by the load-following objective.

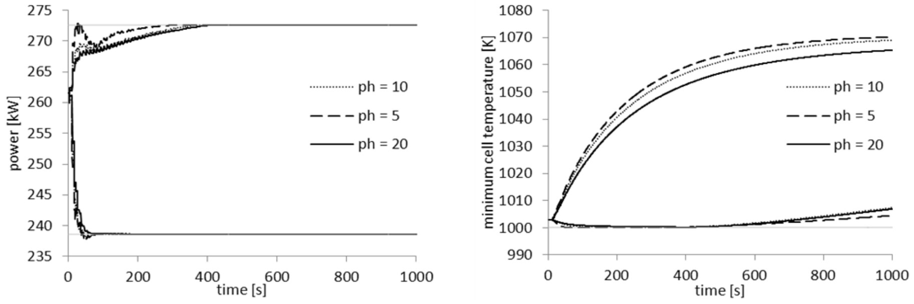

(a) power (W) (b) minimum cell temperature (K)

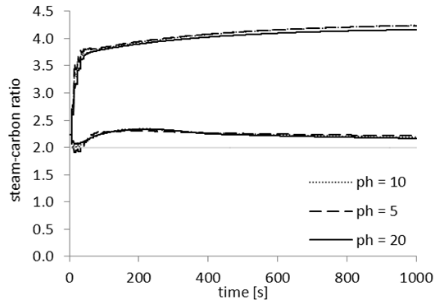

(c) steam-to-carbon ratio

Figure 5.2: Closed-loop load-following using different prediction horizons

The sampling time should be short enough to provide satisfactory control but sufficiently long to enclose the time period necessary for solving the MPC NLP optimization problem. On a 3.59 GHz PC running MATLAB/Simulink *fmincon*, the MPC problem with a prediction horizon of 20 solves in under 5 s. The sampling time study is performed for time steps of 5 s and 10 s, and the results are shown in Figure 5.3. A comparison of the two time steps indicates that the 5 s time step provides a negligible improvement in settling time while producing overshoot when the load setpoint is decreased. The overshoot is attributed to how the 5 s case weights load error greater than the 10 s case – a prediction horizon of 20 is used for the 5 s case vs. a

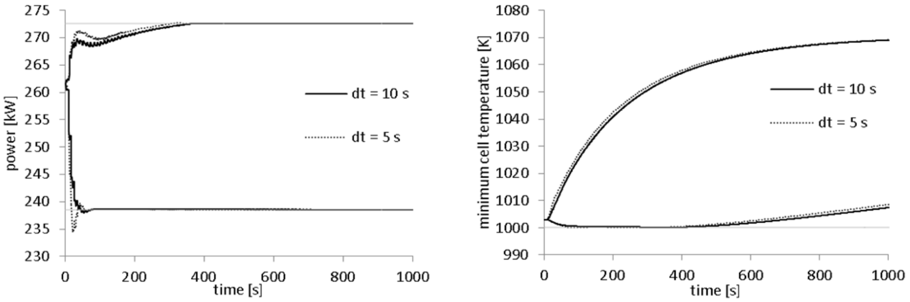

(a) power (W) (b) minimum cell temperature (K)

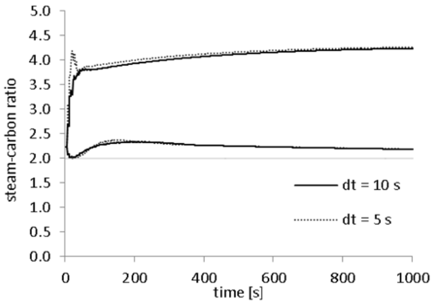

(c) steam-to-carbon ratio

Figure 5.3: Closed-loop load-following using different sampling times

horizon of 10 for the 10 s case to ensure both cases predict the same length of time. Weighting was adjusted to provide a similar ratio of load error penalty to minimum cell temperature constraint penalty. The main conclusion is that the 10 s case provides satisfactory control versus the 5 s case.

5.2.2 Load-Following

The load-tracking capability of the SOFC MPC is further examined with four simulations each at unique load setpoints: 205, 239, 273, and 290 kWe. The manipulated variables (MVs) are constrained based upon feasible operating limits for continuous operation. For instance, the system pressure may drop to atmospheric following a shutdown, but during continuous operation the compressor may only safely span a range of pressures for a given range of air mass flow rates. The inlet fuel pressure lower limit of 6 bar is chosen heuristically to demonstrate operation at the constraint and may be set lower for continuous operation. Results for controlled variable responses are shown in Figure 5.4. As shown in Figure 5.4(a), the SOFC power does

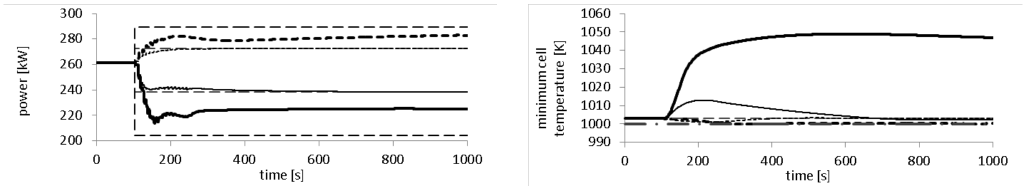

(a) power (W)

(b) minimum cell temperature (K)

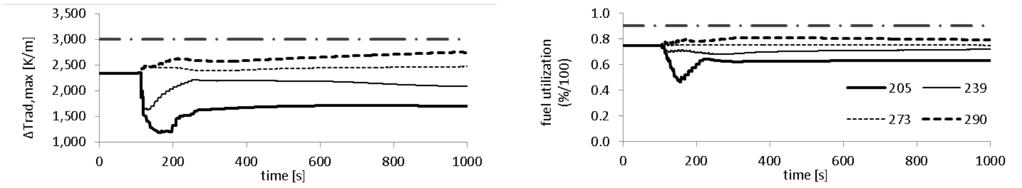

(c) $\Delta T_{rad,max}$ (K/m)

(d) fuel utilization (%/100)

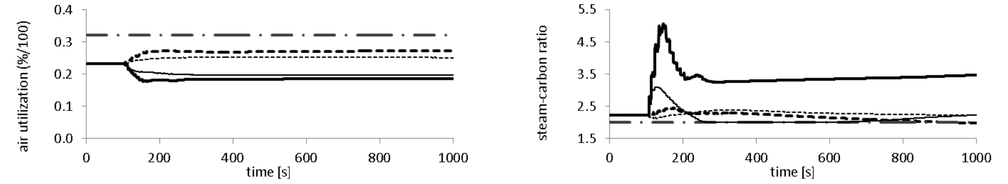

(e) air utilization (%/100)

(f) steam-to-carbon ratio

Figure 5.4: Closed-loop load following at different load set points

not reach the targets of 205 or 290 kWe. The minimum cell temperature limit may contribute to constraining the rise to 290 kWe as shown in Figure 5.4(b). However, the decrease to 205 kWe does not cause any CVs to reach limits. Rather, the restricted load following to 205 kWe is caused by the MV limits as shown in Figure 5.5. All four MVs reach limits for the load decrease to 209 kWe, and all MVs besides the inlet fuel temperature contact limits for the load increase to 290 kWe. As the inlet fuel temperature in this latter case moves away from the limit around 300 s, the the minimum cell temperature for the same case is riding along the constraint as seen in Figure 5.4(b). The minimum temperature CV constraint explains why the inlet fuel temperature is not permitted to reach its MV constraint. The successive power increases cause successive increases in the maximum radial thermal gradient as shown in Figure 5.4(c).

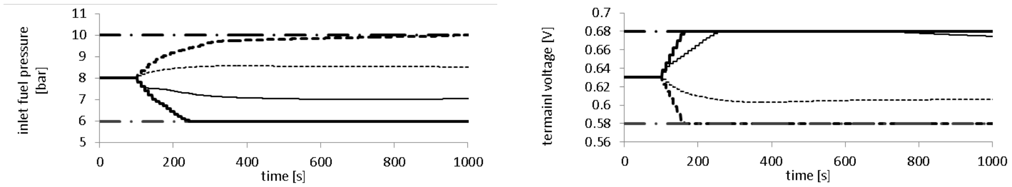

(a) inlet fuel pressure (bar)

(b) terminal voltage (V)

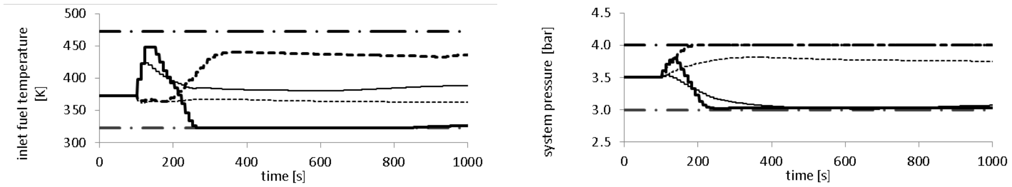

(c) inlet fuel temperature (K)

(d) system pressure (bar)

Figure 5.5: MV profiles for the closed-loop load following at different load set points

5.2.3 Reliability Control

Common SOFC control strategies involve using a lumped dynamic simulator and controlling either a lumped (i.e., average) cell temperature or an outlet gas temperature without using constrained CV control. As noted already, a lumped model cannot capture two critical reliability CVs for the tubular SOFC, the maximum radial thermal gradient and minimum cell temperature. Now, the MPC algorithm is used to test whether controlling the average cell temperature or outlet gas temperature provides satisfactory control of these two reliability CVs. This test is performed by using the following tracking variables: (1) load, and (2) either minimum cell temperature, average cell temperature, or outlet gas temperature. In the latter two cases, to ensure only the average cell temperature or outlet gas temperature tracking is affecting the minimum temperature profile and provide a better comparison with unconstrained control, all CV limit constraints are removed. Results for the CV and MV profiles are shown in Figures 5.6, 5.7, and 5.8.

In the load and minimum cell temperature tracking case, the load monotonically increases to the setpoint while the minimum cell temperature and steam-to-carbon ratio are prevented from exceeding lower limit constraints as seen in Figure 5.6. The minimum cell temperature is also held within a range of 10°C while the mean cell temperature drifts over 100°C from the initial value; however, since the mean temperature has no direct effect on reliability, this controller meets reliability objectives.

In the load and average cell temperature tracking case, the load likewise reaches the setpoint monotonically, but the minimum cell temperature

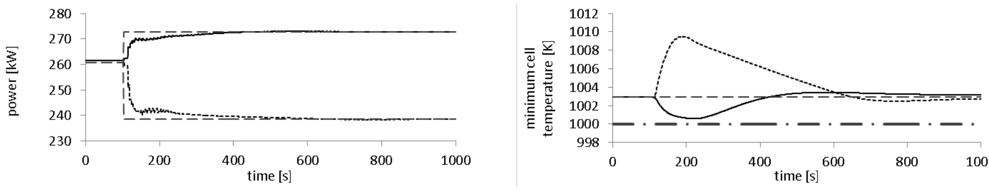

(a) power (W)

(b) minimum cell temperature (K)

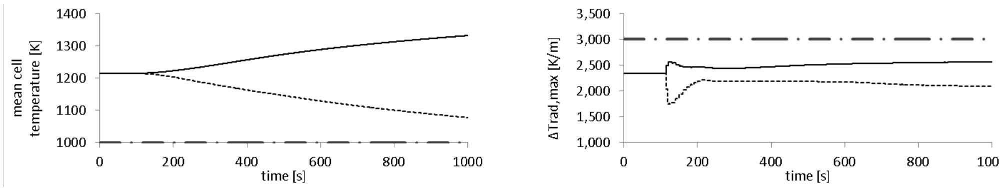

(c) average cell temperature (K)

(d) $\Delta T_{rad,max}$ (K/m)

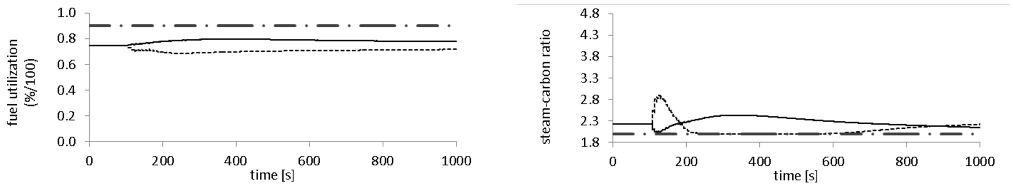

(e) fuel utilization (%/100)

(f) steam-to-carbon ratio

Figure 5.6: Closed-loop load and minimum cell temperature tracking

travels 30 to 60°C from the initial value as seen in Figure 5.7; the SCR also violates its lower limit since it is now unconstrained. Successful mean cell temperature tracking is demonstrated in Figure 5.7(c). The maximum radial thermal gradient increases by approximately 500 K/m although the mean cell temperature is constant as seen in Figure 5.7(d). The plots demonstrate that controlling the average cell temperature, or outlet gas temperature, is not an effective means to controlling the two critical thermal stress drivers in the tubular SOFC. However, constrained control provides very effective reliability control while adjusting MVs in an efficient manner - considering multivariable interactions and using MVs only as necessary to satisfy constraints, not unnecessary tracking.

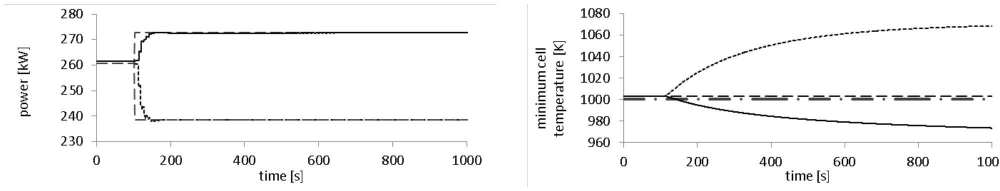

(a) power (W)

(b) minimum cell temperature (K)

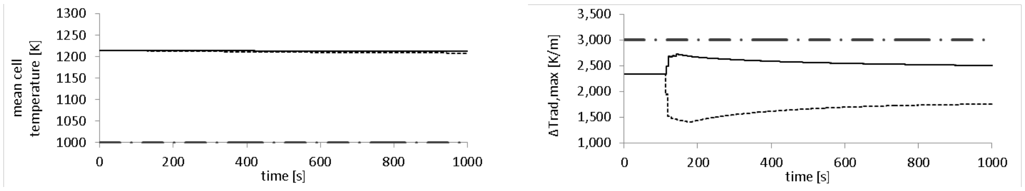

(c) average cell temperature (K)

(d) $\Delta T_{rad,max}$ (K/m)

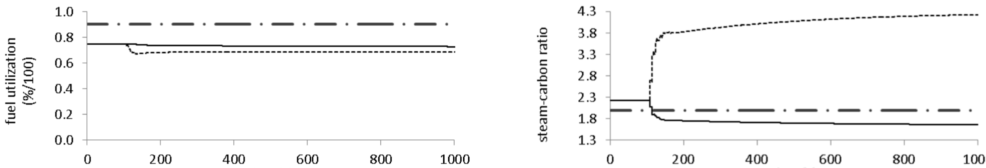

(e) fuel utilization (%/100)

(f) steam-to-carbon ratio

Figure 5.7: Closed-loop load and average cell temperature tracking

As shown in Figure 5.8, the outlet gas temperature tracking produces nearly identical results to the average cell temperature tracking. In both cases the steam-to-carbon ratio and minimum cell temperature significantly violate the limits. Further plots of the outlet gas temperature results would be redundant since they nearly replicate the average cell temperature results. Using either of these as the reliability CV does not control the actual reliability CVs for the tubular SOFC, the minimum cell temperature or maximum radial thermal gradient.

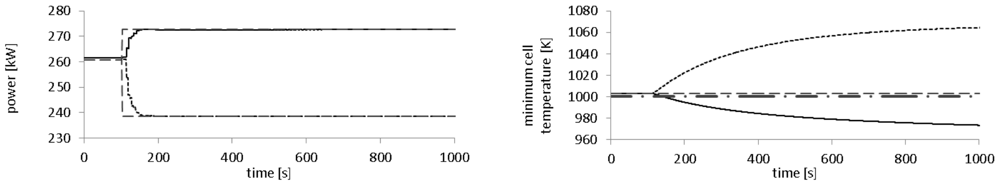

(a) power (W)

(b) minimum cell temperature (K)

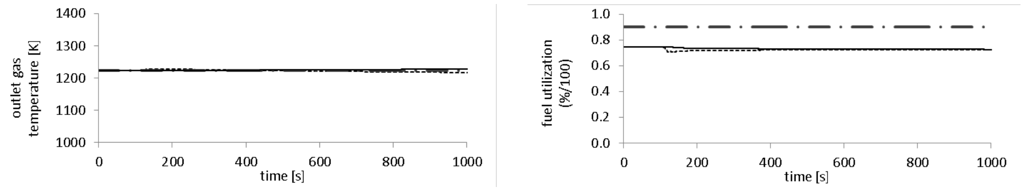

(c) outlet gas temperature (K)

(d) fuel utilization (%/100)

Figure 5.8: Closed-loop load and outlet gas temperature tracking

Table 5.2: Integrated absolute error for setpoint tracking with disturbances

Control case	Tracking variables	Disturbance model	Power IAE	$T_{cell,min}$ IAE
(1)	Power	none	4315	76 319
(2)	Power, $T_{cell,min}$	none	5808	8667
(3)	Power, $T_{cell,min}$	included	4017	13 368

5.2.4 Disturbance Rejection

The proposed model and MPC algorithm are tested for disturbance rejection capability with a sinusoidal fuel quality disturbance characterized by varying CH_4 and CO_2 concentrations as shown in Figure 4.19. Three unique simulation cases are studied and the integrated absolute error (IAE) is compared in Table 5.2.

The controller with modeled disturbances succeeds at having the lowest IAE for load-following while including the minimum cell temperature as a tracking variable. All three cases have matching MPC tuning parameters – load tracking is weighted an order of magnitude larger than temperature tracking. The closed-loop controlled variable response with disturbances is shown for case 3 in Figure 5.9. As the methane concentration reaches a minimum value near 700 s and 2100 s, the controller ability to maintain load is limited by the U_f, SCR, and $T_{cell,min}$ CV constraints. In addition, three of the four MVs are riding upper or lower limits at various times as shown in Figure 5.10. As the MPC finds optimal operation at MV limits for the inlet fuel temperature, system pressure, and voltage, an important conclusion from the

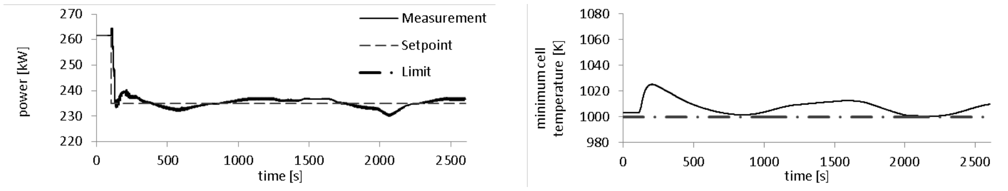

(a) power (W)

(b) minimum cell temperature (K)

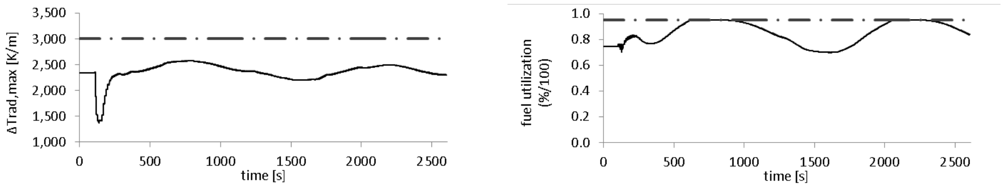

(c) $\Delta T_{rad,max}$ (K/m)

(d) fuel utilization (%/100)

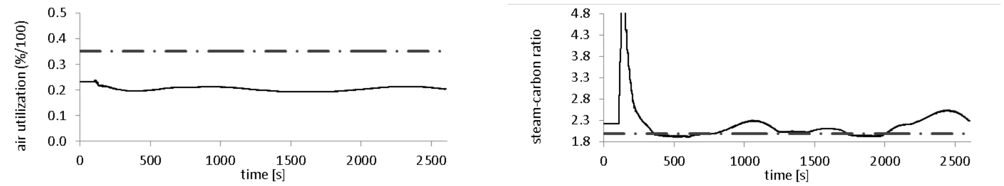

(e) air utilization (%/100)

(f) steam-to-carbon ratio

Figure 5.9: Closed-loop load regulation with measured fuel quality disturbance rejection

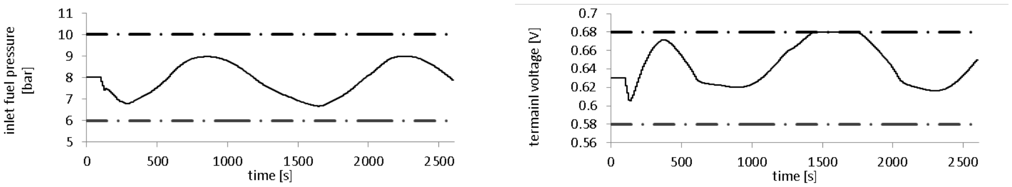

(a) inlet fuel pressure (bar)

(b) terminal voltage (V)

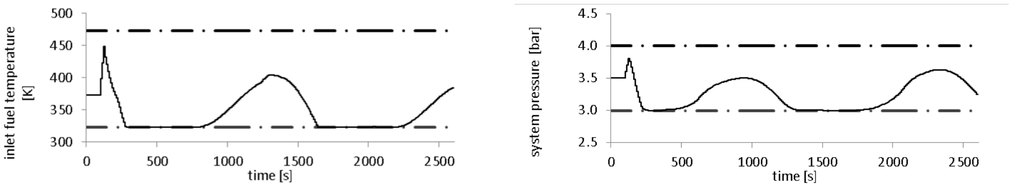

(c) inlet fuel temperature (K)

(d) system pressure (bar)

Figure 5.10: MV profiles during closed-loop load regulation with disturbances

MV plots is that the controller ability to meet operational objectives would be improved by expanding the MV ranges. Having an air compressor that operates at lower pressures would be beneficial while expanding the range of inlet fuel pressure would have little effect in this case. Including closed-loop control studies in the system design process would provide critical insight into the system's capability to meet performance and reliability goals and predict capability to reject disturbances in potential new SOFC applications.

Chapter 6

Economic Optimization

Optimization of the solid oxide fuel cell involves adjusting manipulated variables in order to lead system operation to an optimal state subject to operating constraints, set points, design limitations, and actuator limitations. The optimal state may have various definitions including maximum fuel cell efficiency, minimum total or operational cost. Preexisting control objectives such as load following should still be satisfied.

The design optimization involves finding an optimal combination of design and operational parameters to minimize total system cost. The design parameter chosen here is the number of cells, and the operational parameters are $P_{p,in}$, V_{cell}, $T_{p,in}$, and P_{sys}. The total system cost is composed of annualized capital and operational costs as described in the following section. The optimization solves for optimal values at steady-state. The economic model is described followed by justification for the chosen performance index. The SOFC system as described in Chapter 3, with fuel cell, ejector, and prereformer, is modeled completely within APMonitor and solved as a constraint to the nonlinear programming optimization problem. Design optimization results indicate that optimization provides a cost reduction versus the nominal fuel cell design case while remaining in a safe operating region.

6.1 SOFC Economic Model

An economic model for the SOFC is defined as the annual cost for purchasing and operating the SOFC to produce the desired power output as shown in Equation 6.1:

$$C_{tot} = C_{cap} + C_{op}, \tag{6.1}$$

with the total cost, C_{tot}, capital cost, C_{cap}, and operating cost, C_{op}.

Annual operating cost is defined as the cost of fuel, methane, to operate the SOFC for 8600 h, N_h, as shown in Equation 6.2:

$$C_{op} = c_f \, V_f \, N_h, \tag{6.2}$$

with the specific cost of fuel, c_f $[\$/(m^3\,h)]$, and volumetric flow rate, V_f $[m^3/h]$. The fuel cost is chosen as $0.2\ \$/\left(m^3\,h\right)$ consistent with current prices and Calise [15].

Annualized capital cost is defined as the sum of financing cost, maintenance cost, and insurance cost as shown in Equation 6.3:

$$C_{cap} = C_{fin} + C_{mai} + C_{ins}, \tag{6.3}$$

$$C_{fin} = \frac{C_{pur}\, i\, (1+i)^{N_h}}{(1+i)^{N_h} - 1}, \tag{6.4}$$

$$C_{mai} = \frac{f_{mai}\, C_{pur}}{N_h}, \tag{6.5}$$

$$C_{ins} = \frac{f_{ins}\, C_{pur}}{N_h}. \tag{6.6}$$

The financing cost is calculated based on a ten year payback at a 5% interest rate, i, given the initial purchase cost, C_{pur}. The purchase cost is the sum of the fuel cell, inverter, prereformer, and auxiliary equipment costs as shown in Equation 6.7:

$$C_{pur} = C_{sofc} + C_{inv} + C_{pre} + C_{aux}. \tag{6.7}$$

The cost of the fuel cell is commonly a function of cell number, cell size and operating temperature as shown in Equation 6.8:

$$C_{sofc} = \; n_{cells}\, \pi\, D_{outer} L \; (2.96\, T_{sofc} - 1907)\,, \tag{6.8}$$

with the cell length, L, outer diameter, D_{outer}, and operating temperature, T_{sofc}. The temperature dependency accounts for more costly materials used at higher temperature as proposed by Chen [18]. In particular La Chromite is prescribed by Chen for the interconnects at high temperatures near 1000°C. Since the La Chromite is necessary for the high peak temperatures considered herein, T_{sofc} is set constant to 1000°C. The inverter cost is based upon the maximum required power output, P_{max}, as shown in Equation 6.9:

$$C_{inv} = \; 10^5 \left(n_{cells} \frac{P_{max}}{500} \right)^{0.7}. \tag{6.9}$$

The prereformer and auxiliary costs are shown in Equation 6.10 and 6.11:

$$C_{pre} = \; 130 \left(\frac{A}{0.093} \right)^{0.78} \; + \; 3240\, V_{pr}^{0.4} \; + \; 21280.5\, V_{pr}, \tag{6.10}$$

$$C_{aux} = \; 0.1\, C_{sofc}, \tag{6.11}$$

with the prereformer area, A, and volume, V_{pr}.

The economic model presented herein is based upon a combination of models presented by Calise, Arsalis, and Chen [7, 15, 18]. Costs of taxation and offsets from government incentives are not considered due to their local and transitory nature.

6.2 Optimization Performance Index

The performance index for optimization should be chosen to provide the most economical operation. For the SOFC optimal economic operation

Table 6.1: Maximum fuel cell efficiency versus minimum fuel cost performance indices

	Minimum Fuel Cost	Maximum Efficiency
Power (kW)	267.0	267.0
Efficiency (%)	42.5	43.9
Annual Operating Cost ($)	94 930.67	96 022.90
Fuel Utilization (%)	77.4	82.7
External Fuel Supply (kg/s)	0.009 93	0.010 05
SOFC Inlet Fuel Flow (kg/s)	0.075 07	0.071 57
SOFC Inlet H_2 Molar Flow (mol/s)	0.000 90	0.000 88
SOFC Inlet CH_4 Molar Flow (mol/s)	0.000 065	0.000 047

involves satisfying the power demand with the minimal total cost, i.e., maximizing overall system efficiency while minimizing system size. While system efficiency is generally improved using a high efficiency SOFC prime mover, the system efficiency and fuel cell efficiency move independently and in opposite directions at times. Table 6.1 demonstrates how the maximum fuel cell efficiency and minimum fuel cost cases differ.

The maximum fuel cell efficiency case has a 43.9% efficiency yet consumes 1% more methane than the minimum fuel cost case. The minimum fuel cost case has an efficiency of 42.5%. Examining the fuel flow rates explains the difference in the two cases. The maximum fuel cell efficiency case consumes more methane yet produces the same power with less rich fuel at the fuel cell inlet, thereby explaining the higher efficiency. Note how the SOFC inlet molar flows are lower in the maximum efficiency case.

Although the minimum cost case has lower fuel cell efficiency, the recycled fuel is richer due to lower fuel cell efficiency. Therefore, the minimum cost case requires less pure methane to satisfy the power demand. Internal fuel recycling within the SOFC causes overall system efficiency to move independently from fuel cell efficiency in this scenario. For the tubular SOFC system design optimization, the performance index should be specified as minimum total cost, and for operational optimization, the performance index should equal the minimum fuel cost or maximum system efficiency as follows in Equation 6.12 and 6.13:

$$\min_{\boldsymbol{u(t)}} J = \ C_{tot} \tag{6.12}$$

$$\begin{array}{cccccc} s.t. & g(x,u) & = & 0 & & \\ & u_{min} & \leq & u(k) & \leq & u_{max} \\ & y_{min} & \leq & y(k) & \leq & y_{max} \end{array} , \tag{6.13}$$

where $g(x)$ represents the SOFC system model as presented in Chapter 3 combined with the economic model presented in this chapter, and the MV and CV constraints are same as those used for control. The fuel cell efficiency or fuel utilization are not recommended for use as the performance index if the optimal performance index is desired.

6.3 Results

For an SOFC system capable of load-following, the optimal design must be chosen based upon the expected power demand distribution. An SOFC system optimized at the peak power state may become increasingly sub-optimal as the power demand decreases. This research considers three unique load distributions represented by load probability density functions (PDFs) as shown in Figure 6.1. In two cases, $h_1(x)$ and $h_2(x)$, the system has the highest probability of operating at a power less than peak power, 252 kW and 260 kW respectively. These power demand curves are represented by Weibull PDFs.

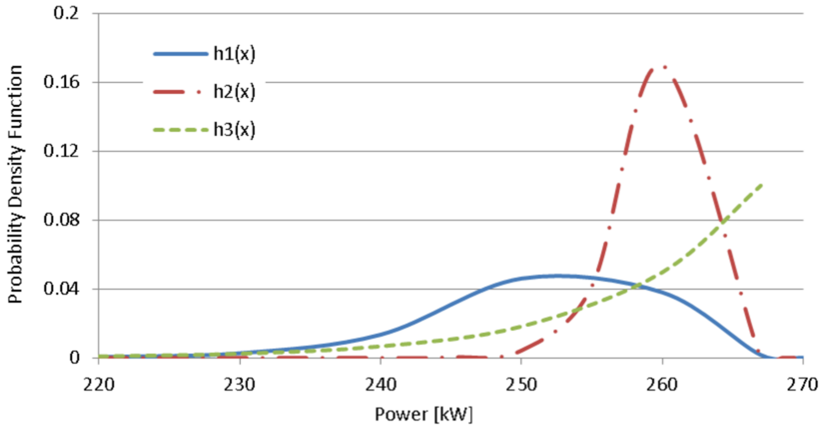

Figure 6.1: Probability density curves for three distinct power demand distributions

The third case, $h_3(x)$, represents a power demand profile with highest probability at peak power and a monotonically decreasing probability of operating at lower power; an exponential distribution is used to represent this PDF. The area under the PDFs has been verified to equal a probability of 100%. Equations for these curves are provided in Equations 6.14 and 6.15:

$$h_{weibull}(x) = \frac{\beta}{\delta}\left(\frac{x}{\delta}\right)^{\beta-1}\exp\left[-\left(\frac{x}{\delta}\right)^{\beta}\right], \tag{6.14}$$

$$h_{exp}(x) = \lambda \exp\left[\lambda\left(x - 267\right)\right], \tag{6.15}$$

where β and δ are parameters for the Weibull distribution, and λ is a parameter for the exponential distribution. β is equal to 40 and 120, and δ is equal to 255 and 260 for $h_1(x)$ and $h_2(x)$ respectively. λ is equal to 0.1.

Several steps are performed in order to find the optimal system design for each power demand curve shown in Figure 6.1:

- A steady-state optimization finds the optimal system design to produce a specified power output, i, for a range of powers i ϵ $[250, 260, 267]$.

- A function, $f_i(x)$, represents the annual total cost of operating each system, i, over a range of powers x $\epsilon\,[220:267]$.
- The product of the power demand PDF and total cost function is integrated over x to calculate the expectation value of cost for design i with a power demand curve j :
  Expected Annual Cost $= E_j\left[f_i(x)\right] = \int_{220}^{267} h_j(x)\cdot f_i(x)\,dx.$

Steady-state optimization found that the optimal number of cells for power outputs of 250, 260, and 267 kW are 1681, 1778, and 1887 cells, respectively. The total annualized cost curves, $f_i(x)$ in Figure 6.2, illustrate costs of operating a fuel cell design at a fixed power output for 8600 h in one year. A fourth curve, default, is plotted to represent the nominal SOFC design without optimization. The plot demonstrates how all optimal designs operate at lower costs than the default design. A quadratic equation is used to model each curve, $f_i(x)$.

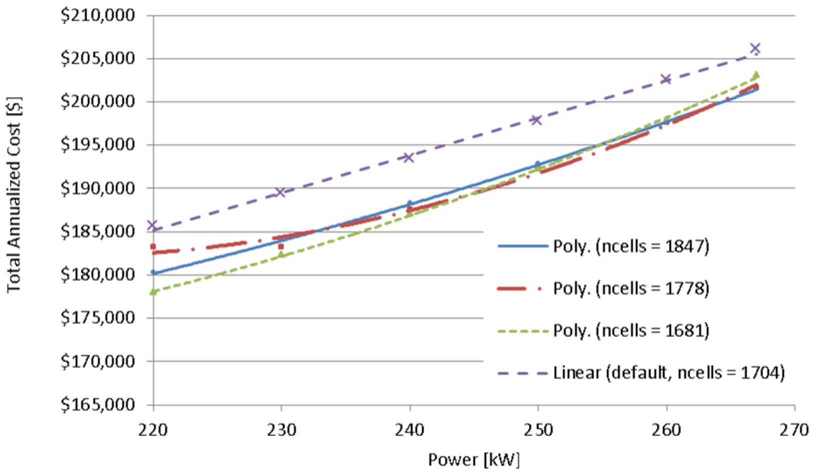

Figure 6.2: Total annualized cost of operating an optimal SOFC design at constant power outputs

Since Figure 6.2 only considers the total operating costs for at a constant power throughout one year, calculating the expected annual cost given the power demand PDF is required to evaluate optimality for a load-following SOFC application. The expected annual cost produces the expectation value of the annual operating cost for each design, i, over each load profile, j. Since the 1778 cell design represents the optimal design for most cases, the total annual operating cost for each case is shown with respect to the 1778 cell design in Figure 6.3: The overall optimal design case, 1778 cells, meets the power demand at an annual cost \$5314 to \$6119 less than the default design. All optimal cases demonstrate annual cost differentials from other optimal cases less than \$1000. The 1681 cell design is more optimal than the 1778 cell design for the $h_3(x)$ load profile by a trivial amount. The cost savings resulting from design optimization become prominent for systems producing higher power outputs since the cost savings scale linearly. For instance, a 26.7

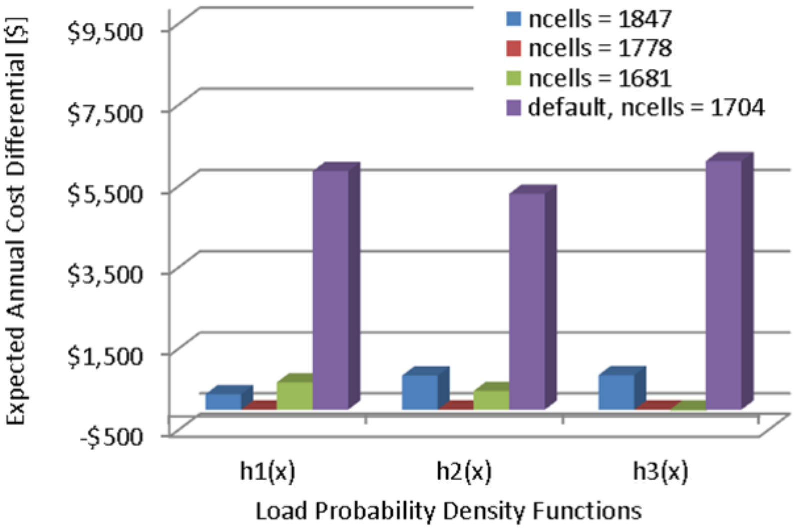

Figure 6.3: Difference from minimum cost for each design and load distribution

MW plant would save \$531,400 annually by implementing the design optimization. In conclusion, the optimization algorithm is successful in producing a 5% reduction in operating costs while ensuring safe operation within operability constraints.

Chapter 7

Summary and Recommendations

7.1 Summary of Contributions

The main focus of this dissertation is to provide new strategies to improve solid oxide fuel cell lifetime and reduce operating costs via advanced control and optimization. While solid oxide fuel cell systems have demonstrated advantages for distributed power generation, the fuel cell lifetime must be increased from the state of the art to make the cost of electricity competitive. The areas of system dynamic analysis and process control play a critical role for increasing lifetime by guaranteeing dynamic operation within operability constraints using constrained control. In particular, thermomechanical stress is a primary predictor for SOFC risk of failure due to crack formation. No significant work can be found in literature that investigates the dynamic response of operability constraints based upon thermomechanical finite element analysis of the electrode electrolyte assembly (EEA). Rather, most works choose different operability constraints, such as the lumped cell temperature, outlet gas temperature, or axial temperature distribution, without justification for these constraints based on mechanical stress and risk analysis. This work builds upon existing steady-state analysis to investigate the dynamic response of contributors to SOFC degradation [30, 65], presents a novel constrained, predictive MIMO controller to ensure operability constraint satisfaction, and identifies means to reduce system costs while satisfying constraints using a detailed optimization model.

7.1.1 Dynamic Modeling of Contributions to Thermal Stress

Thermomechanical stress analysis indicates that the primary contributors to thermal-stress induced cracking within the tubular SOFC are local low EEA temperatures and negative radial thermal gradients [30, 65]. The zer0-stress state of the high-temperature tubular SOFC occurs at a high sintering temperature of 1250°C and is set during fabrication. Low EEA temperatures occur locally especially at the active catalytic sites for steam reformation near the fuel inlet. Negative radial thermal gradients occur as the outer chamber gas, fuel in this case, enters at a lower temperature than the inner chamber gas, air.

This work investigates the dynamic response of the minimum cell temperature and maximum negative radial thermal gradient to changes in manipulated variables, fuel inlet pressure, fuel inlet temperature, system pressure, and cell voltage. In addition, the dynamic responses of other causes of fuel cell degradation, the steam-to-carbon ratio, fuel utilization, and air utilization, are investigated. These five controlled variables comprise the set of operability constraints. The dynamic responses demonstrate multivariable interactions, numerator dynamics, and nonlinearities and suggest appropriate control structures.

Steady-state analysis demonstrates the effect of radiation on temperature and concentration profiles for the tubular SOFC. Dynamic analysis reveals that the fuel pressure and fuel temperature are the most effective MVs for load-following. The staircase results for thermal gradient dynamics indicates numerator dynamics particularly in response to the load-following MVs; thus, the thermal gradient should be considered on the same time scale as power output control. Plots of cell temperature versus time and axial location indicate that local temperatures respond differently to the MVs. The fuel pressure significantly affects the inlet cell temperature while air temperature has a greater effect on the center cell temperature. Thus, a control model based on distributed parameters is necessary to control the dynamics of thermal stress drivers, the minimum cell temperature and maximum radial thermal gradient. The local temperature results also have implications for placement of thermocouples for feedback control.

7.1.2 Constrained Predictive MIMO Control of the Tubular SOFC

Dynamic analysis confirms the need to incorporate the operability constraints, particularly thermal constraints, into the control structure. All operability constraint variables show noticeable changes in magnitude simultaneously with changes in power. Constrained control is an ideal solution for this control problem because the number of CVs outnumber the MVs, six to five, and most CVs can move freely within constraints without inducing fuel cell degradation. MIMO control is necessary to account for multivariable interactions, and model-based predictive control enables the controller to consider short and long time constants for mass transport and thermal phenomena respectively by use of varying objective function penalties along the prediction horizon.

Model-based control simulations demonstrate successful load-following in the presence of multiple active MV and CV constraints. Operability variables approach constraints during dynamic load-following without noticeable overshoot past limits. Incorporating the minimum cell temperature as a tracked CV within the MIMO control structure demonstrates improved control over simple load-following. The controller accommodates the power setpoint while preparing in advance for the slow thermal inertia. Simulation studies also use operability CVs chosen in literature, average cell temperature and outlet gas temperature, for comparison with CVs chosen herein. Results indicate that these CVs chosen in other literature do not restrict excursions of thermal stress drivers, the minimum cell temperature or maximum radial thermal gradient. Disturbance rejection is important to permit applications with varying fuel purity. Disturbance feedback measurements are incorporated into the model-based controller, and the controller successfully rejects disturbances while tracking the power setpoint.

7.1.3 SOFC Optimization Subject to Operability Constraints

SOFC design optimization seeks the optimal combination of steady-state design factors and operational states to minimize system cost. Optimization-level models often neglect operability constraints, particularly thermal constraints, as included in this work. However, the accuracy of optimization results is dependent on operational feasibility; an optimal state without considering the minimum cell temperature for the tubular SOFC is a suboptimal state that may not meet lifetime assumptions. In addition, optimization is often performed to satisfy a specified power load. For load-following applications, the load probability distribution should be considered to find the optimal system.

This work incorporates the two-dimensional SOFC model, along with the prereformer and ejector, as a constraint on the optimization problem; this combined model is the same model used as the physical plant model in dynamic simulations. The optimization problem thereby includes an accurate representation of the five operational constraints. Several load probability density functions are chosen to compare suboptimal designs. Results indicate the potential for reducing annual system costs by implementing optimal design on the SOFC system while satisfying true operational constraints. Optimization cost savings are due primarily to optimal operation versus number of cells, and savings due to optimization are approximately 5% of operational costs.

7.2 Recommendations for Future Work

7.2.1 Inferential Control of Operability Constraints

All operability variables may not be available for direct measurement. Instead, measurement of other variables, such as pressures and temperatures, may be used to estimate the value of the operability variables using state estimation. Incorporating these estimated variables as CVs produces inferential control. Radial thermal gradients are a likely candidate for inferential control since thermocouple diameters are commonly in the same range as the EEA thickness. Future work should investigate techniques for estimating the radial thermal gradient and other CVs as necessary and incorporating the estimation algorithms into the control structure.

7.2.2 Fault Detection Based on Distributed Parameter Modeling

Fault detection algorithms will be important for protecting the SOFC from unexpected situations that produce cell degradation. As the constrained control simulations indicate operation at multiple CV limits, failure of one actuator or sensor is likely to cause excursions past operability constraints. Even temporary excursions present risk of crack propagation in the ceramic EEA. Candidates for fault detection are valve stiction, sensor failure or miscalibration, and drift faults such as fuel cell wear and catalytic inactivity. The distributed parameter model ensures accurate predictions of local and outlet temperatures necessary for model-based fault detection.

7.2.3 Application to GT-SOFC Hybrid Systems

Gas turbine-solid oxide fuel cell hybrid systems present the opportunity for improved efficiencies reaching 70%. The GT-SOFC is a highly interacting system with additional operability constraints than the SOFC. The hybrid system presents more CVs for control than the SOFC, and these CVs, such as surge margin and turbine inlet temperature, should be controlled with constraints. Multivariable interactions are increased with the GT-SOFC system due to the coupled thermal and mass transport, and additional nonlinearities are introduced, particularly in compressor operation. The need for a constrained, predictive MIMO controller is apparent for a GT-SOFC, and the control algorithm demonstrated in this work is a promising foundation for GT-SOFC control.

Appendices

Appendix A

Mathematical Derivations

MISO Transfer Function to State-Space Conversion

The initial MISO model is fit as a transfer function model as shown in Equation A.1:

$$Y(s) \;=\; \left[\tfrac{K_1(\tau_a\, s+1)}{(\tau_1\, s+1)(\tau_2\, s+1)} \quad \ldots \quad \tfrac{K_{n_u}(\tau_{n_u}\, s+1)}{(\tau_1\, s+1)(\tau_2\, s+1)}\right] \begin{bmatrix} U_1(s) \\ \vdots \\ U_{n_u}(s) \end{bmatrix}. \tag{A.1}$$

The state-space model may be derived as shown in the following.

1. Factor a common denominator:

$$Y(s) \;=\; \tfrac{1}{(\tau_1\, s+1)} \left[\tfrac{K_1(\tau_a\, s+1)}{(\tau_2\, s+1)} \quad \ldots \quad \tfrac{K_{n_u}(\tau_{n_u}\, s+1)}{(\tau_2\, s+1)}\right] \begin{bmatrix} U_1(s) \\ \vdots \\ U_{n_u}(s) \end{bmatrix}. \tag{A.2}$$

2. Introduce the state variables, x_i:

$$X_i(s) \;=\; \tfrac{U_i(s)}{\tau_i\, s+1}, \tag{A.3}$$

$$\tau_i\, \dot{x}_i + x_i \;=\; u_i, \tag{A.4}$$

$$\dot{x}_i \;=\; -\tfrac{1}{\tau_i}\, x_i + \tfrac{1}{\tau_i}\, u_i. \tag{A.5}$$

3. Update the process model by substituting X_i and apply the inverse Laplace transform:

$$Y(s) \;=\; \tfrac{1}{(\tau_1\, s+1)} \left[K_1\, (\tau_a\, s+1)\, X_i(s) \quad \ldots \quad K_{n_u}\, (\tau_{n_u}\, s+1)\, X_{n_u}(s)\right], \tag{A.6}$$

$$\tau_1\, \dot{y} + y \;=\; \left[K_1\, (\tau_a\, \dot{x}_1 + x_1) \quad + \ldots + \quad K_{n_u}\, (\tau_{n_u}\, \dot{x_{n_u}} + x_{n_u})\right]. \tag{A.7}$$

4. Substitute the expressions for x from Equation A.5 and assign y as the final state variable, x_{n_u+1}, to convert the model to state-space form:

$$\dot{\boldsymbol{x}} = A\,\boldsymbol{x} + B\,\boldsymbol{u}. \tag{A.8}$$

Appendix B

SOFC Model Equations

Material Balance

$$\dot{N}_{i,out} = \dot{N}_{i,in} + \sum_{j=1}^{3} v_i \, r_j \quad [mol \, s^{-1}] \tag{B.1}$$

$$r_{CH_4} = A \exp\left(-\frac{E_a}{R\,T}\right) p_{CH_4} \quad [mol \, m^{-1} \, s^{-1}] \tag{B.2}$$

$$\begin{aligned} A &= 4,274 \quad [\tfrac{mol}{m^2 \, bar \, s}] \\ E_a &= 82 \quad [\tfrac{kJ}{mol}] \end{aligned} \tag{B.3}$$

$$r_{shift} = k \left(X_{H_2O} \, X_{CO} \; - \; \frac{X_{H_2} \, X_{CO_2}}{K_{eq}} \right) \quad [mol \, m^{-3} \, s^{-1}] \tag{B.4}$$

$$\begin{aligned} K_{eq} &= \exp\left(-0.2935\,\zeta^3 + 0.635\,\zeta^2 + 4.1788\,\zeta + 0.3169\right) \\ \zeta &= \tfrac{1000}{T} - 1 \end{aligned} \tag{B.5}$$

$$r_{anode} = \frac{v_a \, I}{2F} \tag{B.6}$$

$$r_{cathode} = \frac{v_c \, I}{4F} \tag{B.7}$$

Electrical Model

$$\begin{aligned} V_{oc} &= V^0_{H_2} + \tfrac{R\,T}{2\,F}\,\ln\left(\tfrac{p_{H2}\,p^{0.5}_{O_2}}{p_{H_2O}}\right) \\ V^0_{H_2} &= -\tfrac{\Delta G_0}{2\,F} + \tfrac{\Delta S_0}{2\,F}\,(T - 298) \end{aligned} \tag{B.8}$$

$$V_{cell} = V_{oc} - \eta_{act} - \eta_{conc} - \eta_{ohm} \tag{B.9}$$

$$\eta_{ohm} = I\,R_{ohm} \tag{B.10}$$

$$\eta_{act} = \eta_{act,a} + \eta_{act,c} \tag{B.11}$$

$$\eta_{act,a} = \frac{R\,T\,i}{2\,F\,i_0} \tag{B.12}$$

$$\eta_{act,c} = \frac{R\,T\,i}{4\,F\,i_0}. \tag{B.13}$$

$$\begin{aligned} i_{0,an} &= \gamma_{an}\,\left(\tfrac{p_{H_2}}{p_{amb}}\right)\,\left(\tfrac{p_{H_2}O}{p_{amb}}\right)^m\,\exp\left(-\tfrac{E_{act,an}}{RT}\right)\,A/m^2, \\ i_{0,cat} &= \gamma_{cat}\,\left(\tfrac{p_{O_2}}{p_{amb}}\right)^{0.25}\,\exp\left(-\tfrac{E_{act,an}}{RT}\right)\,A/m^2, \end{aligned} \tag{B.14}$$

$$\begin{aligned} \eta_{conc} &= \eta_{conc,an} + \eta_{conc,cat} \\ &= \tfrac{R\,T}{2\,F}\,\ln\left(\frac{X^b_{H_2}\,X^r_{H_2O}}{X^r_{H_2}\,X^b_{H_2O}}\right) + \tfrac{R\,T}{4\,F}\,\ln\left(\frac{X^b_{O_2}}{X^r_{O_2}}\right), \end{aligned} \tag{B.15}$$

$$R_i = \frac{\rho_i\,\delta_i}{A_i} \tag{B.16}$$

Table B.1: Electrical Constants

γ_{an}	$7(10^9)$
γ_{cat}	$7(10^9)$
ΔG_0	$-228.61(10^3)$ [J/mol]
ΔS_0	-44.34 [J/(mol K)]
m	1
$E_{act,an}$	$1(10^5)$ [J/mol]
$E_{act,cat}$	$1.2(10^5)$ [J/mol]

$$\begin{aligned}
R_{tc} &= 0.55, \\
R_I &= \tfrac{\rho_I\,\delta_I}{A_I} + \tfrac{0.5\rho_C\,thk_C}{A_I} \\
R_E &= \tfrac{\rho_E\,\delta_E}{A_E} + \tfrac{0.5\rho_C\,thk_C}{A_E} + 0.5\tfrac{\rho_A\,thk_A}{A_E} \\
R_C &= \tfrac{\rho_C\,\delta_C}{A_C} \\
R_1 &= \tfrac{(R_C+R_E)(R_E+R_A)}{R_C+2R_E+R_A} \\
R_2 &= \tfrac{(R_C+R_1)(R_E+2R_A)}{R_C+R_1+R_E+2R_A} \\
R_3 &= \tfrac{(R_E+3R_A)(R_C+R_2)}{R_E+R_2+R_C+3R_A} \\
R_{ohm} &= \tfrac{(R_C+R_3)(1+R_{tc})}{2+R_I}
\end{aligned} \tag{B.17}$$

Energy Balance

$$
\begin{aligned}
&\dot{N}\, MW\, c_p\, T_g|_{i,out} \; = \\
&\qquad \dot{N}\, MW\, c_p\, T_g|_{i,in} \; + \; \sum_j h_j\, A_j\, \left(T_{s,surf_{ij}} \; - \; T_{g_i}\right) \; - \; \sum_k \Delta H_{ik}\, r_{ik}
\end{aligned}
\qquad \text{(B.18)}
$$

$$
Q_{cond,ij} \; = \; \frac{k\, A}{\Delta r}\, \left(T_{s,surf_{ij}} \; - \; T_{s_{ij}}\right) \qquad \text{(B.19)}
$$

$$
\begin{aligned}
MW &= \sum_i MW_i\, X_i \\
X_i &= \tfrac{\dot{N}_i}{\dot{N}}
\end{aligned}
\qquad \text{(B.20)}
$$

$$
\frac{c_{p,ig}}{R} \; = \; \alpha \; + \; \beta\, T \; + \; \gamma\, T^2 \; + \; \frac{\varsigma}{T^2} \qquad \text{(B.21)}
$$

$$
\rho\, V\, c_{p,i}\, \frac{dT_{a,i}}{dt} \; = \; h\, A\, (T_{ga_i} \; - \; T_{a,surf,i}) \; + \; k\, A\, \frac{dT_{a,i}}{dx} \; + \; k\, A\, \frac{dT_{a,i}}{dr} \qquad \text{(B.22)}
$$

$$
\rho\, V\, c_{p,i}\, \frac{dT_{e,i}}{dt} \; = \; k\, A\, \frac{dT_{e,i}}{dx} \; + \; k\, A\, \frac{dT_{e,i}}{dr} \; + \; \dot{Q}_{elec}, \qquad \text{(B.23)}
$$

$$
\begin{aligned}
&\rho\, V\, c_{p,i}\, \frac{dT_{c,i}}{dt} \; = \\
&\quad h\, A\, (T_{gc_i} \; - \; T_{c,surf,i}) \; + \; k\, A\, \frac{dT_{c,i}}{dx} \; + \; k\, A\, \frac{dT_{c,i}}{dr} \; + \; \varepsilon\, F_i\, \sigma\, A\, \left(T_{tube}^4 \; - \; T_c^4\right)|_i
\end{aligned}
\qquad \text{(B.24)}
$$

$$
\begin{aligned}
\rho\, V\, c_{p,i}\, \frac{dT_{tube,i}}{dt} \; = \; & h\, A\, (T_{gc_i} - T_{tube,surf,i}) \; + \; h\, A\, (T_{gc2_i} - T_{tube,surf2,i}) \\
& + \; k\, A\, \frac{dT_{tube,i}}{dx} \; + \; \varepsilon\, F_i\, \sigma\, A\, \left(T_c^4 \; - \; T_{tube}^4\right)|_i
\end{aligned}
\qquad \text{(B.25)}
$$

$$\dot{Q}_{elec} = \left(\frac{\Delta H_{f,H_2O(g)}}{n\,F} - V_{cell} \right) \cdot i, \tag{B.26}$$

Table B.2: Heat Transfer Constants

F_{outer}	0.46
F_{inner}	1
ε	0.8
$N_{u,ga}$	4.2
$N_{u,gc}$	5.5
$N_{u,tube}$	11
k_{ga}	$176(10)^{-3}$ [W/(m K)]
k_{gc}	$51.5(10)^{-3}$ [W/(m K)]

Appendix C

Gas Turbine Model

C.1 Modeling

C.1.1 Overview

The gas turbine system must be modeled with sufficient detail for the reasons provided in the following:

- to provide a system plant with accurate dynamics that will be used in lieu of an experimental system for closed-loop control studies;
- to include fundamental properties, i.e. temperatures and pressures, necessary for including operating constraints directly into the optimization problem - constraints include compressor surge margin, combustor and fuel cell fuel utilization, pressure and temperature gradients, and flow direction; and
- to benefit from advanced control and optimization techniques which have become available for real-time control applications with state-of-the-art computational resources.

With this aim, conservation laws for mass, momentum, composition, and energy and transport equations are used in combination with experimental equations to produce a modular and nonlinear differential and algebraic equation (DAE) model. Dynamic states include gas dynamics for pressure and mass flow, gas temperatures and compositions, and equipment material temperatures. The model requires algebraic equations to incorporate thermodynamics, reaction equations, electrical performance, steady-state assumptions, and turbomachinery map interpolation equations.

The governing physical-mathematical equations for all components are derived from unsteady, one-dimensional Euler's equations as shown in Equation C.1.

$$\begin{array}{rcl} \frac{\delta(S\rho)}{\delta t}+\frac{\delta(S\rho u)}{\delta x} & = & 0 \\ \frac{\delta(S\rho u)}{\delta t}+\frac{\delta S\left(\rho u^2+P\right)}{\delta x} & = & \sum F_i \\ \frac{\delta(SE)}{\delta t}+\frac{\delta S(E+P)u}{\delta x} & = & \dot{Q}_{gen}+\dot{Q}_{loss} \\ \frac{\delta(S\rho Y_i)}{\delta t}+\frac{\delta(S\rho Y_i u)}{\delta x} & = & \dot{m}_{i,gen} \end{array} \tag{C.1}$$

in which $S, \rho, u, P, F_i, E, Q_{gen}, Q_{loss}, Y_i$, and $m_{i,gen}$ are the area normal to flow, gas density, gas velocity, pressure, momentum frictional losses, heat generated, environmental heat loss, gas component mass fraction, and chemical reaction mass generation terms. Key simplifying assumptions used throughout much of the GT-SOFC model are ideal gas, constant heat capacity, constant area, lumped equipment temperatures, and spatially-discretized one-dimensional transport. Additional assumptions are deemed reasonable for the time step of interest with this research, approximately 1 second, to improve computational robustness and reduce model stiffness; these assumptions include a lumped combustor model, steady-state combustion pressure equations, steady-state fuel cell electrical properties, and an increased time constant for turbomachinery gas dynamics.

The DAE models for each component are spatially discretized as a lumped model or in one dimension and are incorporated as model functions within MATLAB and Simulink. Each GT-SOFC component is modeled separately in a modular approach, and the components are linked via input and output nodes. A state flow diagram for the completed gas turbine model is shown in Figure C.1 in which p_{atm}, T_{atm}, N, A_{IBV} and MR represent atmospheric pressure and temperature, shaft speed, area of the inlet butterfly valve (or IGV angle), and combusted air mass flow percent, respectively. The latter variable is the percent of compressor air that passes through the combustor; the remainder is bypassed around the combustor and mixes with the combustor exit flow. This gas turbine model is designed for variable speed operation and is only one of the turbine variations; modeling of the SOFC is remaining work. The system model is numerically integrated in a simultaneous and robust manner for stiff equations using a built-in variable order, multi-step solver that optionally uses a backwards difference formula.

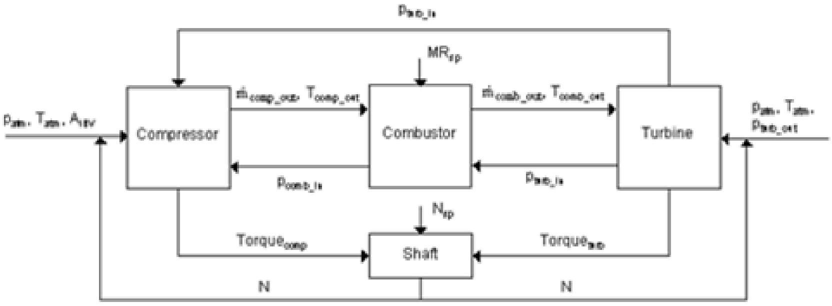

Figure C.1: The state flow diagram illustrates internal and external data exchange between gas turbine component models.

C.1.2 Model Details

The compressor and gas turbine are modeled via a combination of conservation equations, experimental performance maps, and thermodynamic equations. The continuity equation provides the differential equation for pressure and is spatially discretized using backward differences; the momentum equation provides the dynamic mass flow equation and is discretized using forward differences. Discretization is performed in this manner to ensure convergence to a unique solution.

Gas turbine turbomachinery quasi-steady-state performance maps are used according with common practice to provide the relationship between pressure ratio versus mass flow and isentropic efficiency versus mass flow at varying shaft speeds. Mass flows and shaft speeds displayed on the performance maps are corrected versus ambient conditions. The corrected mass flow is fitted as a log function of the pressure ratio with coefficients as an exponential function of speed. Maps may be scaled as necessary to provide sufficient mass flow and pressure ratio for the power demand. The turbomachinery models used in this research are based on centrifugal, single-stage compressor and turbine performance maps from the Garrett 4508R turbocharger.

Thermodynamic relationships model the relationship between temperature and pressure change during compression and expansion, and an isentropic process is assumed with constant heat capacity. Torque is calculated by performing a first-law energy balance relating shaft work to internal energy changes within the gas.

The combustor is modeled as a lumped well-stirred tank reactor, and gas dynamics are modeled as steady-state given that concentration changes govern the system time constant. Combustion reactions are modeled using a two-step Westbrook-Dryer model for methane combustion and the reversible carbon monoxide-carbon dioxide reaction. The dynamics of the following seven species are modeled to interface with the SOFC: methane, carbon monoxide, carbon dioxide, hydrogen, water, nitrogen, and oxygen.

Modeling of the compressor, combustor, and turbine using governing equations permits the calculation of critical reliability parameters, namely surge margin, fuel utilization, turbine inlet temperature, and emissions, which may be used as controlled variables within closed-loop control. Manipulated variables will varying depending on the turbomachinery configuration and may include inlet guide vane area, fuel mass flow, variable guide vane area, and shaft speed depending on the chosen configurations.

C.2 Results

The variable speed gas turbine with motoring alternator configuration has been simulated to demonstrate gas turbine performance. Results from the simulations confirm that the model is representative of a gas turbine with the specified size and configuration. These results are useful for observing the feasible operating range and optimal operating conditions prior to incorporation into the hybrid system.

The efficiency and power output of the gas turbine increase monotonically with the turbine inlet temperature as expected. Surge margin decreases below zero as the shaft speed is increased at high combustor air mass flows near forty percent as seen in Figure C.2. The operating region that exceeds the temperature limit of 1350 K and surge margin limit of zero percent is shown in crosshatching. The maximum operating efficiency is achieved at the maximum speed of 100,005 rpm when the combustor air percent is above fifteen percent. Within this region the surge margin is below eight percent and decreases with increasing combustor air percent. The plots illustrate how the system states will reside along their constraints when efficiency is maximized. Total turbine mass flow increases monotonically with increasing speed but decreases as a larger portion of compressor airflow is used in combustion. This result is intuitive since less mass flow is needed to maintain a given speed when the gas temperature is higher. With this configuration variable speed is necessary to span the full region of possible mass flows.

Dynamic simulation is performed with 10000 rpm step changes occur-

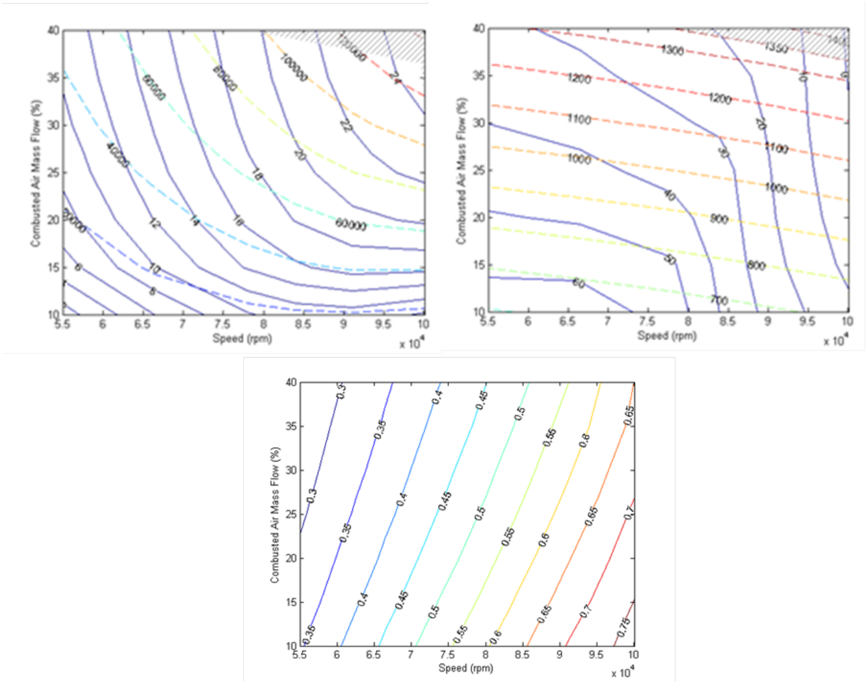

Figure C.2: Gas turbine performance is shown as shaft speed and combusted air mass flow percentage are varied; the operating region that exceeds limits is crosshatched.

ring at sixty second intervals. Following the set point change the shaft speed settles within two seconds, and gas dynamic properties, temperature and pressure, have an equivalent settling time as shown in Figure C.3. Turbine casing temperature has the longest settling time at ten seconds.

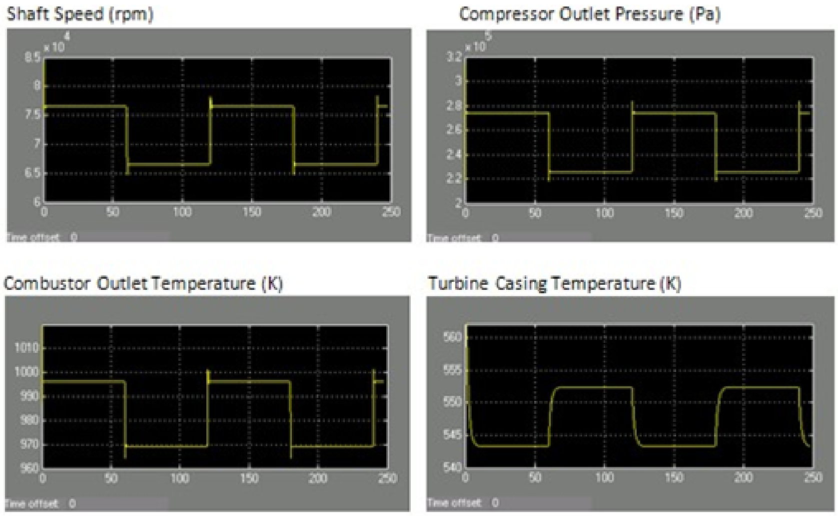

Shaft Speed (rpm)

Compressor Outlet Pressure (Pa)

Combustor Outlet Temperature (K)

Turbine Casing Temperature (K)

Figure C.3: Dynamic responses due to shaft speed set point step changes of 10000 rpm at 60 second intervals.

Appendix D

Indirect Internal Reformer Model

Contributed by Zack Doran, Undergraduate Research Assistant.

D.1 Overview

Fuel cells are currently attracting large interests for their increased efficiency over traditional power plants and near commercial viability. The potential benefits of fuel cells are high due to their direct conversion of chemical energy into electrical energy in combination with low emissions. Solid oxide fuel cells use a solid ceramic inorganic oxide as the electrolyte, typically zirconia, rather than a liquid electrolyte, and require operation at elevated temperatures, typically between 750 - 1000°C. SOFCs generally process a mixture of hydrogen and carbon monoxide formed by internal reformation.

Process Flow

A stream of high purity, desulfurized natural gas is fed to the front-end of the SOFC, first passing through an injector to increase the velocity of the gas. The high velocity natural gas is then reacted over a pre-reformer to crack long-chain hydrocarbons, potentially followed by an indirect internal reformer (IIR), to produce a high yield stream of hydrogen gas, which is used to electrochemically fuel the SOFC on the anode side. Hydrogen is passed over the anode with air or oxygen being passed over the cathode to undergo redox reactions and produce electrical current.

Indirect Internal Reformer

The focus of this report is on the IIR component of the SOFC. The IIR takes a mixture of pre-reformed methane, hydrogen, carbon monoxide, carbon dioxide, and steam and further reforms methane to produce hydrogen and carbon dioxide. Methane undergoes the well-known methane reformation and gas shift reactions in the IIR as shown.

$$\begin{aligned} CH_4 + H_2O &\quad \xleftrightarrow{r_{CH_4}} \quad CO + 3\,H_2 \\ CO + H_2O &\quad \xleftrightarrow{r_{shift}} \quad CO_2 + H_2 \end{aligned} \tag{D.1}$$

The remainder of the methane exiting the IIR is reformed directly at the anode. The intention of reforming upstream of the SOFC is to prevent the latter from strong local temperature drops and high thermal stresses originating from the endothermic reforming reaction.

Model Overview

The IIR was modeled as a set of ten continuously-stirred tank reactors in series, such that the model could be discretized along the length of the IIR. Since the reformation reaction is endothermic, the IIR requires heat from the SOFC to drive the methane reformation reactions. Radiation heat transport occurs from the fuel cell to the IIR walls, which are located directionally in front of the fuel cell. Radiation heating effects were modeled via the Stefan-Boltzman law.

$$Q_{rad} = \varepsilon\,\sigma\,\left(T_w^4 - T_i^4\right) \tag{D.2}$$

In equation D.2, P is power (Watts), e is emissivity, σ is the Stefan-Boltzmann constant, T is the temperature of the wall of the IIR (Kelvin), and T_i is the temperature of CSTR at location i in the series. A constant wall temperature of 1200K was assumed for the SOFC operating temperature. The outside and inside temperatures of the walls were assumed equal because of the small thickness compared to the length and metallic material of the walls. The entrance and exit of the IIR are adiabatic. The reformer was modeled with tubular design and simulated as plug flow.

Assumptions

Mass flow was assumed constant and pressure drop was neglected through the IIR. The model is only discretized in the length direction. Kinetic rate-based, volumetric equilibrium equations were used to model reactions in the reformer. Convective heat transfer was neglected outside the reformer. Specific heat capacities of each component are based on temperature dependent relations. Steady-state behavior of the IIR was modeled to integrate with the steady-state pre-reformer. It is important to note at this point that dynamic behavior of the IIR will strongly depend on the amount of heat inertia and thus thickness and material properties of the wall.

Distributed vs. Lumped Model

An important system characteristic is the modeling domain. System design can vary, but two common methods include distributed and lumped system approach. A lumped system is one in which the dependent variables of interest have no spatial variation. A distributed system is one in which all dependent variables are functions of one or more spatial variables. A distributed approach was taken for design of the IIR because of increased accuracy over a lumped system. This reformer is designed as a discrete-time system, where the next state of this system is solved from the inputs of the previous state and an initial guess. The advantage of a lumped approximation is that it reduces computation costs by solving non-linear and ODE equations at fewer points, rather than a full solver. However, the computational costs for the distributed model are relatively low for the IIR compared to the SOFC system.

D.2 Results

Emissivity Sensitivity Analysis

This model does not have a distributed radiation profile on the IIR walls; however, since the emissivity of the SOFC may not be known accurately, it is important to quantify the effects of emissivity. Figure D.1 illustrates the effects of changing wall emissivity from 0.4 - 1.0 (ideal radiation emitter).

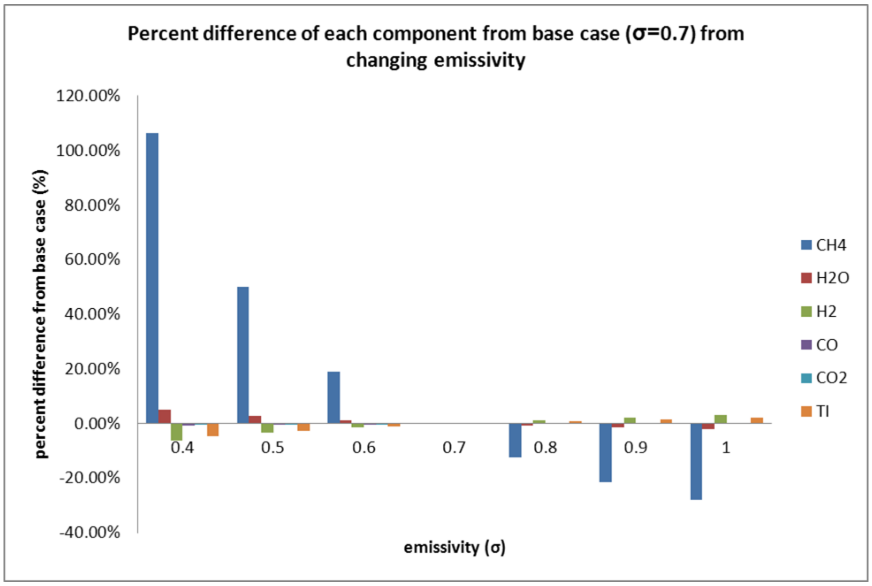

Figure D.1: The sensitivity effects of changing emissivity of the SOFC and measuring change in molar gas molar flow rate and temperature.

Results of the sensitivity analysis show that there is significant dependence of material property of the SOFC on molar flow in the IIR. The molar flow of the primary reactant in the IIR, methane, is dramatically affected by the emissivity of the SOFC. For an emissivity of 0.4, the average molar flow rate of methane is 106% higher than the base case of an emissivity of 0.7. For an ideal emissivity of 1.0, the average molar flow of methane through the IIR is 28% low than the base case. Thus, at lower emissivities, the reformation reactions occur at a lower rate due to less radiation heat transferring to the gas stream and driving the reaction, and vice versa.

Temperature and Molar Flow in the IIR

Heat and material balances were described and simultaneously solved in MATLAB for the IIR. Two important characteristics of the reformer model are complexity and time expense to run the model. Increasing complexity of the system leads to better and more accurate results. However, a trade-off exists with increasing complexity because the time to solve the model will increase as well, which is undesirable for advanced controls. Figures D.2 and D.3 illustrate the resulting molar flow rates and gas temperatures over the length of the IIR. Figure D.2 shows the least complex system, a lumped model considering one large reaction volume. Figure D.3 represents a complex system of 10 discrete reaction volumes for the IIR. Resulting profiles for Figures D.2 and D.3 are quite different. In Figure D.2, the molar flowrate of methane

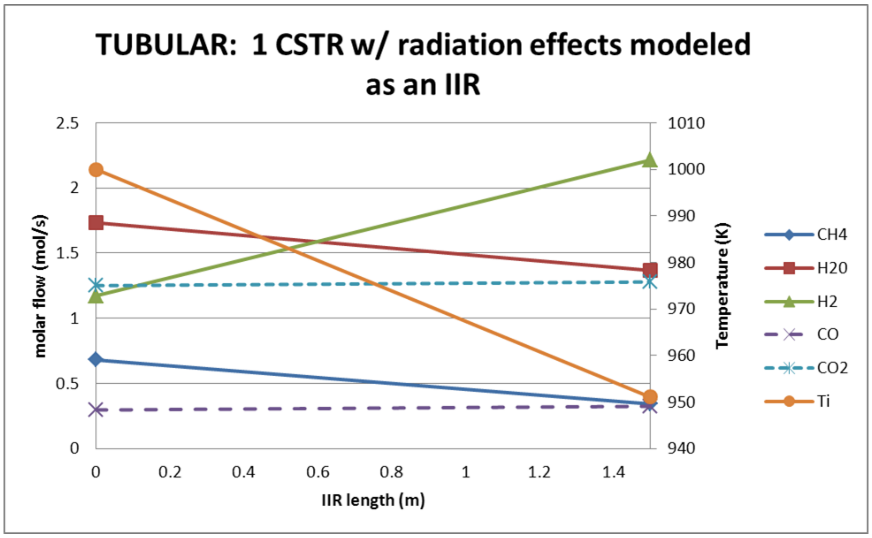

Figure D.2: Profiles using a lumped model with the lumped value equal to effluent

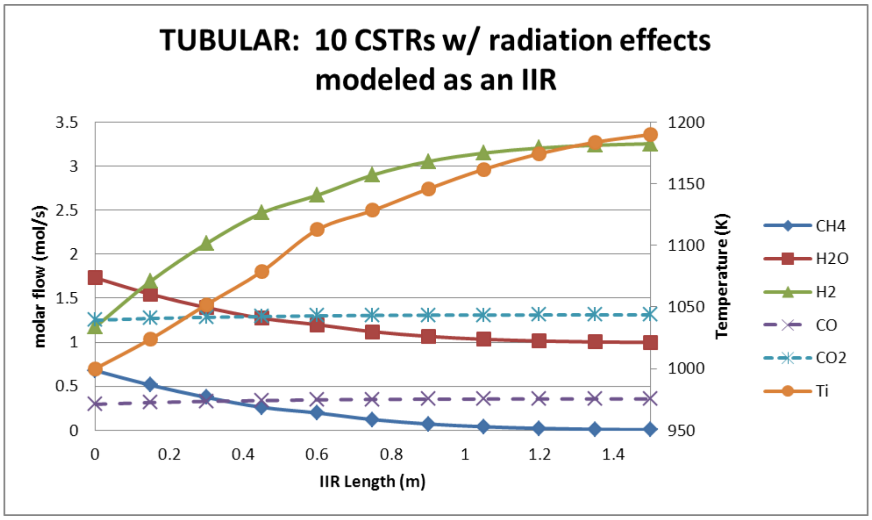

Figure D.3: Profiles based on the distributed parameter model

does not approach zero as it should and reactor temperature decreases, which is undesirable. Reactor temperature decreases for one volume because the effects of the endothermic reforming reactions dominate over the effects of radiation heating. Figure D.3 demonstrates more accurate profiles for all components in the IIR. Methane flow approaches zero while gas temperature approaches the wall temperature of 1200K. Additionally, the molar flow of steam approaches 1 mol/s due as it is consumed, while hydrogen production increases as the desired product. Carbon monoxide and carbon dioxide productions increase slightly.

The more complex model for the IIR resulted in much more accurate results at the expense of more time. However, the time elapsed for solving the simple IIR was 0.105 s versus 0.639 s for the complex IIR. Thus, time expense is not an issue for this model, and the more complex model should be used for its increased accuracy and profile resolution.

D.3 Conclusions

A steady-state indirect internal reformer was modeled for integration into a solid-oxide fuel cell. The primary purpose of the IIR is to reform methane further into hydrogen to be used in the SOFC. The reformer was modeled as a series of 10 CSTRs with reaction kinetics shown in Equation D.1. Sensitivity analysis showed a strong dependence of methane concentration on SOFC emissivity, the primary fuel in the system. At lower emissivities, the methane flow through the system is higher, and reacts to a lesser extent than at higher wall emissivities. Complexity analysis was performed on the IIR to evaluate the effects of reaction volume. A more complex system of 10 smaller reaction volumes proved to be more accurate and resulted in desirable flow and temperature trends through the IIR.

Bibliography

[1] E. Achenbach. Modeling and evaluation of advanced sofc, subtask a : Numerical modeling, experimental database and validation, activity a2 : Stack modeling, 1995.

[2] E. Achenbach and E. Riensche. Methane/steam reforming kinetics for solid oxide fuel cells. *Journal of Power Sources*, 52:283–288, 1994.

[3] P. Aguiar, C.S. Adjiman, and N.P. Brandon. Anode-supported intermediate temperature direct internal reforming solid oxide fuel cell. i: model-based steady-state performance. *Journal of Power Sources*, 138:120–136, 2004.

[4] P. Aguiar, C.S. Adjiman, and N.P. Brandon. Anode-supported intermediate-temperature direct internal reforming solid oxide fuel cell ii. model-based dynamic performance and control. *Journal of Power Sources*, 147:136–147, 2005.

[5] P. Aguiar, D. Chadwick, and L. Kershenbaum. Modelling of an indirect internal reforming solid oxide fuel cell. *Chemical Engineering Science*, 57(10):1665–1677, 2002.

[6] K. Ahmed and K. Foger. Kinetics of internal steam reforming of methane on ni/ysz-based anodes for solid oxide fuel cell. *Catal. Today*, 63:479–487, 2000.

[7] A. Arsalis. Thermoeconomic modeling and parametric study of hybrid sofc-gas turbine-steam turbine power plants ranging from 1.5 to 10 mwe. *Journal of Power Sources*, 181:313–326, 2008.

[8] Y.M. Barzi, M. Ghassemi, and M.H. Hamedi. Numerical analysis of start-up operation of a tubular solid oxide fuel cell. *International Journal of Hydrogen Energy*, 34:2015–2025, 2009.

[9] H.D. Baumann. *Control Valve Primer: A User's Guide.* Instrument Society of America, 3rd edition, 1998.

[10] M. Bavarian, M. Soroush, I.G. Kevrekidis, and J.B. Benziger. Mathematical modeling, steady-state and dynamic behavior, and control of fuel cells: A review. *Industrial and Engineering Chemistry Research*, 49:7922–7950, 2010.

[11] C. Beckermann and T. F. Smith. Incorporation of internal surface radiant exchange in the finite-volume method. *Journal Name: Numerical Heat Transfer. Part B, Fundamentals; (United States); Journal Volume: 23:1*, pages Medium: X; Size: Pages: 127–133, 1993.

[12] V.D. Belyaev, T.I. Politova, Mar'ina. O.A., and V.A. Sobyanin. Internal steam reforming of methane over ni-based electrode in solid oxide fuel cells. *Applied Catalysis A: General*, 133:45–57, 1995.

[13] D. Bhattacharyya and R. Rengaswamy. A review of solid oxide fuel cell (sofc) dynamic models. *Industrial and Engineering Chemistry Research*, 48:6068–6086, 2009.

[14] D. Bhattacharyya and R. Rengaswamy. System identification and nonlinear model predictive control of a solid oxide fuel cell. *Industrial and Engineering Chemical Research*, 49:4800–4808, 2010.

[15] F. Calise, M. d'Accadia, L. Vanoli, and M. Spakovsky. Full load synthesis/design optimization of a hybrid sofc-gt power plant. *Energy*, 32:446–458, 2007.

[16] S. Campanari. Thermodynamic model and parametric analysis of a tubular sofc module. *Journal of Power Sources*, 92:26–34, 2001.

[17] S. Campanari and P. Iora. Definition and sensitivity analysis of a finite volume sofc model for a tubular cell geometry. *Journal of Power Sources*, 132:113–126, 2004.

[18] T. Chen, J. Wright, and K. Krist. Sofc system analysis. Technical report, 1997.

[19] C.M. Colson and M.H. Nehrir. Evaluating the benefits of a hybrid solid oxide fuel cell combined heat and power plant for energy sustainability and emissions avoidance. *IEEE Transactions on Energy Conversion*, 26:140–148, 2011.

[20] P. Costamagna and K. Honneger. Modeling of solid oxide heat exchanger integrated stacks and simulation at high fuel utilization. *Journal of Electrochemical Society*, 145(11):3995–4007, 1998.

[21] Department of Defense. Department of defense instruction: Dod modeling and simulation (m&s) verification, validation, and accreditation (vv&a), 2009.

[22] Z. Deng, H. Cao, X. Li, J. Jiang, J. Yang, and Y. Qin. Generalized predictive control for fractional order dynamic model of solid oxide fuel cell output power. *Journal of Power Sources*, 195:8097–8103, 2010.

[23] C.M. Dikwal, W. Bujalski, and K. Kendall. The effect of temperature gradients on thermal cycling and isothermal ageing of micro-tubular solid oxide fuel cells. *Journal of Power Sources*, 193:241–248, 2009.

[24] P. Dokmaingam, S. Assabumrungrat, A. Soottitantawat, and N. Laosiripojana. Modelling of tubular-designed solid oxide fuel

cell with indirect internal reforming operation fed by different primary fuels. *Journal of Power Sources*, 195:69–78, 2010.

[25] R. Egidi. Integrated electric power systems. In *11th Annual SECA Workshop*, 2010.

[26] United States. Department of Energy. Cooling, heating, and power (chp) for commercial buildings benefits analysis, 2002.

[27] United States. Department of Energy. Combined heat and power: A decade of progress. a vision for the future., 2009.

[28] M. Fardadi, F. Mueller, and F. Jabbari. Feedback control of solid oxide fuel cell spatial temperature variation. *Journal of Power Sources*, 195:4222–4233, 2010.

[29] J.R. Ferguson, J.M. Fiard, and Herbin J. Three-dimensional numerical simulation for various geometries of solid oxide fuel cells. *Journal of Power Sources*, 58:109–122, 1996.

[30] K. Fischer and J.R. Seume. Impact of the temperature profile on thermal stress in a tubular solid oxide fuel cell. *Journal of Fuel Cell Science and Technology*, 6:1–9, 2009.

[31] R.A. George. Status of tubular sofc field unit demonstrations. *Journal of Power Sources*, 86:134–139, 2000.

[32] W. Graus and E. Worrel. Trend in efficiency and capacity of fossil power generation in the eu. *Energy Policy*, 37:2147–2160, 2009.

[33] D.J. Hall and R.G. Colclaser. Transient modeling and simulation of a tubular solid oxide fuel cell. *IEEE Transactions on Energy Conversion*, 14(3):749–753, 1999.

[34] A. Hawkes and M. Leach. Solid oxide fuel cell systems for residential micro-combined heat and power in the uk: Key economic drivers. *Journal of Power Sources*, 149:72–83, 2005.

[35] H. Huo, X. Zhu, W. Hu, H. Tu, J. Li, and J. Yang. Nonlinear model predictive control of sofc based on a hammerstein model. *Journal of Power Sources*, 185:338–344, 2008.

[36] M.M. Hussain, X. Li, and I. Dincer. A general electrolyteelectrode-assembly model for the performance characteristics of planar anode-supported solid oxide fuel cells. *Journal of Power Sources*, 189:916–928, 2009.

[37] Y. Inui, N. Ito, T. Nakajima, and A. Urata. Analytical investigation on cell temperature control method of planar solid oxide fuel cell. *Energy Conversion & Management*, 47:2319–2328, 2006.

[38] A.K.S. Iyengar, N.A. Desai, S.D. Vora, and L.A. Shockling. Numerical investigation of a delta high power density cell and comparison with a flattened tubular high power density cell. *Journal of Fuel Cell Science and Technology*, 7:1–8, 2010.

[39] F. Jurado. Predictive control of solid oxide fuel cells using fuzzy hammerstein models. *Journal of Power Sources*, 158:245–253, 2006.

[40] R. Kandepu, L. Imsland, B. A. Foss, C. Stiller, B. Thorud, and O. Bolland. Modeling and control of a sofc-gt-based autonomous power system. *Energy*, 32(4):406–417, 2007.

[41] S. Karellas, J. Karl, and E. Kakaras. An innovative biomass gasification process and its coupling with microturbine and fuel cell systems. *Energy*, 33:284–291, 2008.

[42] J.A. Kent. *Kent and Riegel's Handbook of Industrial Chemistry and Biotechnology*. Springer, 11th edition, 2007.

[43] M. Koyama. http://www.aki.che.tohoku.ac.jp/ koyama/html/research/sofc.html, 2008.

[44] S. Kurachi, Y. Mizutani, T. Hiroyama, K. Katsurayama, F. Okada, and K. Ukai. Development of a small-scale solid oxide fuel cell (sofc). In *24th World Gas Conference*, Argentina, 2009.

[45] J. Laraminie and A. Dicks. *Fuel Cell Systems Explained*. John Wiley & Sons, Inc., New York, NY, 2000.

[46] A.L. Lee. Internal reforming development for solid oxide fuel cells. final report, doe/mc22045-2364. Technical report, Feb 1987.

[47] P. Li and M. Chyu. Simulation of the chemical/electrochemical reactions and heat/mass transfer for a tubular sofc in a stack. *Journal of Power Sources*, 124:487–498, 2003.

[48] S. Linderoth. Innovative energy technologies. Presentation, Riso National Laboratory, Technical University of Denmark, 2007.

[49] S. Linderoth. Solid oxide cell r&d at riso national laboratory–and its transfer to technology. *Journal of Electroceramics*, 22:61–66, 2009.

[50] A.B. Lovins. *Small is Profitable: The Hidden Economic Benefits of Making Electrical Sources the Right Size*. Rocky Mountain Institute, Snowmass, CO, 2002.

[51] F. Marsano, L. Magistri, and A.F. Massardo. Ejector performance influence on a solid oxide fuel cell anodic recirculation system. *Journal of Power Sources*, 129:216–228, 2004.

[52] F. Mueller, F. Jabbari, J. Brouwer, S.T. Junker, and H. Ghezel-Ayagh. Linear quadratic regulator for a bottoming solid oxide fuel cell gas turbine hybrid system. *Journal of Dynamic Systems, Measurement, and Control*, 131:1–9, 2009.

[53] F. Mueller, B. Tarroja, J. Maclay, F. Jabbari, J. Brouwer, and S. Samuelsen. Design, simulation and control of a 100 mw-class solid oxide fuel cell gas turbine hybrid system. *Journal of Fuel Cell Science and Technology*, 7:1–11, 2010.

[54] A.M. Murshed, B. Huang, and K. Nandakumar. Estimation and control of a solid oxide fuel cell system. *Computers and Chemical Engineering*, 34:96–111, 2010.

[55] A. Nakajo, C. Stiller, G. Harkegard, and O. Bolland. Modeling of thermal stresses and probability of survival of tubular sofc. *Journal of Power Sources*, 158:287–294, 2006.

[56] D. Nishijima. Development of sofc for residential use at ngk spark plug co., ltd. In *Fuel Cell Seminar 2010*, San Antonio, TX, 2010.

[57] R. O'Hayre, S. Cha, W. Colella, and F. Prinz. *Fuel Cell Fundamentals*. Wiley, 2nd edition, 2009.

[58] R.H. Perry and D.W. Green. *Perry's Chemical Engineering Handbook*. McGraw-Hill Professional, 8th edition, 2007.

[59] L. Petruzzi, S. Cocchi, and F. Fineschi. A global thermo-electrochemical model for sofc systems design and engineering. *Journal of Power Sources*, 118:96–107, 2003.

[60] J. Pierre. Siemens energy. In *11th Annual SECA Workshop*, Pittsburgh, PA, 2010.

[61] E. Porpatham, A. Ramesh, and B. Bagalingam. Investigation on the effect of concentration of methane in biogas when used as a fuel for a spark ignition engine. *Fuel*, 87:1651–1659, 2008.

[62] S. J. Qin and T. A. Badgwell. A survey of industrial model predictive control technology. *Control Engineering Practice*, 11(7):733–764, 2003.

[63] C. Rechnenauer and E. Achenbach. *Dreiddimensionale mathematische Modellierung des stationaren und instationaren Verhaltens oxidkeramischer Hocthtemperatur-Brennstoffzellen.* Doctoral thesis, Forschungszentrum Julich, 1993.

[64] R.C. Reid, J.M. Prausnitz, and B.E. Poling. *The Properties of Gases and Liquids.* McGraw-Hill, New York, 1987.

[65] W. Schmittinger and A. Vahidi. A review of the main parameters influencing long-term performance and durability of pem fuel cells. *Journal of Power Sources*, 180:1–14, 2008.

[66] A. Selimovic. *SOFC Modeling for SOFC/GT Combined Cycle Simulations.* Licenciate thesis, Lund University, 2000.

[67] O. Shaneb, G. Coates, and P. Tayler. Micro combined heat and power technologies and control for residential applications. *International Journal of Renewable Energy Technology*, 1:325–347, 2010.

[68] S.C Singhal. Advances in tubular solid oxide fuel cell technology. In *Proceedings of the Fourth International Symposium on Solid Oxide Fuel Cells*, volume 95-1, pages 195–207, Pennington, NJ, 1995.

[69] C. Stiller. *Design, Operation and Control Modelling of SOFC/GT Hybrid Systems.* Doctoral thesis, Norwegian University of Science and Technology, 2006.

[70] C. Stiller, B. Thorud, O. Bolland, R. Kandepu, and L. Imsland. Control strategy for a solid oxide fuel cell and gas turbine hybrid system. *Journal of Power Sources*, 158:303–315, 2006.

[71] C. Stiller, B. Thorud, S. Seljebo, O. Mathisen, H. Karoliussen, and O. Bolland. Finite-volume modeling and hybrid-cycle performance of planar and tubular solid oxide fuel cells. *Journal of Power Sources*, 141:227–240, 2005.

[72] Y. L. Sun, S. Ghantasala, and N. H. El-Farra. Networked control of distributed energy resources: Application to solid oxide fuel cells. *Industrial & Engineering Chemistry Research*, 48(21):9590–9602, 2009.

[73] B. Thorud, C. Stiller, T. Weydahl, O. Bolland, and H. Karoliussen. Part-load and load change simulation of tubular sofc systems. In *Fuel Cell Forum*, Lucerne, 2004.

[74] C. Voisard. Manufacturing solid oxide fuel cells for the sulzer hexis stationary system. *International Journal of Applied Ceramic Technology*, 1:31–39, 2004.

[75] S.D. Vora. Office of fossil energy fuel cell program - solid state energy conversion alliance (seca) - clean economic energy for a carbon challenged world. In *11th Annual SECA Workshop*, Pittsburgh, PA, 2010.

[76] H. Xi and J. Sun. A low-order dynamic model for planar solid oxide fuel cells using online iterative computation. *Journal of Fuel Cell Science and Technology*, 5:1–11, 2008.

[77] J. Xu and G.F. Froment. *AIChE Journal*, 35:88–96, 1989.

[78] X. Xue, J. Tang, N. Sammes, and Y. Du. Dynamic modeling of single tubular sofc combining heat/mass transfer and electrochemical reaction effects. *Journal of Power Sources*, 142:211–222, 2005.

[79] H. Yakabe, T. Ogiwara, M. Hishinuma, and I. Yasuda. 3-d model calculation for planar sofc. *Journal of Power Sources*, 102(1-2):144–154, 2001.

[80] J. Yuan, M. Rokni, and B. Sunden. Three-dimensional computational analysis of gas and heat transport phenomena in ducts relevant for anode-supported solid oxide fuel cells. *International Journal of Heat and Mass Transfer*, 46:809–821, 2003.

[81] Huayang Zhu, Andrew M. Colclasure, Robert J. Kee, Yuanbo Lin, and Scott A. Barnett. Anode barrier layers for tubular solid-oxide fuel cells with methane fuel streams. *Journal of Power Sources*, 161(1):413–419, 2006.

[82] Y. Zhu, W. Cai, C. Wen, and Y. Li. Fuel ejector design and simulation model for anodic recirculation sofc system. *Journal of Power Sources*, 173:437–449, 2007.

Vita

Benjamin James Spivey was born in Atlanta, GA and graduated from Killian Hill Christian School in Lilburn, GA in May of 2000. He entered the Georgia Institute of Technology to pursue a degree in mechanical engineering in fall of 2000. During his undergraduate degree, he worked with Michelin Americas R&D in Greenville, SC, and Edwards Lifesciences in Irvine, CA. Upon graduation in May 2005, he worked as a design engineer with General Electric in Greenville, SC designing hot gas path gas turbine components. In spring of 2007, he entered the graduate school at The University of Texas at Austin. He earned a masters degree in chemical engineering in December 2009 and participated in internships with ExxonMobil Chemical in Baytown, TX, in advanced process controls.

My faith, friends in Austin, and family have provided valued perspective throughout my time in Austin working towards the PhD.

> Trust in the Lord with all your heart and lean not on your own understanding; in all your ways acknowledge him, and he will make your paths straight. Proverbs 3:5-6

Permanent address: ben.spivey@gmail.com

This dissertation was typeset with LaTeX[†] by the author.

[†] LaTeX is a document preparation system developed by Leslie Lamport as a special version of Donald Knuth's TeX Program.